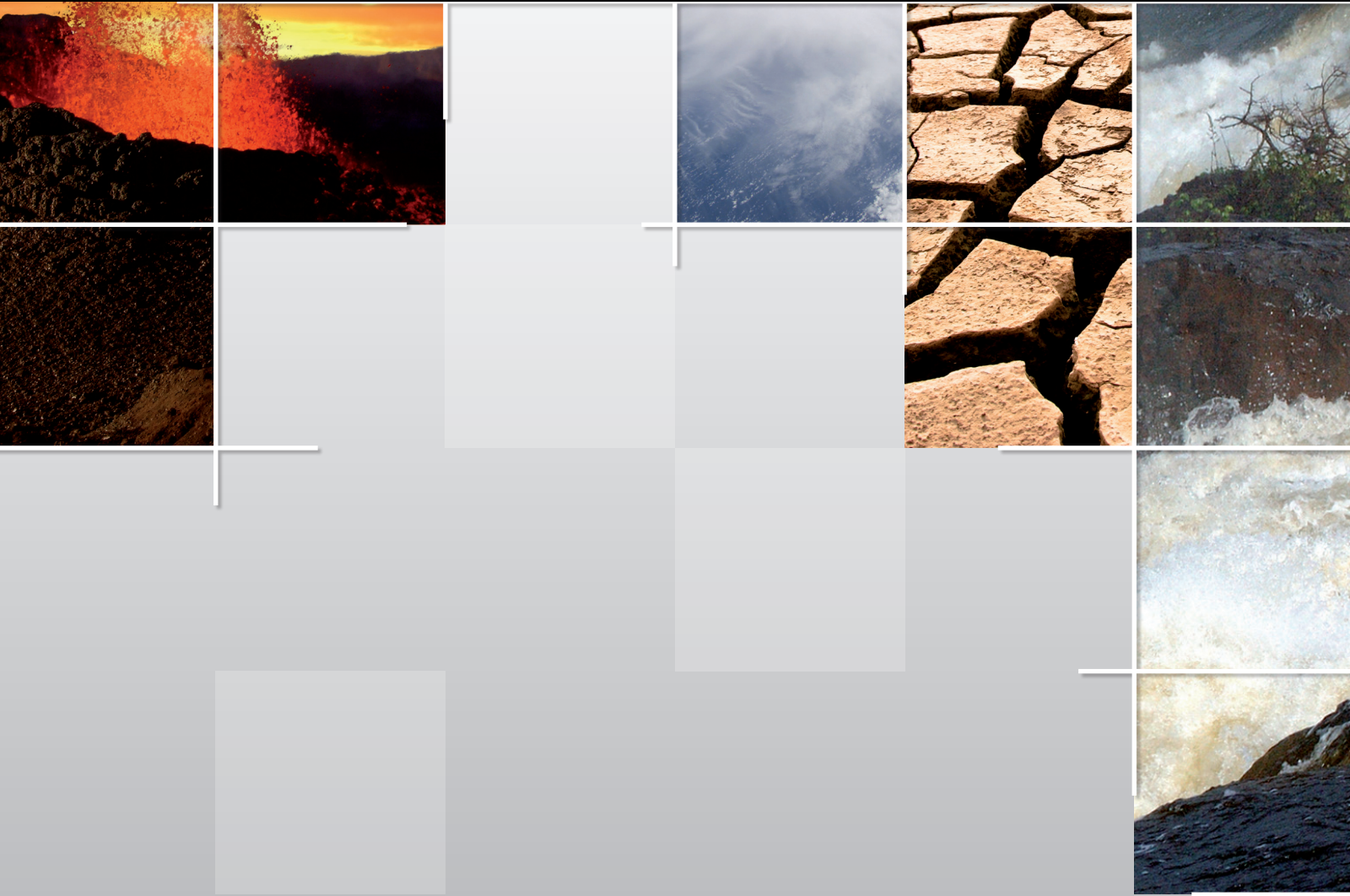


Landslides and Geophysical Investigations: Advantages and Limitations

Lead Guest Editor: Stefano Morelli

Guest Editors: Stefano Utili, Veronica Pazzi, Riccardo Castellanza,
and Xuanmei Fan





Landslides and Geophysical Investigations: Advantages and Limitations

Landslides and Geophysical Investigations: Advantages and Limitations

Lead Guest Editor: Stefano Morelli

Guest Editors: Stefano Utili, Veronica Pazzi,
Riccardo Castellanza, and Xuanmei Fan



Copyright © 2019 Hindawi. All rights reserved.

This is a special issue published in “International Journal of Geophysics.” All articles are open access articles distributed under the Creative Commons Attribution License, which permits unrestricted use, distribution, and reproduction in any medium, provided the original work is properly cited.

Editorial Board

Marco Bonini, Italy
Yun-tai Chen, China
Angelo De Santis, Italy
Gary Egbert, USA
Semih Ergintav, Turkey
Fabrizio Galadini, Italy
Salvatore Gambino, Italy

Marek Grad, Poland
Libo Liu, China
Francisco Luzon Martinez, Spain
Steve Milan, UK
Veronica Pazzi, Italy
Salvatore Piro, Italy
Ruey-Juin Rau, Taiwan

Sheng-Rong Song, Taiwan
Pantelis Soupios, Greece
Alexey Stovas, Norway
Sándor Szalai, Hungary
Filippos Vallianatos, Greece
Petr Vaníček, Canada
Michael S. Zhdanov, USA

Contents

Landslides and Geophysical Investigations: Advantages and Limitations

S. Morelli , S. Utili, V. Pazzi , R. Castellanza, and X. Fan

Editorial (2 pages), Article ID 8732830, Volume 2019 (2019)

A Review of the Advantages and Limitations of Geophysical Investigations in Landslide Studies

Veronica Pazzi , Stefano Morelli , and Riccardo Fanti

Review Article (27 pages), Article ID 2983087, Volume 2019 (2019)

3D Mafic Topography of the Transition Zone between the North-Western Boundary of the Congo Craton and the Kribi-Campo Sedimentary Basin from Gravity Inversion

Séverin Nguiya, Willy Lemotio , Philippe Njandjock Nouck, Marcelin M. Pemi, Alain-Pierre K. Tokam, and Evariste Ngatchou

Research Article (15 pages), Article ID 7982562, Volume 2019 (2019)

The Mitla Landslide, an Event That Changed the Fate of a Mixteco/Zapoteco Civilization in Mesoamerica

V. H. Garduño-Monroy , A. Figueroa-Soto, N. Magaña-García, A. Ruiz-Figueroa, J. Gómez-Cortés, A. Jiménez-Haro, and V. M. Hernández-Madrigal


Research Article (14 pages), Article ID 5438381, Volume 2019 (2019)

HVSR Analysis of Rockslide Seismic Signals to Assess the Subsoil Conditions and the Site Seismic Response

Alessia Lotti, Veronica Pazzi , Gilberto Saccorotti, Andrea Fiaschi, Luca Matassoni, and Giovanni Gigli

Research Article (11 pages), Article ID 9383189, Volume 2018 (2019)

Integrated Geophysical-Geological 3D Model of the Right-Bank Slope Downstream from the Rogun Dam Construction Site, Tajikistan

Hans-Balder Havenith , Isakbek Torgoev, and Anatoli Ischuk

Research Article (16 pages), Article ID 1641789, Volume 2018 (2019)

Editorial

Landslides and Geophysical Investigations: Advantages and Limitations

S. Morelli ¹, S. Utili,² V. Pazzi ¹, R. Castellanza,³ and X. Fan⁴

¹Department of Earth Sciences, University of Firenze, Firenze, Italy

²Newcastle University, Newcastle upon Tyne, UK

³University of Milano-Bicocca, Milano, Italy

⁴Chengdu University of Technology, Sichuan, China

Correspondence should be addressed to V. Pazzi; veronica.pazzi@unifi.it

Received 4 July 2019; Accepted 4 July 2019; Published 16 July 2019

Copyright © 2019 S. Morelli et al. This is an open access article distributed under the Creative Commons Attribution License, which permits unrestricted use, distribution, and reproduction in any medium, provided the original work is properly cited.

Geohazards processes can damage or increase the risk of human beings, properties, critical infrastructures, and environment itself. They also could involve the interruption of human activities with serious socioeconomic consequences. Among all the natural occurrences, landslides are regarded as one of the most destructive types of geohazards. Landslides are a type of “mass wasting,” which denotes any down-slope movement of soil and rock under the direct influence of gravity, which can occur and develop in a large variety of volumes and shapes. Even though the catastrophic impact of landslides is not totally unavoidable, it can be significantly reduced by increasing the capacity to assess and predict the risks and using different mitigation methods. In the past decades, many 2D and 3D numerical modelling methods have been designed and developed to assess slope stability, to predict slope response to various triggers, to evaluate the slope deformation and evolution pattern, and to perform back-analysis simulations. Nevertheless, such models still require access to detailed knowledge of the geological, mechanical, and hydrological properties of landslides and boundary conditions. Therefore, accurate geological field surveys have to be integrated by means of low-cost and noninvasive techniques, like the geophysical ones, to collect widespread data with the aim of reconstructing a suitable geological and hydrogeological model of the area, improving the reliability of deterministic model.

This special issue is dedicated to the geophysical methods applied to investigate, characterize, and monitor landslides.

Over the years, both the advantages and limitations of these techniques have been highlighted, and some drawbacks are still open. Some papers were submitted to this special issue, and, after a thorough peer review process, only five articles were selected to be included in this special issue. This relatively small number is probably caused by the difficulty in applying geophysical techniques on slope movements given hard-operating conditions (e.g., high slopes, distance from access roads, and lack of security for the technical operator) and not because the methods limitations are greater than the advantages.

The review carried out by V. Pazzi et al. on geophysical techniques applied in landslides studies analyses the international efforts toward overcoming the geophysical technique limitations highlighted by the 2007 geophysics and landslide review, focusing on works of the last twelve years (2007-2018). The authors carried out the review analysis using a “material landslide approach” on the basis of the more recent landslides classification. The most studied landslides are those of the flow type for “soil” landslide typology and those of the fall type for the “rock” category. From the “employed method” point of view, active and passive seismic methods are the most employed in landslide characterization and monitoring. To quantify the efforts performed to overcome the limitations highlighted in 2007, a three-level scale was employed (from many/some efforts to non-discussed). The limits inherent in each technique and the need to still develop multisource data integration methods were clear; very often

the main drawbacks depend on the operator who carries out the survey, the analysis of data, and the interpretation and the presentation of the results. Finally, independently of the applied technique/s, a very accurate and high-resolution survey could be performed only on a small landslide portion, as it is costly and time-consuming.

V. H. G. Monroy et al. describe the preliminary results of an integrated geological and geophysical study carried out to demonstrate that the city of Mitla (Mexico) was covered by the deposits of a dry landslide. It is a collapsed body composed of ignimbrite blocks and matrix from the Sierra La Calavera, and according to its morphology, the geotechnical characteristics, and the geophysical data interpretation, the landslide was provoked by an earthquake of a magnitude in the range from 6.2 to 7.3 Mw. Unfortunately, until now there is no a precise age established for the landslide occurrence. However, the event presumably damaged the pyramids of Mitla in historical times, and large parts of the pyramids are probably still located under the avalanche deposit as evidenced by the outcomes of this preliminary investigation. This paper highlights how geophysical exploration, in particular electrical resistivity tomographies, the study of earthquakes, and the environmental seismic noise carried out in synergy with other survey techniques are good and promising tools in the geoarchaeology field of research.

The paper by H.-B. Havenith et al. presents the results of an integrated survey and the 3D geomodel generated for an ancient mass movement located immediately downstream from the Rogun Dam construction site (Tajikistan). The geophysical survey includes electrical resistivity tomographies, seismic profiles, and ambient vibration measurements, as well as earthquake recordings. The integrated interpretation of all results reveals that probably only a relatively small part of the ancient giant mass movement is really exposed to slope instability phenomena. Nevertheless, authors highlight how all the geophysical measurements are affected by a great variability that affects the final estimated unstable volume.

Implementing an early warning system (EWS) is a challenging issue in landslide monitoring. To verify the usefulness of seismic noise analysis as part of an EWS, A. Lotti et al. describe the results of the HV analysis of a 7-month period of passive seismic data collected by a pilot scale passive seismic network arranged to monitor an unstable rock mass. Possible connection between rainfall/temperature/displacement and rockslide seismic activity is evaluated, and the hypothesis that the HV amplitude value is directly related to meteorological factors can be excluded. On the contrary, the observed variations potentially reveal changes of subsoil site conditions and have also implications for the assessment of site response to seismic shaking.

Finally, S. Nguiya et al., based on the analysis and the gravity inversion constrained by seismic information, show the geodynamic implication of the intracrustal mafic discontinuity in the north-western portion of the Congo Craton and its implication for the occurrence of landslides across the area. Faults, earthquake, volcanism, and geomorphology are known as potential triggers of landslides. According to the authors, by correlating the location of some observed

landslides and the gravity data, new insights into the regional tectonic can be inferred.

Conflicts of Interest

The authors declare that there are no conflicts of interest regarding the publication of this paper.

Acknowledgments

We would like to thank all the authors who contributed to this special issue. This publication would not be possible without the participation of our expert reviewers, who provided valuable feedback and constructive comments throughout the review process.

*S. Morelli
S. Utili
V. Pazzi
R. Castellanza
X. Fan*

Review Article

A Review of the Advantages and Limitations of Geophysical Investigations in Landslide Studies

Veronica Pazzi , Stefano Morelli , and Riccardo Fanti

Department of Earth Sciences, University of Firenze, Via G. La Pira 4, 50121 Firenze, Italy

Correspondence should be addressed to Veronica Pazzi; veronica.pazzi@unifi.it

Received 30 November 2018; Accepted 27 June 2019; Published 14 July 2019

Academic Editor: Pantelis Soupios

Copyright © 2019 Veronica Pazzi et al. This is an open access article distributed under the Creative Commons Attribution License, which permits unrestricted use, distribution, and reproduction in any medium, provided the original work is properly cited.

Landslide deformations involve approximately all geological materials (natural rocks, soil, artificial fill, or combinations of these materials) and can occur and develop in a large variety of volumes and shapes. The characterization of the material inhomogeneities and their properties, the study of the deformation processes, and the delimitation of boundaries and potential slip surfaces are not simple goals. Since the '70s, the international community (mainly geophysicists and lower geologists and geological engineers) has begun to employ, together with other techniques, geophysical methods to characterize and monitor landslides. Both the associated advantages and limitations have been highlighted over the years, and some drawbacks are still open. This review is focused on works of the last twelve years (2007-2018), and the main goal is to analyse the geophysical community efforts toward overcoming the geophysical technique limitations highlighted in the 2007 geophysics and landslide review. To achieve this aim, contrary to previous reviews that analysed the advantages and limitations of each technique using a “technique approach,” the analysis was carried out using a “material landslide approach” on the basis of the more recent landslides classification.

1. Introduction

Large landslides and smaller-scale mass movements are natural widespread processes that result in the downward and outward movement of slope-forming materials, significantly sculpting the landscape and redistributing sediment and debris to gentler terrain. The rapid population growth and the pressure from human activities have strongly influenced their extension and occurrence so that they have become disasters causing vast direct and indirect socioeconomic consequences [1]. These deformations involve approximately all geological materials (natural rocks, soil, artificial fill, or combinations of these materials) and can occur and develop in a large variety of volumes and shapes [2]. Artificial fills are usually composed of excavated, transported, and placed soil or rock, but they can also contain demolition debris, ash, slag, and solid trash. The term rock refers to hard or firm bedrock that was intact and in place prior to slope movement. Soil, either residual or transported material, is used for unconsolidated particles or poorly cemented rock or aggregates. Soil is usually further distinguished on the basis of texture as debris (coarse fragments) or earth (fine fragments) according to the well-established Varnes Classification [3]. Following the

recent updating of [4], more reasonable use of geotechnical material terminology (clay, silt, sand, gravel, and boulders) is starting to spread, although some classical terminologies (mud, debris, earthflow, peat, and ice) are maintained after a recalibration of their definitions, because they have acquired a recognized status in landslide science by now. The Hungry classification includes aggregations of different materials that have been mixed by geomorphic processes such as weathering, mass wasting, glacier transport, explosive volcanism, or human activity. The use of geotechnical terminology is indeed most useful, as it relates best to the mechanical behaviour of the landslide as stated by [4] and even to most common investigation methods. In any case, the distinction between different materials is usually based on interpretation of the main geomorphic characteristics within landslide deposits but can also be inferred from the geological attributes of the involved parent material. The type of material is one of the most important factors influencing the movement of landslides, which can be categorized as falls, topples, spreads, slides, or flows according to their behaviour from the source area to the final deposit through distinctive kinematics [2, 3, 5]. Actually, the most common criterion used in landslides classification is based on the combination of the materials

with the type of movement, but it is possible to find many other classification criteria, including velocities, volumes, water content, geotechnical parameters, and processes related to the formation of the mobilized material, among others. This is because, as stated by [5], engineering geology literature on landslides is affected by inconsistent terminology and ambiguous definitions from older classifications and current key terms for both specialists and the public. Currently, the most widely accepted and used classification is that of [2], which enhances the previous system devised by D.J. Varnes [3, 6]. Since then, only small improvements for specific categories have occurred, such as that for flow-like landslides by [5]. In 2014 Hungr et al. [4], by maintaining the consolidated concepts introduced by [2], redefined some basic elements (basically typology and material) that still refer to the original characterization of [3] and, consequently, updated the total amount of categories (from 29 to 32), along with revisiting some of their descriptions. This new landslides classification version (Table 1), which was proposed to simplify landslides studies, is increasingly circulating in the academic world, and for this reason, it is used as the reference in the present paper.

Characterizing landslide material inhomogeneities and their properties, studying the deformation processes, and delimiting boundaries and potential slip surfaces are not simple goals. They require the availability of a wide range of data, observations, and measurements (e.g., kinematic, geomorphologic, geological, geotechnical, and petro-physical data [7]) and the evaluation of geologic and hydrologic conditions related to phenomena occurrences [8]. To obtain the needed information, many techniques including both traditional methods (detailed geomorphological surveys, geotechnical investigations, local instrumentation, and meteorological parameters analyses) and more recent methods (remote-sensing satellite data, aerial techniques, and synthetic aperture radar interferometry) can be employed [9, 10] and references within]. Among the latter, geophysical techniques are also included, since they are very useful in detecting the petro-physical properties of the subsoil (e.g., seismic wave velocity, electrical resistivity, dielectric permittivity, and gravitational acceleration [7]). Even though linking geophysical parameters and geological/geotechnical properties should always be supported with direct information (e.g., data from drillings), geophysical methods can provide the layered structure of the soil and certain mechanical parameters [11]. Therefore, because almost all of the advantages of geophysical methods correspond to disadvantages of geotechnical techniques and vice versa, the two investigation techniques can be considered complementary. Finally, the geophysical inversion data, and, therefore, the creation of a reliable subsoil model, is a complex and nonlinear problem that must be evaluated by taking into account all the available data on the site [11].

It is to be noted that the success of geophysical methods is mostly dependent on the presence of a significant and detectable contrast in the physical properties of different lithological units. However, in landslide characterization, geophysical contrast (i.e., differences in mechanical and physical properties) cannot be associated only with a boundary in mechanical properties (i.e., landslide boundaries) and therefore be of interest relative to the slope stability. These

measured variations, in fact, could be local anomalies within the landslide or caused by the rough topography, and as a result, they could be of no or little interest [12]. This is why according to [11], the references for landslide investigation purposes are relatively few, and according to [13], there have been few landslides in which geophysical techniques were very useful. Nevertheless, the application of these techniques has changed over the years thanks to technological progress, the availability of cheaper computer electronic parts, and the development of more portable and faster equipment and new software for data processing [12], allowing the adequate investigation of 3D structures, which addresses one of the most ancient geophysical method limitations according to [11].

This review work, which starts from [11], is focused on the last twelve years of works (2007-2018) published in international journals and available online. The main goal was to analyse the geophysical community efforts in overcoming the geophysical technique limitations highlighted in the conclusion section of [11]. The drawbacks pointed out were as follows: (i) geophysicists have to make an effort in the presentation of their results; (ii) the resolution and penetration depth of each method are not systematically discussed in an understandable way; (iii) the geological interpretation of geophysical data should be more clearly and critically explained; (iv) the challenge for geophysicists is to convince geologists and engineers that 3D and 4D geophysical imaging techniques can be valuable tools for investigating and monitoring landslides; and finally, (v) efforts should also be made towards achieving quantitative information from geophysics in terms of geotechnical parameters and hydrological properties. To reach the aim, contrary to the four geophysics and landslide reviews discussed in section number 2 [8, 11, 12, 14] that analysed the advantages and limitations of each technique using a “technique approach,” the analysis in this paper was carried out on the basis of a “material landslide approach” according to the recent landslide classification discussed above [4]. Finally, since it is beyond the aim of the work, we do not discuss the theoretical principles of the different geophysical techniques nor how to perform field surveys in this paper.

2. Geophysical Techniques and Landslides: The State of the Art of Review Papers

One of the first papers related to the application of geophysical techniques for the investigation of landslides, defined as a pioneering work by [11], is [8]. Herein, “landslides” are defined as a sudden or gradual rupture of rocks and their movement downslope by the force of gravity. In this paper, the main advantages of applying geophysical methods are as follows: (a) the rapid investigation of vast areas, collecting a larger number of sample points than those acquired by geologic engineering techniques; (b) the determination of the mechanical properties of wet and dry soils based on the measurements of large rock volumes directly involved in the processes; (c) the measured parameters reflect the combined geological and hydrological characteristics, which sometimes cannot be identified separately; and (d) the measurements

TABLE 1: Nomenclature of the newly proposed landslide classification version according to [4] based on the Varnes classification system. Words divided by / (slash symbol) have to be used alternatively. In italic movement types that usually reach extremely rapid velocities as defined by [2], while for the others, the velocity varies between extremely slow to very rapid (for details, refer to [4]).

TYPE OF MOVEMENT	ROCK	SOIL
Fall	<i>Rock/ice fall</i>	<i>Boulder/debris/silt fall</i>
Topple	<i>Rock block topple</i> <i>Rock flexural topple</i>	<i>Gravel/sand/silt topple</i>
Slide	<i>Rock rotational slide</i> <i>Rock planar slide</i> <i>Rock wedge slide</i> <i>Rock compound slide</i> <i>Rock irregular slide</i>	<i>Clay/silt rotational slide</i> <i>Clay/silt planar slide</i> <i>Gravel/sand/debris slide</i> <i>Clay/silt compound slide</i>
Spread	<i>Rock slope spread</i>	<i>Sand/silt liquefaction spread</i> <i>Sensitive clay spread</i>
Flow	<i>Rock/ice avalanche</i>	<i>Sand/silt/debris dry flow</i> <i>Sand/silt/debris flowslide</i> <i>Sensitive clay flowslide</i> <i>Debris flow</i> <i>Mud flow</i> <i>Debris flood</i> <i>Debris avalanche</i> <i>Earthflow</i> <i>Peat flow</i>
Slope Deformation	<i>Mountain slope deformation</i> <i>Rock slope deformation</i>	<i>Soil slope deformation</i> <i>Soil creep</i> <i>Solifluction</i>

can be repeated any number of times without disturbing the environment. Four main goals can be reached by applying vertical electric sounding (VES), seismic refraction (SR), self-potential (SP), and electromagnetic measurements (EM), listed as follows: (i) the investigation of the landslide geologic configuration, (ii) the investigation of the groundwater (determining the level and its fluctuation with time) as a landslide formation factor, (iii) the study of the physical properties and status of the landslide deposits and their changes with time, and (iv) the investigation of the landslide displacement process. Reference [8] also showed how electrical resistivity values and seismic waves velocities decrease between the bedrock and the rocks in the landslide body. Finally, in the conclusion section of [8], microseismic noise (SN) analysis is mentioned as a valuable method by which to characterize the slope soil strata.

Reference [14] conducted a review of the geophysical methods employed in landslide investigations. They highlighted that the selection of the method/s to be applied depends on its/their suitability for solving the problem. To estimate this adequacy, there are four main control factors: (i) the definition/understanding of the geophysical contrasts that have to be investigated, (ii) the evaluation of the characteristics (penetration depth and resolution) of the geophysical

methods, (iii) the calibration of the acquired data by means of geological/geotechnical data, and finally, (iv) the signal-to-noise ratio. In the paper, several case studies are shown wherein the SR was successfully employed to determine the lower landslide boundary.

Ten years later, the SR, seismic reflection (SR_e), electrical resistivity (ER), SP, EM, and gravimetry were discussed by [12] as the most frequently used methods in landslide characterization. For each method, the author gives (i) the theoretical principles, (ii) how to perform the measurements, (iii) the sources for those which are active techniques, and, finally, (iv) some expected results. Moreover, he presents some summary tables with the physical property ranges (e.g., those of the P-wave velocity, density, and electrical resistivity) of the most common soil and rock masses in their crude form (without taking into account variations caused by different clay contents, weathering, saturation, etc.). Finally, for each discussed method, [12] synthesizes in one table its suitability for use in landslide characterization, human artefact (like pipes and foundations) identification, and physical properties determination for geotechnical purposes. Overall, the SP method results are not or only marginally suitable in all fields. Nevertheless, in the same year, [15] and, later, [16–18] showed how the SP method could be helpfully employed. From the table

in [12], the seismic tomography and 2D and 3D geo-electric results correspond to the best methods for use in landslide characterization.

Reference [11] presents the state of the art of the geophysical techniques applied in landslide characterization based on papers after 1990. According to this review, the methods could be divided into seldom, widely, and increasingly used categories. Among the first methods they enumerate are SRe, ground penetrating radar (GPR), and gravimetry, while among the second group are SR, ER VES, or tomographies (ERT), and SP, and, finally, among the third group are SN, surface waves (SW), and EM. Moreover, they indicate seismic tomography (ST) as method useful only for limited site conditions (rock slides). They synthesize in a table (a) the main geophysical methods used, (b) the measured geophysical parameters and information type, (c) the geological context, (d) the landslide classification following [2], (e) the geomorphology, and (f) the applications (targets). According to the review in [11], there are three main advantages and three main limitations in employing geophysics for the subsurface mapping of landslides. As benefits of the geophysical methods, the author enumerates (i) the flexibility and the relative efficiency on slopes; (ii) the noninvasiveness and the generation of information on the internal structures of soil or rock masses; and (iii) the allowance of examining large volumes of soil. As drawbacks, he highlights that (i) the resolution, which is dependent on the signal-to-noise ratio, decreases with depth; (ii) the solution for a set of data is nonunique, and the results must be calibrated; and (iii) these methods yield indirect information on the subsoil, such as physical parameters rather than geological or geotechnical properties. One of the main conclusions of the review is that in landslide characterization, the geophysical survey design is still a much-debated question, and no unique strategy has arisen from the literature.

Reference [11] is the last review published in an international journal and available online that focused on the advantages and limitations of the geophysical methods applied in landslides characterization. Reference [19], in fact, discusses, by means of case studies, benefits and drawbacks of the most common geophysical techniques (GPR, ER, and SR) in geomorphological applications. Therefore, in this paper landslides are just one of the possible fields of application. Two more recent reviews about geophysics and landslides are [20, 21]. The first is focused only on the ERT technique applied in landslide investigations and analyses the advantages and limitations of 2D-, 3D-, and 4D-ERT (or time-lapse ERT: tl-ERT) surveys based on papers of the period from 2000 to 2013. The second is a review of the current state of the art and the future prospects of the near surface geophysical characterization of areas prone to natural hazards (e.g., landslides, rockfalls, avalanches and rock glaciers, floods, sinkholes and subsidences, earthquakes, and volcanos) published in a book series (and, therefore, not freely available online for download), wherein the analysis of the geophysical techniques applied in landslides characterization is limited to subsections of the case study section.

3. Geophysical Techniques and Landslides: A “Landslide Approach” Analysis

As mentioned in Introduction, this review work is based on a “material landslide approach” analysis on the basis of the more recent landslide classification presented by [4] and discussed in Introduction. Even though this classification is not widely employed (only 20% of the analysed papers from the years 2015-2018 adopted it, and these papers are marked with # in Tables 2 and 3), we decided to use it considering that the same landslide could assume different names from paper to paper, though the authors could be more or less the same. Among the analysed papers, examples are the Super Sauze landslide and the La Vallette landslides (marked in Table 2 with (°) and (°°), respectively) or the Randa landslide (marked with (°) in Table 3). This means that the analysed works are clustered and discussed in two groups, “soil” and “rock,” respectively, on the basis of the material landslide type (columns 2 and 3 of Table 1).

Moreover, we decided to analyse the works starting from 2007 because the review in [20] is focused only on the ERT technique application; nevertheless, we do not analyse in detail all references already discussed therein, but we synthesize the results. The results of the review analysis are summarized in Tables 2 and 3, where for each work, we specify: (a) the landslide typology according the authors of the paper (i.e., how they refer to the landslide in the text) and (b) according to the classification from [4] (where possible, since sometimes it is not easy to identify the landslide classes from [4] on the basis of only the text); (c) the materials involved in the landslides; (d) which geophysical methods and (e) which other traditional techniques were employed; and (f)-(l) how many efforts were performed to overcome the five drawbacks highlighted by [11] and listed in Introduction. To quantify these efforts, a three-level scale was employed, where +, -, and n.d. mean, respectively, that many/some, insufficient, and nondiscussed efforts were made to overcome the limitations. Unfortunately, we know that the evaluation of how many efforts were performed could seem subjective. Therefore, in Table 4, for each drawback, we summarize how we evaluated the efforts.

3.1. “Soil” Landslides. “Soil” landslides, with respect to “rock” landslides, are the typology most studied with geophysical techniques. Among the 120 analysed papers, more than half (e.g., 66 papers, which means 75 landslides analysed without considering those reported in [20]) were about “soil” landslides, and among them, more than half were on the flow type. As summarized in Table 5, in fact, no one was focused on falls, topples, or spreads, while 28 landslides (the 37.3%) were analysed focused on the slide (6 clay/silt rotational slides, 8 clay/silt planar slides, 11 rotational and planar slides, 1 debris slide, and 2 clay/silt compound slides), 41 (the 54.6%) on the flows (5 sensitive clay flowslides, 9 debris flows, 5 mud flows, and 22 earthflows), and 6 (the 8.1%) on the slope deformations (soil slope deformation). Only two of the analysed landslides were marine landslides [33, 35], indicating that it is not easy to conduct geophysical surveys to characterize landslides that dive into the sea. It is also

TABLE 2: This table summarizes the analysed scientific papers from the last twelve years (2007-2018) focused on “soil landslide”. The landslide typology and materials are defined as in the papers themselves. Moreover, where possible, we added the landslide classification according to [4]. Papers marked with # already adopted this classification. Papers marked with (°) and (°°) focus on the Super Sauze and La Vallette landslides, respectively. Drawbacks 1 to 5 are the limitations of the geophysical techniques applied to landslide characterizations pointed out by [11]. They are, respectively, as follows: *Drawback 1*: geophysicists have to make an effort in the presentation of their results; *Drawback 2*: the resolution and the penetration depth of each method are not systematically discussed in an understandable way; *Drawback 3*: the geological interpretation of geophysical data should be more clearly and critically explained; *Drawback 4*: the challenge for geophysicists is to convince geologists and engineers that 3D and 4D geophysical imaging techniques can be valuable tools for investigating and monitoring landslides; and *Drawback 5*: efforts should also be made towards obtaining quantitative information from geophysics in terms of geotechnical parameters and hydrological properties. +, -, and n.d. mean, respectively, that many/some, insufficient, and non-discussed efforts were made to overcome the limitations (see Table 4), while +* means that the interpretation is linked to a numerical model or landslide feature identification. VES: vertical electrical sounding, ERT: electrical resistivity tomography, IP/SIP: induced polarization/spectral induced polarization, SP: self-potential, SPT: self-potential tomography, F/TDEM: frequency/time domain electro magnetism, VLF-EM: very low-frequency electro magnetism, EM: electro magnetism, RMT: radio magnetotelluric, AE: acoustic emission, SN: seismic noise, SR: seismic refraction, SR: seismic reflection, SW: surface waves, DH: downhole, CH: crosshole, GPR: ground penetrating radar, MG: micro gravity, DTM: digital terrain model, SAR: synthetic aperture radar, GB-InSAR: ground based interferometric SAR, GPS: global position system, TS: total station, TLS: terrestrial laser scanners, CPT: cone penetration test, TDR: time domain reflectometry.

Year	Reference	Landslide typology (as defined by the author/s)	Landslide typology (according [4])	Material	Geophysical Technique/s	Other available data	Drawback 1	Drawback 2	Drawback 3	Drawback 4	Drawback 5
2007	[22] (°)	mudslide	earthflow	clay formation	SN (local)	GPS, geodetic and strain instrument, piezometer	-	n.d.	n.d.	n.d.	n.d.
2007	[23]	earthflow (the oldest movement), clay planar slide (reactivations)	earthflow	clay body over mudstone-shale basement	ERT, SR, SW, SN (local), DH	SAR data, inclinometers, stratigraphy	+	+	-	n.d.	n.d.
2007	[24]	/	/	mudstone, colluvium, limestone and carbonate breccia	SN (regional)	/	-	n.d.	-	n.d.	+
2007	[25] (°)	intra-material mudslide	earthflow	clay formation	SR, ERT, SW, SN (local)	boreholes	+	-	+	n.d.	+
2007	[26]	rock and debris flows	rock avalanche and debris flows	/	SN (local)	/	-	n.d.	++	n.d.	n.d.
2007	[27] (°)	(a) soft-rock (mudslide or clayey flow-like landslide) (b) translational landslide	(a) earthflow (b) clay planar landslide	clay formation	SN (local), ERT	(a) geology, geomorphology, geotechnics and hydrology (b) geomorphology and geotechnics	+	+	-	-	n.d.
2008	[28]	earthflow	earthflow	loess	ERT, SR, SN (local)	DEM	-	n.d.	+	n.d.	+

TABLE 2: Continued.

Year	Reference	Landslide typology (as defined by the author/s)	Landslide typology (according [4])	Material	Geophysical Technique/s	Other available data	Drawback 1	Drawback 2	Drawback 3	Drawback 4	Drawback 5
2008	[29]	/	/	mudstone, colluvium, limestone and carbonate breccia	SN (local)	/	-	n.d.	-	n.d.	+
2009	[30]	debris flow	debris flow	metasediments, gneisses, quartzites	SN (local)	meteorological data	+	n.d.	++	n.d.	n.d.
2009	[31]	earthflow	earthflow	flysch, calcareous Alps	SRe	boreholes, DEM	-	n.d.	+	n.d.	n.d.
2009	[32]	earthflow	earthflow	coarse components in silty-clayey matrix	SR, SRe	boreholes	-	n.d.	n.d.	n.d.	n.d.
2009	[33]	/	clay rotational and planar slide	/	SRe	/	-	-	-	n.d.	n.d.
2010	[34]	sandy-clay translational landslide	clay planar slide	marly limestone	ERT	piezometer, field observations, boreholes	-	n.d.	+	n.d./+	+
2010	[35]	translational slope landslide	clay rotational slide, sensitive clay flowslide	marine and glaciomarine clay (Fjord-deltaic sediments)	seismic sub-bottom profile	boreholes, CPT, geotechnical test, trenches, bathymetric data	+	n.d.	+	n.d.	n.d.
2010	[36]	deep landslide	clay/silt rotational slide, mud flow	glaciolacustrine clays	SN (local)	inclinometers, boreholes, GPS	+	n.d.	+	+/n.d.	n.d.
2010	[37]	debris slide	debris slide	schist and gneiss	VLF-EM, VES	boreholes, TS	-	n.d.	-	n.d.	n.d.
2010	[38]	composite multiple earth slide – earth flow	earth flow	mudstone, sandstone	ERT	GPS	+	+	-	n.d./+	n.d.
2011	[39]	deep-seated landslide	soil slope deformation	coarse colluvium over mudstone	SN (local)	/	-	n.d.	+	n.d.	+

TABLE 2: Continued.

Year	Reference	Landslide typology (as defined by the author/s)	Landslide typology (according [4])	Material	Geophysical Technique/s	Other available data	Drawback 1	Drawback 2	Drawback 3	Drawback 4	Drawback 5
2011	[40]	/	clay compound slide	sandy, silty clay	SN (local)	meteorological data, extensometers, SR, robotic TS	-	n.d.	+	n.d.	-
2012	[41]	clayey landslide	earthflow	black marls	SR	geometrical model, DEM	+	-	+	n.d.	n.d.
2012	[42]	many	/	black marl	ERT, SR, SW	/	-	n.d.	+	n.d.	+
2012	[43] (°)	intra-material landslide	rotational and planar slide, mud flow	clay-shale deposits	ERT, SR, SW	/	-	-	+	n.d.	+
2012	[44]	debris flow complex retrogressive rot-translational slide	debris flow	/	SN (regional)	/	-	n.d.	++	n.d./-	n.d.
2012	[45]		rotational and planar slide	schist, flysch	ERT	TDR, weather station	+	n.d.	-	n.d./+	-
2012	[46] (°)	flow-like landslide	rotational and planar slide, mud flow	black marls	3D-SR	boreholes, SR, ERT	+	n.d.	+	+/n.d.	n.d.
2012	[7] (°)	flow-like landslides (mudslides)	earthflow	/	SR, ERT, GPR, EM, MG	many	+	+	+	n.d	n.d.
2012	[47]	deep-seated landslide	soil slope deformation	/	SN (regional)	/	-	n.d.	++	n.d.	n.d.
2013	[48]	quick clay landslide	sensitive clay flow-like	clay	ERT, IP	resistivity CPT, geotechnical test	-	n.d.	+	n.d	n.d.
2013	[49]	deep-seated landslide	soil slope deformation	clay-rich formation and colluvial deposits	SN (local)	/	-	-	+	n.d.	n.d.
2013	[50]	shallow landslide	planar slide-earthflow	silty sand, marlstone, sandstone	ERT	TRD, tensiometer	-	-	+	n.d./+	+

TABLE 2: Continued.

Year	Reference	Landslide typology (as defined by the author/s)	Landslide typology (according [4])	Material	Geophysical Technique/s	Other available data	Drawback 1	Drawback 2	Drawback 3	Drawback 4	Drawback 5
2013	[51]	earth flow (quick clay landslide)	sensitive clay flowslide	quick clay	2D and 3D SR, SRe, SN (local), 2D and 3D ERT, EM, GPR, RMT, MG	boreholes, CPT, LiDAR, geotechnical test	-	n.d.	+	-/n.d.	n.d.
2013	[52]	earth flow (quick clay landslide)	sensitive clay flowslide	quick clay	SRe	boreholes, CPT, LiDAR, geotechnical test, ERT, IP	-	n.d.	+	-/n.d.	n.d.
2013	[53]	/	clay/silt rotational slide	gravel, sand, and plastic and non-plastic fines from quartzite, phyllite, slate, and limestone	ERT, IP, MG	geotechnical analysis	-	n.d.	-	n.d.	n.d.
2013	[54]	surficial failures along a planar soil/rock interface	clay/silt planar slide	clayey sand, silty sand, sandstone	ERT	boreholes, geotechnical analysis, meteorological station, TDR, piezometer	-	n.d.	-	n.d./-	+
2013	[55]	muddy landslide	debris flow, rock fall	(a) black marls, (b) flysch and clay-shale	SN (local)	/	-	n.d.	++	n.d.	n.d.
2013	[9]	mudslide and rotational/planar slide (^{av})	planar slide	black marls, flysch	SR	LiDAR, TLS, field investigations, GPS, DEM	+	n.d.	+	n.d.	n.d.
2013	[56]	deep-seated landslide	soil slope deformation	/	SN (local)	LiDAR	-	n.d.	++	n.d.	n.d.
2014	[57]	translational slide	clay planar slide	clay sandy calcarene succession	2D and 3D ERT, SR, SN (local), SW	boreholes	+	n.d.	+	+/n.d.	n.d.
2014	[58]	/	/	/	SN (local)	/	-	n.d.	n.d.	n.d.	+
2014	[59]	composite rotational landslide (complex landslide)	clay rotational landslide	marls, chalks	ERT, SR	field investigation, aerial orthophotographs, LiDAR, boreholes, DEM	+	n.d.	+	n.d.	n.d.

TABLE 2: Continued.

Year	Reference	Landslide typology (as defined by the author/s)	Landslide typology (according [4])	Material	Geophysical Technique/s	Other available data	Drawback 1	Drawback 2	Drawback 3	Drawback 4	Drawback 5
2014	[60]	complex, composite, successive earth-slide earth flow	clay/silt rotational slide, earthflow	mudstone	ERT	boreholes, LiDAR, aerial photos, DEM, GPS, inclinometer	-	n.d.	+	+ / n.d.	-
2014	[20]	many	/	many	ERT (ERT technique review paper)	many	+	-	-	+ / +	n.d.
2014	[61]	deep-seated gravitational deformation dismantled into slides and flows	clay/silt rotational and planar slide, earthflow, creep	boulders, gravel and coarse sand over argillites and limestone	SRe, ERT	inclinometers, boreholes, SR	+	n.d.	-	n.d.	n.d.
2014	[62]	(a) and (b) rotational- translational landslide	(a) and (b) clay rotational/planar slide	(a) colluvium, (b) colluvium and amphibolite	ERT	inclinometer, 3D displacement measures, piezometric water level, soil temperature	+	+	+	n.d. / +	n.d.
2015	[63] (#)	debris flow	debris flow	glacial till, outwash sediments	SN (regional)	LiDAR, GIS, numerical modelling	+	n.d.	++	n.d.	n.d.
2015	[64]	debris flow	debris flow		SN (regional)	/	-	n.d.	++	n.d.	n.d.
2015	[65]	earth-flow	earthflow	sandstone and limestone	ERT	GPS	+	n.d.	n.d.	+	n.d.
2015	[66]	earthflow	earthflow	marl, claystone, mudstone, alluvium, limestone	ERT, SP,	/	-	n.d.	+	n.d.	n.d.
2016	[67] (#)	shallow clay planar slide	clay planar slide	plastic blue marls, limestone, blue clays	ERT	GPS, aerial photo, boreholes, auger and penetration, geotechnical analysis, rainfall and groundwater level data	+	-	+	n.d.	n.d.
2016	[68] (°)	clayey landslide	earthflow	black marls	ERT	/	+	+	+	n.d. / +	-

TABLE 2: Continued.

Year	Reference	Landslide typology (as defined by the author/s)	Landslide typology (according [4])	Material	Geophysical Technique/s	Other available data	Drawback 1	Drawback 2	Drawback 3	Drawback 4	Drawback 5
2016	[69]	shallow creeping landslide	soil slope deformation	clayey silt, mild clay and gravelly sand, covered by grass peat and turf. (bedrock: mudstone, sandstone)	ERT, GPR	boreholes	-	n.d.	-	n.d.	n.d.
2016	[70] (#)	debris flow	debris flow	sandstone, claystone, siltstone, volcanic rocks, Quaternary sediments	ERT, EM, SP, MG	gamma-ray, soil Radon, boreholes, GPS	-	n.d.	-	n.d.	n.d.
2016	[71]	translational landslide	clay/silt planar slide	silty clay with gravels over sandstone and mudstone	ERT	boreholes, inclinometers, piezometers, pluviometer, osmometer	+	n.d.	+	n.d./-	n.d.
2016	[72]	quick-clay landslide	sensitive clay flowslide	quick clay	FDEM, ERT, SR, SW	LiDAR, geotechnical test, resistivity-CPT, boreholes	+	n.d.	+	n.d.	n.d.
2016	[73]	loess landslide	clay/silt rotational slide	sandy and clayey loess	ERT	/	-	-	+	n.d.	+
2016	[74] (#)	multiple earth slide-earth flow	earth flow	mudstone, sandstone	SR	3D-ERT, geotechnical analysis	+	-	+	n.d.	-
2016	[75]	complex landslide	clay compound slide	clays, sands, gravels	SW, SN (local), VES	borehole	+	-	+	n.d.	n.d.
2017	[10]	(a), (b) complex roto-translational landslide	(a) clay/silt rotational and planar slide (b) clay/silt rotational and planar slide, earthflow	limestone	SN (local)	boreholes, inclinometers,	+	n.d.	-	+/n.d.	n.d.
2017	[76]	debris flow	debris flow	schists, dolobrecias, quartzites	SN (local)	flow stage sensors	-	n.d.	++	n.d.	n.d.
2018	[77]	Sackung-like movement	soil slope deformation	sandstone, colluvium Quaternary deposits	ERT, SR, SN (local)	boreholes, geotechnical analysis, DEM, remote images, GPS	+	n.d.	+	n.d.	n.d.

TABLE 2: Continued.

Year	Reference	Landslide typology (as defined by the author/s)	Landslide typology (according [4])	Material	Geophysical Technique/s	Other available data	Drawback 1	Drawback 2	Drawback 3	Drawback 4	Drawback 5
2018	[78]	flow-like landslide	rotational and planar slide, mud flow	sandstone, limestone	IP, SIP	LiDAR, GPS, boreholes geotechnical analysis, ERT, SR	+	-	+	n.d.	n.d.
2018	[79]	roto-translational slide, earth slide and flows	clay/silt rotational and planar slide, earthflow	flysch, metamorphic rocks	SN (local), ERT	DTM, aerial images	-	n.d.	+	n.d.	n.d.
2018	[80]	/	earth flow (?)	sandstone, shale, coal shale, marl, clay, silt	ERT	boreholes, geotechnical analysis, SPT, field investigations	+	-	+	n.d./+	+
2018	[81]	(a) mudflow, (b) debris flow	(a) mud flow, (b) debris flow	/	SN (local), AE	ultrasonic gauge, video cameras	+	n.d.	++	n.d./-	n.d.
2018	[82]	loess landslide	clay/silt rotational slide	clayey and sandy loess	ERT	pressure pore	-	n.d.	+	n.d.	n.d.
2018	[83] (#)	(a), (b) clay-rich debris slide (clayey landslide)	(a), (b) earthflow	clay-rich matrix, marls and limestone	SN (local)	/	+	n.d.	++	n.d.	n.d.

TABLE 3: This table summarizes the analysed scientific papers from the last twelve years (2007-2018) focused on “rock landslide”. Landslide typology and materials are defined as in the papers themselves. Moreover, where possible, we added the landslide classification according to [4]. Papers marked with # already adopted this classification. Papers marked with (‘) focus on the Randa landslides. Drawbacks 1 to 5 are the limitations of the geophysical techniques applied to landslide characterizations pointed out by [11]. They are, respectively, as follows *Drawback 1*: geophysicists have to make an effort in the presentation of their results; *Drawback 2*: the resolution and penetration depth of each method are not systematically discussed in an understandable way; *Drawback 3*: the geological interpretation of geophysical data should be more clearly and critically explained; *Drawback 4*: the challenge for geophysicists is to convince geologists and engineers that 3D and 4D geophysical imaging techniques can be valuable tools for investigating and monitoring landslides; and *Drawback 5*: efforts should also be made towards obtaining quantitative information from geophysics in terms of geotechnical parameters and hydrological properties. +, -, and n.d. mean, respectively, that many/some, insufficient, and non-discussed efforts were made to overcome the limitations (see Table 4), while ++ means that the interpretation is linked to a numerical model or landslide feature identification. VES: vertical electrical sounding, ERT: electrical resistivity tomography, IP/SIP: induced polarization/spectral induced polarization, SP: self-potential, SPT: self-potential tomography, F/TDEM: frequency/time domain electro magnetism, VLF-EM: very low-frequency electro magnetism, EM: electro magnetism, RMT: radio magnetotelluric, AE: acoustic emission, SN: seismic noise, SR: seismic refraction, SRe: seismic reflection, SW: surface waves, DH: downhole, CH: crosshole, GPR: ground penetrating radar, MG: micro gravity, DTM: digital terrain model, SAR: synthetic aperture radar, GB-InSAR: ground based interferometric SAR, GPS: global position system, TS: total station, TLS: terrestrial laser scanners, CPT: cone penetration test, TDR: time domain reflectometry.

Year	Reference	Landslide typology (as defined by the author/s)	Landslide typology (according [4])	Material	Geophysical Technique/s	Other available data	Drawback 1	Drawback 2	Drawback 3	Drawback 4	Drawback 5
2007	[84]	Rockfall/debris flows	rock fall, debris flow	basaltic	SN (local)	/	-	n.d.	++	n.d.	n.d.
2007	[85]	rock fall	rock fall	limestone	GPR	boreholes, mining	-	-	+	n.d.	n.d.
2007	[26]	rock and debris flows	rock avalanche and debris flows	/	SN (local)	/	-	n.d.	++	n.d.	n.d.
2007	[86] (‘)	rock fall	rock fall	heterogeneous gneisses	SN (local), 3D-SRT	boreholes, GPR, geodetic, geotechnical, meteorological monitoring system	+	n.d.	-	+ / n.d.	n.d.
2008	[87]	rock fall	rock fall	limestone	ERT, GPR	TLS, photogrammetry	+	-	++	n.d.	n.d.
2008	[88]	rock fall and rock-fall avalanches	rock fall and rock avalanche	limestone, amphibolite, granite	SN (regional)	/	-	n.d.	++	n.d.	n.d.
2008	[89]	rockfall	rock fall	lava dome	SN (regional)	/	-	n.d.	++	n.d.	n.d.
2008	[90]	rotational sliding	rockslide (any specific typology emerged)	marl and schist	airborne EM, ERT, geophysical logs, SP	boreholes, geotechnical test, hydrophysical logs, DEM, gamma ray spectrometer, inclinometers	-	-	+	n.d/-	n.d.

TABLE 3: Continued.

Year	Reference	Landslide typology (as defined by the author/s)	Landslide typology (according [4])	Material	Geophysical Technique/s	Other available data	Drawback 1	Drawback 2	Drawback 3	Drawback 4	Drawback 5
2008	[91]	rockfall (artificial)	rock fall	/	SN (local)	videos, photos	+	n.d.	++	n.d.	-
2008	[92] (°)	rockslide	rock wedge slide	heterogeneous gneisses	SR, GPR,	boreholes, field mapping	+	-	+	-/n.d.	n.d.
2009	[93]	rockfall	rock fall	metalliferous limestone	SN (local)	TS, TLS	+	+	-*	n.d.	n.d.
2009	[94]	rock-fall	rock fall	chalk	SN (local)		+	n.d.	-*	n.d.	n.d.
2010	[95]	rockfall	rock fall	othogneisses	SN (local)	thermometer	-	n.d.	-*	n.d.	n.d.
2010	[96]	rockslide	rock block toppling	heterogeneous gneisses	SN (local)	GPS	+	n.d.	++	n.d.	n.d.
2010	[97]	rockslide	rock compound slide	meta-granodiorite and two-mica gneiss	SN (local)	GPS, meteorological data	-	n.d.	+	n.d.	n.d.
2010	[98]	rock slice collapse	rock rotational slide	limestone	SN (local)	extensometer	-	n.d.	++	n.d.	n.d.
2010	[99]	rockslide	rock fall	micaschists	SN (local)	meteorological station, GPS	+	n.d.	++	n.d.	n.d.
2010	[100]	rock fall	rock fall	limestone and marly limestone	SN (local), SR	extensometer	+	n.d.	++	n.d.	n.d.
2010	[101]	rock-ice avalanche	rock/ice avalanche	plutonic rocks	SN (regional)	DEM	-	n.d.	++	n.d.	n.d.
2010	[102]	deep-seated with several debris flow	rock slope deformation	flysh and evaporites	SR, SRe	/	+	n.d.	+	n.d.	n.d.
2011	[103]	rockslide	many	many	SN (regional)	/	-	n.d.	++	n.d.	n.d.
2011	[104]	rockfall	rock fall	volcanos	SN (local)	/	-	n.d.	++	n.d.	n.d.
2011	[105]	rockslide	rock fall	micaschists	SN (local)	GPS, boreholes	+	+	++	n.d.	n.d.
2011	[106]	rockfall	rock fall	limestone	SN (local), SR		-	n.d.	++	n.d.	n.d.

TABLE 3: Continued.

Year	Reference	Landslide typology (as defined by the author/s)	Landslide typology (according [4])	Material	Geophysical Technique/s	Other available data	Drawback 1	Drawback 2	Drawback 3	Drawback 4	Drawback 5
2011	[107]	rock slope	rock block toppling	paragneiss and schists	SN (local)	regional earthquakes, fibre optic strain sensors	+	n.d.	++	n.d.	n.d.
2011	[108]	rockslide (long-runout)	rock planar slide	flysch (clay- stone/mudstone sequence)	ERT	radiocarbon and dendrogeomorpho- logical analysis, geomorphic mapping, GPS, geotechnical analysis	+	n.d.	+	n.d.	n.d.
2011	[109]	deep-seated gravitational slope deformation	mountain slope deformation	flysch	ERT	field survey, kinematic analysis, trenches	+	-	+	n.d.	n.d.
2012	[110]	rock fall (precondition for)	rock fall	granitic gneiss	AE	meteorological data	-	-	++	n.d.	n.d.
2012	[111]	/	rock fall/rock block topple (?)	orthogneiss	SN (local)	/	+	n.d.	++	n.d.	n.d.
2012	[112]	rock-fall	rock fall	gneiss and gabbro	SN (local)	thermometers, GPS	-	n.d.	++	n.d./-	n.d.
2012	[113]	rockfall and lateral spreading	rock fall	limestone, clay formation	SN (local)		+	n.d.	+	n.d.	n.d.
2012	[114]	rockfall in the source area of a mudslide	rock fall	black marls	SN (regional)	extensometers, DEM	+	n.d.	++	n.d.	n.d.
2012	[115]	rockfall	rock fall	flysch, marls and limestone	SN (local)	meteorological and hydrological data, local seismicity	+	n.d.	++	n.d./-	n.d.

TABLE 3: Continued.

Year	Reference	Landslide typology (as defined by the author/s)	Landslide typology (according [4])	Material	Geophysical Technique/s	Other available data	Drawback 1	Drawback 2	Drawback 3	Drawback 4	Drawback 5
2013	[116]	rockslide-debris flow	rock irregular slide, debris flow	rhyodacite breccias, tuff	SN (regional)	/	-	n.d.	++	n.d.	-
2013	[117]	(a), (b), and (d) toppling/basal sliding, (c) rock compound slide	(a), (b), and (d) rock block topple, (c) rock compound slide	(a) argillites (b) and (d) limestone (c) shale- sandstone series	SN (local) (a) SR, (c) ST	meteorological station (a) displacement measures, (b) and (c) extensometers,	-	n.d.	+	n.d.	n.d.
2013	[118]	many: rockfall, debris avalanche any specific soil or rock emerged)	many (not specified) (any specific soil or rock emerged)	many (not specified)	SN (regional/catchment)	meteorological data, satellite images, aerial photos	+	n.d.	++	n.d.	n.d.
2013	[119]	plan and toppling failures	/	mainly claystone and siltstone	VES	DEM	-	n.d.	-	n.d.	n.d.
2013	[55]	muddy landslide	debris flow, rock fall	(a) black marls, (b) flysch and clay-shale	SN (local)	/	-	n.d.	++	n.d.	n.d.
2014	[120]	rockfall	/	limestone	SN (local)	LiDAR, photogrammetry, video cameras, extensometer, tiltmeter	+	n.d.	++	n.d.	n.d.
2014	[121]	rockfall	rock fall	volcanos	SN (local)	/	-	n.d.	++	n.d.	n.d.
2014	[122]	deep-seated landslide	mountain slope deformation	flysch, sandstone	ERT	field survey	+	n.d.	+	n.d.	n.d.
2015	[123]	rockslide	/	argillaceous materials intercalated with mudstone/limestone	ERT, VES, SR		-	n.d.	+	n.d.	n.d.
2015	[124] (#)	tilting and rock fall	rock slope spread	dolomite	ERT	TLS, GPS	+	n.d.	+	+/n.d	n.d.

TABLE 3: Continued.

Year	Reference	Landslide typology (as defined by the author/s)	Landslide typology (according [4])	Material	Geophysical Technique/s	Other available data	Drawback 1	Drawback 2	Drawback 3	Drawback 4	Drawback 5
2016	[125]	rockfall	rock fall	granite	CH, SR	geotechnical analysis, crackmeters, temperature probes, inclinometers, SN	-	n.d.	+	n.d.	+
2016	[126] (#)	21 landslides: 12 rock falls, 8 rock slides and 1 rock avalanche	21 landslides: 12 rock falls, 8 rock slides (any specific typology emerged) and 1 rock rock	many	SN (local)	/	-	n.d.	++	n.d.	n.d.
2016	[127]	rockslide	planar rockslide, rock fall, debris avalanche	dolomite	SN (regional)	/	-	n.d.	++	n.d./-	n.d.
2017	[128]	rockfall	rock fall	limestone	SN (local)	TLS	+	+	++	n.d.	n.d.
2017	[129]	rockfall	rock fall	limestone	SN (local)	GPS, photo camera	+	n.d.	++	n.d.	n.d.
2017	[130]	rock slide	rockslide (any specific typology emerged)	paragneiss	SW, SN	/	-	n.d.	+	n.d.	n.d.
2017	[131]	rockfall	rock fall	black marls	SN (local)	/	-	n.d.	++	n.d.	n.d.
2017	[132]	deep-seated landslide	mountain slope deformation	sedimentary rocks and flysch	ERT, GPR, SR, MG	field survey, GPS	+	-	+	n.d.	n.d.
2018	[133]	rockfall	rock fall	limestone	SN (local)	weather station, DEM	-	n.d.	++	n.d.	n.d.
2018	[134]	rock slide	rock compound slide, rock fall, debris avalanche	amphibolitic and augen gneiss	SN (local)	extensometers, meteorological station, GPS	+	n.d.	++	n.d.	n.d.
2018	[135]	rockfall	rock fall	limestone	SN (local)	extensometer, meteorological data	+	n.d.	-	n.d./-	n.d.

TABLE 4: For each drawback, this table explains how the three-level scale (+, -, and n.d., which mean that many/some, insufficient, and non-discussed efforts were made to overcome the limitations) was applied.

	+	-	n.d.
Drawback 1	(i) Coloured figures (ii) 3D figures (iii) Figures with interpretations	(i) B&W figures (ii) Non-interpreted figures (iii) Figures too small (iv) Only raw data	/
Drawback 2	There is wide discussion about the technique/s penetration depth and/or resolution	There are only some mentions of the technique/s penetration depth and/or resolution	There are no mentions of the technique/s penetration depth and/or resolution
Drawback 3	There is wide discussion about the geological interpretation of the geophysical data	There are only some mentions of the geological interpretation of the geophysical data	There are no mentions of the geological interpretation of the geophysical data
Drawback 4	3D/4D data are presented and discussed	3D/4D data are presented but they are not discussed in depth	No 3D/4D data are presented or discussed
Drawback 5	There is wide discussion on how to link geophysical data with geotechnical and/or hydrological properties	There are only some mentions of how to link geophysical data with geotechnical and/or hydrological properties	There are no mentions of how to link geophysical data with geotechnical and/or hydrological properties

TABLE 5: For each type of movement and “soil” landslide typology, the table summarizes how many papers are focused on it. In italic movement types that usually reach extremely rapid velocities as defined by [2], while for the others, the velocity varies between extremely slow to very rapid (for details, refer to [4]).

TYPE OF MOVEMENT	Number of papers	SOIL	Number of papers
Fall	/	<i>Boulder/debris/silt fall</i>	/
Topple	/	<i>Gravel/sand/silt topple</i>	/
Slide	28	Clay/silt rotational slide	6
		Clay/silt planar slide	8
		<i>Gravel/sand/debris slide</i>	1
		<i>Clay/silt compound slide</i>	2
Spread	/	<i>Sand/silt liquefaction spread</i>	/
		<i>Sensitive clay spread</i>	/
Flow	41	<i>Sand/silt/debris dry flow</i>	/
		<i>Sand/silt/debris flowslide</i>	/
		<i>Sensitive clay flowslide</i>	5
		<i>Debris flow</i>	9
		<i>Mud flow</i>	5
		<i>Debris flood</i>	/
		<i>Debris avalanche</i>	/
		<i>Earthflow</i>	22
		<i>Peat flow</i>	/
Slope Deformation	6	Soil slope deformation	6
		Soil creep	/
		Solifluction	/

important to point out that in our analysis, we do not consider papers focused on the geophysical characterization of quick-clay that could evolve into a sensitive clay flowslide but only papers focused on those that already occurred [35, 51, 52, 72].

In only 8 works (12.1% of the analysed “soil” landslide works), it is possible to find a detailed discussion of the theory

applied to landslides, concerning either how to formulate the inversion problem [41, 46, 52, 55, 68, 83] or how to combine data from different surveys [7, 42]. All the other papers deal with the discussion of a case study.

A detailed analysis of the applied techniques is discussed in Section 4. Below, we present only the main considerations

from some papers. ERT is an active geophysical method that can provide both 2D and 3D images of the subsoil. A wide review of this technique applied to landslides is provided in [20]. Therefore, here, we limit discussion to saying that in most papers (29 of 33 that present ERT applications, i.e., 88.0%), 2D ERTs are shown, while only in 6.0% (2 papers of 33), 3D ERTs are shown, and in the remaining 6.0% (2 papers of 33), both 3D and 2D applications are presented.

Since the '60s, passive seismic techniques have been developed to monitor and characterize signals triggered by landslide dynamics and related changes in the material mechanical properties (i.e., (i) material bending, shearing, or compression; (ii) fissure opening; (iii) slipping at the bedrock interface; and (iv) debris flows or mudslides) [22, 55]. They are of great interest in (a) detecting debris flows [30], (b) assessing site effects [24, 29], (c) detecting landslide slip surfaces [10], and (d) estimating the thickness of a material that could be mobilized by a landslide [136]. Another advantage of this method is its ability to detect remote events that might otherwise go unnoticed for weeks or months. The main difficulties arise from two issues: (i) the seismic signatures of landslides and mud/debris flows are very complex and cannot be effectively identified without a detailed waveform analysis and (ii) the epicentres of landslides and mud/debris flows cannot be confidently determined by conventional earthquake-locating methods, mainly due to the lack of clear arrivals of P and S phases [44].

3.2. "Rock" Landslides. Among the 120 analysed papers, less than half (e.g., 54) were about "rock" landslides, and the majority discussed were of the rock fall type. As summarized in Table 6 the landslide typology is divided as follows: 41 (the 54.6%) falls, 5 (the 6.7%) topples (5 block topples), 18 (the 24.0%) slides (1 rotational, 2 planar, 1 wedge, 3 compound, 1 irregular), 1 (the 1.3%) spread (rock slope spread), 6 (the 8.0%) flows (avalanches), and 4 (the 5.4%) slope deformations (3 mountain slope deformations and 1 rock slope deformation). In all the works that discuss the application of seismic techniques [26, 55, 84, 86, 87, 89, 91, 93–101, 103–107, 111–118, 120, 121, 126–128, 130, 131, 133, 134], it is possible to find a more- or less-detailed discussion on the theory of the seismic wave analysis carried out to find the "rock" landslide features.

"Rock" landslides are well-known phenomena but are poorly understood. Contrary to other landslide types, rock-falls are usually sudden phenomena with few apparent precursory patterns observed prior to the collapse. A key point in the prediction of rock slope failure is better knowledge of the internal structure (e.g., the persistence of joints), which requires an interdisciplinary research field among rock mechanics, rock engineering, and mining [98]. This is why in 64.8% of the analysed papers, the geophysical technique is carried out along with more traditional methods (i.e., boreholes, mining, extensometers, and inclinometers). Moreover, there are at least two limitations in applying geophysical methods for rock deposits: (a) the difficulty of deploying sensors (i.e., ER electrodes, geophones, or GPR antennas) on sharp and blocky ground with a high void ratio and (b) the low geophysical contrast between the rock deposit and the underlying layers with comparable properties [[137],

not listed in Table 3 because it was already analysed by [20]]. In [137], there is another limitation in applying geophysics for rock deposits: the presence of a shallow geophysical contrast caused by the subsoil water table that could mask deeper interfaces. Nevertheless, this limitation also has to be considered for "soil" landslides.

More recently, to overcome these limitations, rock slope stability characterization and monitoring has been carried out using passive seismic techniques (see also the discussion session), implemented initially in open-mine monitoring [98]. These techniques, in fact, could help in (i) understanding the seismic responses of rock to slope deformation (e.g., the release of stored elastic energy under particular conditions) [135, 138], (ii) detecting and locating microearthquakes generated by fracturing within unstable rock masses (major effort is required for classifying seismic signals and extracting those related to landslides [86, 99, 129]), and (iii) identifying remote events that could otherwise go unnoticed for weeks or months. Therefore, these methods are applied to avalanches [26, 84, 101, 126], rock topplings [107, 111, 117, 134], rockslides [55, 96–99, 103, 116, 126, 127, 130], and rock falls or cliff failures [86, 88, 89, 91, 93–95, 100, 104–106, 112–115, 118, 120, 121, 126, 128, 131, 133]. Finally, some works are focused on finding the relation among "rock" landslides, displacement rate measurements, and meteorological (i.e., rain and temperature) parameters [95, 99, 100].

4. Discussion

Most studies focused on geophysical surveys are applied (a) to explore the subsoil for mineral deposits or fossil fuels, (b) to find underground water supplies, (c) for engineering purposes, and (d) for archaeological investigations [19]. Technological progress and the availability of cheaper computer electronic parts has allowed the improvement of more portable equipment and the development of 2D and 3D geophysical techniques [11, 12]. Therefore, the applicability of geophysical methods in landslide characterization has grown over the years. Starting from the state of the art of the geophysical techniques applied in landslide characterizations pointed out in [12], this review focused on the papers from the last twelve (2007–2018) years and tried to understand how many efforts have been made by the international scientific community to overcome the drawbacks. These geophysical techniques limitations are listed in Introduction. To reach the goal of this paper, contrary to the four reviews discussed in Section 2 [8, 11, 12, 14], the analyses of the geophysical method advantages and limitation were carried out on the basis of the latest landslide classification, which is mainly based on the involved materials and geotechnical properties [4]. Therefore, the 120 analysed papers were divided into two classes: "soil" (in red in the following figures) and "rock" (in green in the following figures), which account for 66 and 54 works, respectively.

Even though it is well known that it is better to integrate more than one geophysical technique because of the intrinsic limitations of each approach, in 68.3% of the analysed papers (Figure 1), only one geophysical method is presented and discussed. However, in 64.6% of these works (which

TABLE 6: For each movement type and “rock” landslide typology, the table summarizes how many papers are focused on it. In italic movement types that usually reach extremely rapid velocities as defined by [2], while for the others, the velocity varies between extremely slow to very rapid (for details, refer to [4]).

TYPE OF MOVEMENT	Number of papers	ROCK	Number of papers
Fall	41	<i>Rock/ice fall</i>	40
Topple	5	<i>Rock block topple</i>	5
		Rock flexural topple	/
Slide	18	Rock rotational slide	1
		<i>Rock planar slide</i>	2
		<i>Rock wedge slide</i>	1
		Rock compound slide	3
		<i>Rock irregular slide</i>	1
Spread	1	Rock slope spread	1
Flow	6	<i>Rock/ice avalanche</i>	6
Slope Deformation	4	Mountain slope deformation	3
		Rock slope deformation	1

correspond to 44.1% of the total analysed papers, as indicated by the bottom/darker part of the blue bar in Figure 1), the geophysical results are interpreted on the basis of other techniques. This means that only in 24.2% of the analysed works (the top/lighter part of the blue bar in Figure 1) is just one technique presented, and in 80% of these 24.2% (which means four works out of five), the employed method is a passive seismic technique. This is probably because these techniques (a) require quite light equipment, (b) can be employed to both monitor and characterize seismic signals triggered by landslide dynamics [55, 133, 134], and (c) can be useful for overcoming the unpredictable occurrence of rockfalls [128], even though it is not easy to correlate seismic signal features with landslide geological properties [120, 134].

In general, active and passive seismic methods are the most employed in landslide characterization and monitoring (Figure 2). In “soil” landslides, the three most employed techniques are ERT, SN (at local and regional scales), and SR. The last, together with SRe and SW, is largely used in this kind of landslide typology, and in general, it is easier to find papers focused on “soil” landslides that integrate the abovementioned seismic techniques with other less-common techniques (e.g., MG, IP, SP, and EM). Our analysis of “soil” landslides confirms the conclusions of [20]; i.e., (a) ERT and SR integration proves to be the most effective, (b) the joint application of ERT, SR, and GPR seems to solve and overcome the resolution problems of each single method, and (c) in the literature, there are very few examples of ERT combined with IP to distinguish clayey material or to better interpret ERT. In “rock” landslides, the three most employed techniques are SN (at local and regional scales), ERT, and SR, indicating that passive seismic techniques are preferred over electrical ones. As mentioned above, this is probably because they can be employed to both monitor and characterize seismic signals triggered by landslide dynamics [55, 133, 134]. At the fourth position is GPR, although the authors highlight both the difficulty of deployment on cliffs and the limitation of its applicability to only highly resistive rock slopes [87, 88, 92, 132].

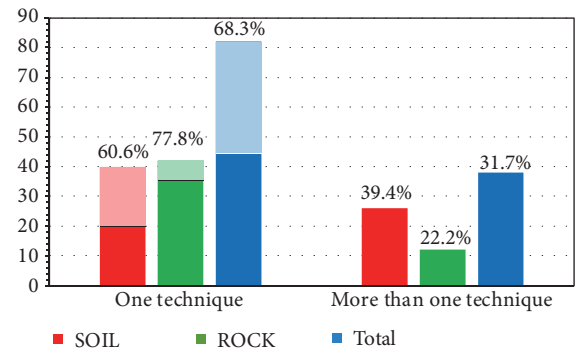


FIGURE 1: For each landslide typology (“soil” in red, “rock” in green, and total in blue), the bar graph shows the number of papers focused on just one technique or on more than one. Numbers on the top of the bars are the percentage values with respect to the total number of analysed papers. The darker colours of the “soil” and “rock” bars indicate in how many works the passive seismic technique was employed alone. The dark blue portion of the “one-technique total bar” indicates in how many works other nongeophysical techniques were employed.

In Figure 3, for each drawback, the percentages and the numbers of papers (numbers on the top of the bars) that fall into each level of the three-level scale (+, -, and n.d., which mean that many/some, insufficient, and nondiscussed efforts were made to overcome the limitations, as shown in Table 4) are summarized. In general, it is possible to observe that great efforts were made (95 papers out of the 120 analysed, which is 79.1%, are on the + level of the scale) to improve the geological interpretation of the geophysical data and to explain it more clearly and critically (drawback 3). In contrast, very few efforts were made to (a) systematically discuss, in an understandable way, the resolution and penetration depth of each method (drawback 2: 91 papers out of the 120 analysed, which are 75.8%, are on the n.d. level of the scale), (b) to convince geologists and engineers that 3D and 4D geophysical imaging techniques can be valuable tools for investigating and monitoring landslides (drawback

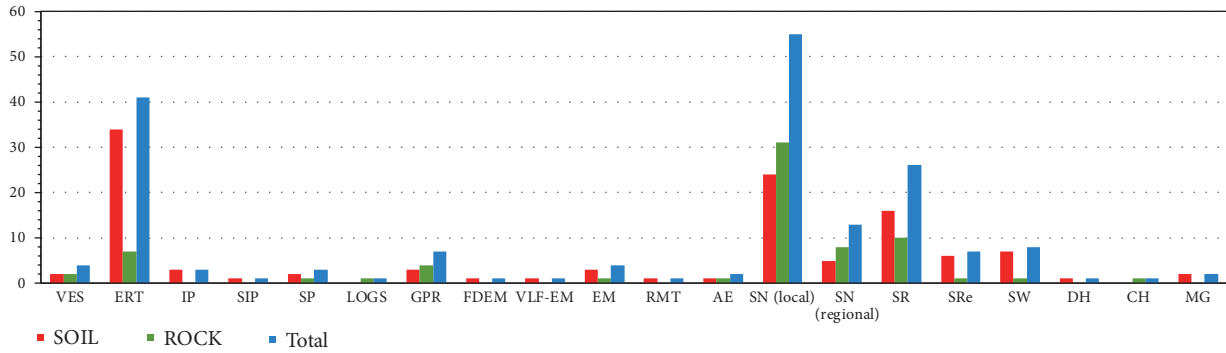


FIGURE 2: For each landslide typology (“soil” in red, “rock” in green, and total in blue), the bar graph shows the number of papers focused on each geophysical method.

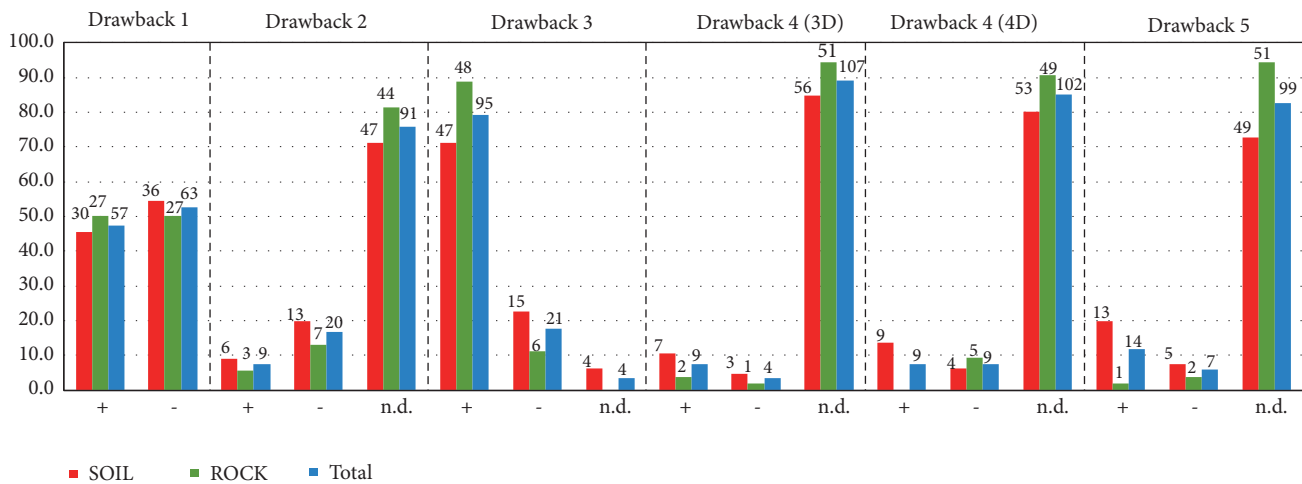


FIGURE 3: The bar graph indicates the percentage of efforts made (+ means many/some, - means insufficient, and n.d. means nondiscussed) to overcome each drawback. The percentages of papers focused on “soil” landslides are in red, those of papers focused on “rock” landslides are in green, while in blue are the total percentages. The numbers on the top of each bar indicate the numbers of papers.

4: 107 papers for 3D applications and 102 papers for 4D applications out of the 120 analysed, which are 89.2% and 85.0%, respectively, are on the + level of the scale), and (c) to obtain quantitative information in terms of geotechnical parameters and hydrological properties from geophysical data (drawback 5: 99 papers out of the 120 analysed, which are 82.5%, are on the n.d. level of the scale). Finally, thanks to the development of new 2D and 3D imaging software, some efforts, but still not enough (57 papers out of the 120 analysed, which is 47.5%, are on the + level of the scale), were made to show the geophysical results more clearly (drawback 1).

In the following discussion, we analyse point-by-point the efforts made to overcome each drawback highlighted by [11].

Drawback 1: Geophysicists Have to Make an Effort in the Presentation of Their Results. According to our analysis (Figure 3), the efforts to overcome this drawback were performed more or less in the same way for both “soil” and “rock” landslides. This means that a tendency to show and present the results more objectively is beginning to emerge. This could be possible thanks to the development of new 2D and 3D software that allow the integration of data from

different sources and surveys (e.g., geophysical, geotechnical, and borehole data). Nevertheless, the presentation of seismic data is sometimes still hard, since authors often show the rough traces or spectra (e.g., [22, 24, 26, 29, 39, 40, 44, 47, 49, 55, 56, 58, 64, 76, 84, 89, 95, 97, 98, 101, 103, 104, 106, 112, 116, 117, 121, 126, 127, 131, 133]) that could be difficult to read for a nonexpert audience.

Drawback 2: The Spatial Resolution and Penetration Depth of Each Method Are Not Systematically Discussed in an Understandable Way. Each technique has a different resolution and penetration depth that contribute to the final quality of a geometrical model. According to [7], several preprocessing steps are needed to carefully check the data quality and, therefore, the resolution and penetration depth before incorporation into a 3D model. In total, 75.8% of the analysed papers (47 of those on “soil” landslides and 44 of those on the “rock” type) do not discuss either the resolution or the penetration depth of the presented methodology (Figure 3). Additionally, in the review in [20], none of the cited papers within the year range (2007-2013) examine these two points. In contrast, in the remaining 24.2% (Figure 3) of the examined works,

these two points are discussed more in depth in nine papers [7, 23, 27, 38, 62, 68, 93, 105, 128], and only few words are presented in the other twenty [25, 33, 41, 43, 49, 50, 67, 73–75, 78, 80, 85, 87, 90, 92, 108, 110, 132]. Therefore, most of the authors who present the results of an integrated survey do not discuss how to consider and combine these data. It is possible to conclude that this drawback has still not been overcome since 2007 and the review in [11].

Drawback 3: The Geological Interpretation of Geophysical Data Should Be More Clearly and Critically Explained. The 3D internal structural characterization of a slope/cliff is essential to any landslide stability analysis and to hydro-mechanical modelling [7]. Nevertheless, interdisciplinary aspects between geomorphological and geophysical data/results are poorly addressed [19]. According to our review (Figure 3), in 79.2% of the analysed papers (47 of those on “soil” landslides and 48 of those on the “rock” type), many efforts have been made to interpret, show, and explain the geophysical data in a more clear and critical way. However, almost 50.0% of these works (those marked with +* in Tables 2 and 3, which total 11 of 47 for “soil” landslides and 36 of 48 for the “rock” type) involve passive seismic monitoring and data analysis and interpretation to (a) provide information on slope dynamics and (b) identify landslide features. Moreover, it is worthwhile to note that the geophysical data interpretations are still not indisputable. In many papers, in fact, the discussion of the results is accompanied by words such as “suspect,” “suppose,” “speculate,” “probably/probable,” “potential,” “our preferred interpretation,” and “provide important information on possible” [9, 22, 25–27, 35, 38–40, 42–44, 46, 48–53, 57, 58, 63, 68, 72, 74, 75, 77, 85, 86, 96, 99, 101, 102, 104, 106, 108–110, 112, 114, 115, 118, 122, 126, 134]. Without close collaboration between geophysicists and geomorphologists, the accurate and effective use of geophysical techniques, as well as the corresponding data interpretation, is often very limited [19].

Drawback 4: The Challenge for Geophysicists Is to Convince Geologists and Engineers That 3D and 4D Geophysical Imaging Techniques Can Be Valuable Tools for Investigating and Monitoring Landslides. In the hydrocarbon industry, the best strategy for reconstructing a high-resolution model is acquiring a 3D data set [31]. On the other hand, there are interesting results from the noninvasive time-lapse monitoring of the hydrological behaviour of a mountain slope [139]. However, in 89.2% of the analysed works (Figure 3) 3D geophysical imaging is not discussed. Even though the 3D volumetric reconstruction of a landslide is a suitable target with new technologies [46, 60, 65, 92], a 3D survey could be very tiring, exhausting, and time-consuming, since it is still difficult to carry and move the equipment over the slope [18, 20]. To overcome this limitation, the acquisition is usually performed by means of 2D parallel profiles, and the results are shown in a 3D fence diagram [[20] and references within, [27, 51, 52, 57, 86, 92, 124]]. Thus, this drawback highlighted by [11] has not been overcome and is still a challenge for geophysicists.

Passive seismic monitoring could be considered a 4D technique, but none of the authors refer to this method in this

way. Therefore, in our analysis, we also have not considered it as a 4D technique, and the results show that in 85% of the works (Figure 3), 4D geophysical imaging is not discussed. In general, 4D ERT has been more frequently employed thanks to the development of ER multichannel measuring systems that significantly reduced the acquisition time [20, 140]. These systems [such as those employed in [141, 142]], in fact, (i) are able to simultaneously acquire a number of potential measurements for a single pair of current electrodes and (ii) can be set up to provide ERT at specific times during the day. Nevertheless, even though tl-ERTs could be helpfully employed in landslide monitoring, since they could provide information about the water content changes (i.e., the data could be related to pore water pressure variations and, therefore, to landslide triggering mechanisms), there are still few examples of 4D ERTs in landslide areas [60, 65, 92]. Moreover, it is still needed to improve software such that it is able to (i) continuously (or very frequently) process acquired data (e.g., ErtLab by Geostudy Astier, [140]), (ii) to link ER variations with hydrological parameter changes, and (iii) to take into account that the positions of the electrodes could change over the time because of the landslide movement [38, 65].

Drawback 5: Efforts Should Also Be Made towards Obtaining Quantitative Information from Geophysics in Terms of Geotechnical Parameters and Hydrological Properties. Authors agree that seismic wave velocities and soil ER could be useful in identifying anomalies related to structural (faults, fissures, and stability), lithological (sand to clay or calcareous variations) and hydrological (moisture, water flow) conditions [42, 123, 143]. However, drillings and inclinometer measurements are still crucial to providing a reliable idea of landslide structures and slip surfaces and to validate any geophysical measurements. This is probably because the geophysical property ranges cover several orders of magnitude, and a measured parameter cannot be directly assigned to a sure substrate. Currently, the major difficulty of applying geophysical techniques to landslides, as also highlighted by [11], is still the complex relationship between the measured geophysical parameters and the desired geotechnical and hydrogeological properties, which prevents the provision, in terms of engineering properties, of a straightforward interpretation. Moreover, a very accurate and high-resolution survey can still only be done on a small landslide portion [23, 24, 27, 28, 38, 40, 46, 60, 78, 86, 92], as it is costly and time-consuming. As also pointed out by [143], this complexity in obtaining quantitative information from geophysical data is probably also caused by (a) the lack of knowledge about geophysics techniques in the geotechnical engineering/geological community and (b) engineers inclination to believe in soil and rock that they can see visually (borehole log), rather than in what they cannot see (geophysical signal).

These abovementioned limitations are confirmed by our analysis. In total, 82.5% of the works (99 of 120, Figure 3), in fact, do not discuss how to obtain quantitative information on geotechnical and hydrogeological properties from geophysical data. In the remaining 17.5% (21 works, 14 of those on “soil” landslides and 7 of those on the “rock” type), both seismic

and electrical methods are used in the same percentage (9 works focused on seismic methods, 8 on ER, and 4 on both seismic and ER methods). Thus, this drawback has still not been overcome, and laboratory surveys to establish a link between rock properties and geophysical data, as well as interdisciplinary communication and discussion, are the primary keys [90].

5. Conclusion

This review work analysed the papers published in open-access journals from 2007 until today, focusing on the application of geophysical techniques to landslides. It was based on a “material landslide approach” analysis and evaluated how many efforts were performed to overcome the five drawbacks highlighted by the last review, which dates to 2007, concerning geophysical techniques applied to landslide monitoring and characterization. To quantify these efforts, a three-level scale was employed (from many/some efforts to nondiscussed). In general, it is possible to observe that (i) many efforts were made to improve the geological interpretation of geophysical data and to explain the interpretations more clearly and critically (drawback 3); (ii) some efforts, but still not enough, were made to show geophysical results more clearly (drawback 1); and (iii) very few efforts were made to (a) systematically discuss, in an understandable way, the resolution and penetration depth of each method (drawback 2), (b) to convince geologists and engineers that 3D and 4D geophysical imaging techniques can be valuable tools for investigating and monitoring landslides (drawback 4), and (c) to obtain quantitative information in terms of geotechnical parameters and hydrological properties from geophysical data (drawback 5).

The most studied landslides are those of the flow type for “soil” landslide typology and those of the fall type for the “rock” category. From the “employed method” point of view, active and passive seismic methods are the most employed in landslide characterization and monitoring. The latest method is also able to remotely detect events that might otherwise go unnoticed for weeks or months, and therefore, it is widely employed. The three more frequently applied techniques, regardless the typology (“soil” or “rock”), are ERT, SN and SR, which are to both characterize and monitor the slope deformation. Finally, independently of the applied technique/s, a very accurate and high-resolution survey could be performed only on a small landslide portion, as it is costly and time-consuming.

Conflicts of Interest

The authors declare that they have no conflicts of interest.

References

- [1] T. J. Burke, D. N. Sattler, and T. Terich, “The socioeconomic effects of a landslide in western washington,” *Environmental Hazards*, vol. 4, no. 4, pp. 129–136, 2002.
- [2] D. M. Cruden and D. J. Varnes, “Landslide types and processes,” *Special Report - National Research Council, Transportation Research Board*, vol. 247, pp. 36–75, 1996.
- [3] D. J. Varnes, “Slope movement type and processes,” in *Landslides, Analysis and Control. Special Report 176*, R. L. Schuster and R. J. Krizek, Eds., pp. 11–33, Transportation Research Board, National Academy Of Sciences, Wash, DC., USA, 1978.
- [4] O. Hungr, S. Leroueil, and L. Picarelli, “The Varnes classification of landslide types, an update,” *Landslides*, vol. 11, no. 2, pp. 167–194, 2014.
- [5] O. Hungr, S. G. Evans, M. J. Bovis, and J. N. Hutchinson, “A review of the classification of landslides of the flow type,” *Environmental and Engineering Geoscience*, vol. 7, pp. 221–238, 2001.
- [6] D. J. Varnes, “Landslide types and processes,” in *Landslides and Engineering Practice, Special Report 28*, E. B. Eckel, Ed., pp. 20–47, Highway research board. National Academy of Sciences, Wash, DC., USA, 1954.
- [7] J. Travelletti and J. Malet, “Characterization of the 3D geometry of flow-like landslides: A methodology based on the integration of heterogeneous multi-source data,” *Engineering Geology*, vol. 128, pp. 30–48, 2012.
- [8] V. A. Bogoslovsky and A. A. Ogilvy, “Geophysical methods for the investigation of landslides,” *Geophysics*, vol. 42, no. 3, pp. 562–571, 1977.
- [9] J. Travelletti, J. Malet, K. Samyn, G. Grandjean, and M. Jaboyedoff, “Control of landslide retrogression by discontinuities: evidence by the integration of airborne-and ground-based geophysical information,” *Landslides*, vol. 10, no. 1, pp. 37–54, 2013.
- [10] V. Pazzi, L. Tanteri, G. Bicocchi, M. D’Ambrosio, A. Caselli, and R. Fanti, “H/V measurements as an effective tool for the reliable detection of landslide slip surfaces: Case studies of Castagnola (La Spezia, Italy) and Roccalbegna (Grosseto, Italy),” *Physics and Chemistry of the Earth, Parts A/B/C*, vol. 98, pp. 136–153, 2017.
- [11] D. Jongmans and S. Garambois, “Geophysical investigation of landslides : a review,” *Bulletin de la Société Géographique de France*, vol. 178, no. 2, pp. 101–112, 2007.
- [12] R. Hack, “Geophysics for slope stability,” *Surveys in Geophysics*, vol. 21, no. 4, pp. 423–448, 2000.
- [13] R. Fell, O. Hungr, S. leroueil, and W. Riemer, “Keynote paper – Geotechnical engineering of the stability of natural slopes and cuts and fills in soil,” in *Proceedings of The International Conference on Geotechnical & Geological Engineering in Melbourne, Australia*, vol. 1, pp. 21–120, Technomic Publishing, Lancaster, UK, 2000, ISBN: 1-58716-067-6.
- [14] D. M. McCann and A. Foster, “Reconnaissance geophysical methods in landslide investigation,” *Engineering Geology*, vol. 29, pp. 59–78, 1990.
- [15] F. Bruno and F. Marillier, “Test of high-resolution seismic reflection and other geophysical techniques on the Boup landslide in the Swiss Alps,” *Surveys in Geophysics*, vol. 21, no. 4, pp. 333–348, 2000.
- [16] A. Perrone, A. Iannuzzi, V. Lapenna et al., “High-resolution electrical imaging of the Varco d’Izzo earthflow (southern Italy),” *Journal of Applied Geophysics*, vol. 56, no. 1, pp. 17–29, 2004.
- [17] V. Naudet, M. Lazzari, A. Perrone, A. Loperte, S. Piscitelli, and V. Lapenna, “Integrated geophysical and geomorphological approach to investigate the snowmelt-triggered landslide of

- Bosco Piccolo village,” *Engineering Geology*, vol. 98, no. 3-4, pp. 156–167, 2008.
- [18] J. Chambers, P. Wilkinson, O. Kuras et al., “Three-dimensional geophysical anatomy of an active landslide in Lias Group mudrocks, Cleveland Basin, UK,” *Geomorphology*, vol. 125, no. 4, pp. 472–484, 2011.
- [19] L. Schrott and O. Sass, “Application of field geophysics in geomorphology: Advances and limitations exemplified by case studies,” *Geomorphology*, vol. 93, no. 1-2, pp. 55–73, 2008.
- [20] A. Perrone, V. Lapenna, and S. Piscitelli, “Electrical resistivity tomography technique for landslide investigation: a review,” *Earth-Science Reviews*, vol. 135, pp. 65–82, 2014.
- [21] A. Melehmir, L. V. Socco, M. Bastani et al., “Near-surface geophysical characterization of areas prone to natural hazards: a review of the current and perspective on the future,” *Advances in Geophysics*, vol. 57, pp. 51–146, 2016.
- [22] D. Amitrano, S. Gaffet, J. Malet, and O. Maquaire, “Understanding mudslides through micro-seismic monitoring: the super-sauze (South French Alps) case study,” *Bulletin de la Société Géographique de France*, vol. 178, no. 2, pp. 149–157, 2007.
- [23] P. Bordon, J. Haines, G. Di Giulio et al., “the cavola experiment team, 2007. cavola experiment site: geophysical investigation and deployment of a dense seismic array on a landslide,” *Annals of Geophysics*, vol. 50, pp. 627–649, 2007.
- [24] V. Del Gaudio and J. Wasowski, “Directivity of slope dynamic response to seismic shaking,” *Geophysical Research Letters*, vol. 34, no. 12, 2007.
- [25] G. Grandjean, J. Malet, A. Bitri, and O. Méric, “Geophysical data fusion by fuzzy logic for imaging the mechanical behaviour of mudslides,” *Bulletin de la Société Géographique de France*, vol. 178, no. 2, pp. 127–136, 2007.
- [26] C. Huang, H. Yin, C. Chen, C. Yeh, and C. Wang, “Ground vibrations produced by rock motions and debris flows,” *Journal of Geophysical Research: Atmospheres*, vol. 112, Article ID F02014, 2007.
- [27] O. Méric, S. Garambois, J.-P. Malet, H. Cadet, P. Guéguen, and D. Jongmans, “Seismic noise-based methods for soft-rock landslide characterization,” *Bulletin de la Société Géographique de France*, vol. 178, no. 2, pp. 137–148, 2007.
- [28] G. Danneels, C. Bourdeau, I. Torgoev, and H.-B. Havenith, “Geophysical investigation and dynamic modelling of unstable slopes: case-study of Kainama (Kyrgyzstan),” *Geophysical Journal International*, vol. 175, no. 1, pp. 17–34, 2008.
- [29] V. Del Gaudio, S. Coccia, J. Wasowski, M. R. Gallipoli, and M. Mucciarelli, “Detection of directivity in seismic site response from microtremor spectral analysis,” *Natural Hazards and Earth System Sciences*, vol. 8, no. 4, pp. 751–762, 2008.
- [30] A. Burtin, L. Bollinger, R. Cattin, J. Vergne, and J. L. Nábělek, “Spatiotemporal sequence of Himalayan debris flow from analysis of high-frequency seismic noise,” *Journal of Geophysical Research: Atmospheres*, vol. 114, no. F4, Article ID F04009, 2009.
- [31] C. G. Eichkitz, M. G. Schreilechner, J. Amtmann, and C. Schmid, “Shallow seismic reflection study of the Gschliefgraben landslide deposition area - Interpretation and three dimensional modeling,” *Austrian Journal of Earth Sciences*, vol. 102, no. 2, pp. 52–60, 2009.
- [32] R. Marschallinger, C. Eichkitz, H. Gruber, K. Heibl, R. Hofmann, and K. Schmid, “The Gschliefgraben landslide (Austria): A remediation approach involving torrent and avalanche control, geology, geophysics, geotechnics and geoinformatics,” *Austrian Journal of Earth Sciences*, vol. 102, no. 2, pp. 36–51, 2009.
- [33] E. Stucchi and A. Mazzotti, “2D seismic exploration of the Ancona landslide (Adriatic Coast, Italy),” *Geophysics*, vol. 74, no. 5, pp. B139–B151, 2009.
- [34] T. Lebourg, M. Hernandez, S. Zerathe, S. El Bedoui, H. Jomard, and B. Fresia, “Landslides triggered factors analysed by time lapse electrical survey and multidimensional statistical approach,” *Engineering Geology*, vol. 114, no. 3-4, pp. 238–250, 2010.
- [35] J.-S. L’Heureux, L. Hansen, O. Longva, A. Emdal, and L. O. Grande, “A multidisciplinary study of submarine landslides at the Nidelva fjord delta, Central Norway- Implications for geohazard assessment,” *Norsk Geologisk Tidsskrift*, vol. 90, no. 1-2, pp. 1–20, 2010.
- [36] F. Renalier, D. Jongmans, M. Campillo, and P. Bard, “Shear wave velocity imaging of the Avignonet landslide (France) using ambient noise cross correlation,” *Journal of Geophysical Research: Atmospheres*, vol. 115, no. F3, Article ID F03032, 2010.
- [37] S. P. Sharma, K. Anbarasu, S. Gupta, and A. Sengupta, “Integrated very low-frequency EM, electrical resistivity, and geological studies on the Lanta Khola landslide, North Sikkim, India,” *Landslides*, vol. 7, no. 1, pp. 43–53, 2010.
- [38] P. B. Wilkinson, J. E. Chambers, P. I. Meldrum, D. A. Gunn, R. D. Ogilvy, and O. Kuras, “Predicting the movements of permanently installed electrodes on an active landslide using time-lapse geoelectrical resistivity data only,” *Geophysical Journal International*, vol. 183, no. 2, pp. 543–556, 2010.
- [39] V. Del Gaudio and J. Wasowski, “Advances and problems in understanding the seismic response of potentially unstable slopes,” *Engineering Geology*, vol. 122, no. 1-2, pp. 73–83, 2011.
- [40] J. Gombert, W. Schulz, P. Bodin, and J. Kean, “Seismic and geodetic signatures of fault slip at the Slumgullion Landslide Natural Laboratory,” *Journal of Geophysical Research: Atmospheres*, vol. 116, no. B9, Article ID B09404, 2011.
- [41] J. Gance, G. Grandjean, K. Samyn, and J. Malet, “Quasi-Newton inversion of seismic first arrivals using source finite bandwidth assumption: application to subsurface characterization of landslides,” *Journal of Applied Geophysics*, vol. 87, pp. 94–106, 2012.
- [42] G. Grandjean, “A multi-method geophysical approach based on fuzzy logic for an integrated interpretation of landslides: application to the French Alps,” *Near Surface Geophysics*, vol. 10, no. 6, pp. 601–611, 2012.
- [43] C. Hibert, G. Grandjean, A. Bitri, J. Travelletti, and J. Malet, “Characterizing landslides through geophysical data fusion: Example of the La Valette landslide (France),” *Engineering Geology*, vol. 128, pp. 23–29, 2012.
- [44] H. Kao, C. Kan, R. Chen et al., “Locating, monitoring, and characterizing typhoon-induced landslides with real-time seismic signals. Landslides,” *Landslides*, vol. 9, no. 4, pp. 557–563, 2012.
- [45] R. Luongo, A. Perrone, S. Piscitelli, and V. Lapenna, “A prototype system for time-lapse electrical resistivity tomographies,” *International Journal of Geophysics*, vol. 2012, Article ID 176895, 12 pages, 2012.
- [46] K. Samyn, J. Travelletti, A. Bitri, G. Grandjean, and J. Malet, “Characterization of a landslide geometry using 3D seismic refraction traveltimes tomography: The La Valette landslide case history,” *Journal of Applied Geophysics*, vol. 86, pp. 120–132, 2012.
- [47] M. Yamada, Y. Matsushi, M. Chigira, and J. Mori, “Seismic recordings of landslides caused by Typhoon Talas (2011), Japan,” *Geophysical Research Letters*, vol. 39, no. 13, Article ID L13301, 2012.

- [48] T. Dahlin, H. Löfroth, D. Schälin, and P. Suer, "Mapping of quick clay using geoelectrical imaging and CPTU-resistivity," *Near Surface Geophysics*, vol. 11, no. 6, pp. 659–670, 2013.
- [49] V. Del Gaudio, J. Wasowski, and S. Muscillo, "New developments in ambient noise analysis to characterise the seismic response of landslide-prone slopes," *Natural Hazards and Earth System Sciences*, vol. 13, no. 8, pp. 2075–2087, 2013.
- [50] P. Lehmann, F. Gambazzi, B. Suski et al., "Evolution of soil wetting patterns preceding a hydrologically induced landslide inferred from electrical resistivity survey and point measurements of volumetric water content and pore water pressure," *Water Resources Research*, vol. 49, no. 12, pp. 7992–8004, 2013.
- [51] A. Malehmir, M. Bastani, C. M. Krawczyk et al., "Geophysical assessment and geotechnical investigation of quick-clay landslides – a Swedish case study," *Near Surface Geophysics*, vol. 11, no. 3, pp. 341–352, 2013.
- [52] A. Malehmir, M. U. Saleem, and M. Bastani, "High-resolution reflection seismic investigations of quick-clay and associated formations at a landslide scar in southwest Sweden," *Journal of Applied Geophysics*, vol. 92, pp. 84–102, 2013.
- [53] R. G. Sastry and S. K. Mondal, "Geophysical characterization of the Salna Sinking zone, Garhwal Himalaya, India," *Surveys in Geophysics*, vol. 34, no. 1, pp. 89–119, 2013.
- [54] S. Springman, A. Thielen, P. Kienzler, and S. Friedel, "A long-term field study for the investigation of rainfall-induced landslides," *Géotechnique*, vol. 63, no. 14, pp. 1177–1193, 2013.
- [55] A. Tonnellier, A. Helmstetter, J. Malet, J. Schmittbuhl, A. Corsini, and M. Joswig, "Seismic monitoring of soft-rock landslides: the super-sauze and valoria case studies," *Geophysical Journal International*, vol. 193, no. 3, pp. 1515–1536, 2013.
- [56] M. Yamada, H. Kumagai, Y. Matsushi, and T. Matsuzawa, "Dynamic landslide processes revealed by broadband seismic records," *Geophysical Research Letters*, vol. 40, no. 12, pp. 2998–3002, 2013.
- [57] P. Capizzi and R. Martorana, "Integration of constrained electrical and seismic tomographies to study the landslide affecting the cathedral of Agrigento," *Journal of Geophysics and Engineering*, vol. 11, no. 4, Article ID 045009, 2014.
- [58] V. Del Gaudio, S. Muscillo, and J. Wasowski, "What we can learn about slope response to earthquakes from ambient noise analysis: An overview," *Engineering Geology*, vol. 182, pp. 182–200, 2014.
- [59] C. Lissak, O. Maquaire, J. Malet et al., "Airborne and ground-based data sources for characterizing the morpho-structure of a coastal landslide," *Geomorphology*, vol. 217, pp. 140–151, 2014.
- [60] A. J. Merritt, J. E. Chambers, W. Murphy et al., "3D ground model development for an active landslide in Lias mudrocks using geophysical, remote sensing and geotechnical methods," *Landslides*, vol. 11, no. 4, pp. 537–550, 2014.
- [61] E. Stucchi, A. Ribolini, and A. Anfuso, "High-resolution reflection seismic survey at the Patigno landslide, Northern Apennines, Italy," *Near Surface Geophysics*, vol. 12, no. 4, pp. 559–571, 2013.
- [62] R. Supper, D. Ottowitz, B. Jochum et al., "Geoelectrical monitoring: an innovative method to supplement landslide surveillance and early warning," *Near Surface Geophysics*, vol. 12, no. 1, pp. 133–150, 2013.
- [63] R. Iverson, D. George, K. Allstadt et al., "Landslide mobility and hazards: implications of the 2014 Oso disaster," *Earth and Planetary Science Letters*, vol. 412, pp. 197–208, 2015.
- [64] M. Ogiso and K. Yomogida, "Estimation of locations and migration of debris flows on Izu-Oshima Island, Japan, on 16 October 2013 by the distribution of high frequency seismic amplitudes," *Journal of Volcanology and Geothermal Research*, vol. 298, pp. 15–26, 2015.
- [65] S. Uhlemann, P. B. Wilkinson, J. E. Chambers et al., "Interpolation of landslide movements to improve the accuracy of 4D geoelectrical monitoring," *Journal of Applied Geophysics*, vol. 121, pp. 93–105, 2015.
- [66] S. Yılmaz and C. Narman, "2-D electrical resistivity imaging for investigating an active landslide along a ridgeway in Burdur region, southern Turkey," *Arabian Journal of Geosciences*, vol. 8, no. 5, pp. 3343–3349, 2015.
- [67] M. Fressard, O. Maquaire, Y. Thiery, R. Davidson, and C. Lissak, "Multi-method characterisation of an active landslide: Case study in the Pays d'Auge plateau (Normandy, France)," *Geomorphology*, vol. 270, pp. 22–39, 2016.
- [68] J. Gance, J. Malet, R. Supper, P. Sailhac, D. Ottowitz, and B. Jochum, "Permanent electrical resistivity measurements for monitoring water circulation in clayey landslides," *Journal of Applied Geophysics*, vol. 126, pp. 98–115, 2016.
- [69] Z. Hu and W. Shan, "Landslide investigations in the northwest section of the lesser Khingan range in China using combined HDR and GPR methods," *Bulletin of Engineering Geology and the Environment*, vol. 75, no. 2, pp. 591–603, 2016.
- [70] D. Kušnirák, I. Dostál, R. Putiška, and A. Mojzeš, "Complex geophysical investigation of the Kapušany landslide (Eastern Slovakia)," *Contributions to Geophysics and Geodesy*, vol. 46, no. 2, pp. 111–124, 2016.
- [71] C. Ling, Q. Xu, Q. Zhang, J. Ran, and H. Lv, "Application of electrical resistivity tomography for investigating the internal structure of a translational landslide and characterizing its groundwater circulation (Kualiangzi landslide, Southwest China)," *Journal of Applied Geophysics*, vol. 131, pp. 154–162, 2016.
- [72] I. Solberg, M. Long, V. C. Baranwal, A. S. Gylland, and J. S. Rønning, "Geophysical and geotechnical studies of geology and sediment properties at a quick-clay landslide site at Esp, Trondheim, Norway," *Engineering Geology*, vol. 208, pp. 214–230, 2016.
- [73] S. Szalai, K. Szokoli, M. Metwaly, Z. Gribovszki, and E. Prácsér, "Prediction of the location of future rupture surfaces of a slowly moving loess landslide by electrical resistivity tomography," *Geophysical Prospecting*, vol. 65, no. 2, pp. 596–616, 2017.
- [74] S. Uhlemann, S. Hagedorn, B. Dashwood et al., "Landslide characterization using P- and S-wave seismic refraction tomography — The importance of elastic moduli," *Journal of Applied Geophysics*, vol. 134, pp. 64–76, 2016.
- [75] E. Yalcinkaya, H. Alp, and O. Ozel, "Near-surface geophysical methods for investigating the Buyukcekmece landslide in Istanbul, Turkey," *Journal of Applied Geophysics*, vol. 134, pp. 23–35, 2016.
- [76] F. Walter, A. Burtin, B. W. McArdell, N. Hovius, B. Weder, and J. M. Turowski, "Testing seismic amplitude source location for fast debris-flow detection at Illgraben, Switzerland," *Natural Hazards and Earth System Sciences*, vol. 17, no. 6, pp. 939–955, 2017.
- [77] H. Havenith, I. Torgoev, and A. Ischuk, "Integrated geophysical-geological 3D model of the right-bank slope downstream from the rogun dam construction site, Tajikistan," *International Journal of Geophysics*, vol. 2018, Article ID 1641789, 16 pages, 2018.

- [78] A. Flores Orozco, M. Bucker, M. Steiner, and J. Malet, "Complex-conductivity imaging for the understanding of landslide architecture," *Engineering Geology*, vol. 243, pp. 241–252, 2018.
- [79] G. Pappalardo, S. Imposa, M. S. Barbano, S. Grassi, and S. Mineo, "Study of landslides at the archaeological site of Abakainon necropolis (NE Sicily) by geomorphological and geophysical investigations," *Landslides*, vol. 15, no. 7, pp. 1279–1297, 2018.
- [80] S. Rezaei, I. Shoooshpasha, and H. Rezaei, "Reconstruction of landslide model from ERT, geotechnical, and field data, Nargeschal landslide, Iran," *Bulletin of Engineering Geology and the Environment*, vol. 78, no. 5, pp. 3223–3237, 2019.
- [81] A. Schimmel, J. Hübl, B. McARDell, and F. Walter, "Automatic Identification of Alpine Mass Movements by a Combination of Seismic and Infrasound Sensors," *Sensors*, vol. 18, no. 5, p. 1658, 2018.
- [82] K. Szokoli, L. Szarka, M. Metwaly, J. Kalmár, E. Prácsér, and S. Szalai, "Characterisation of a landslide by its fracture system using electric resistivity tomography and pressure probe methods," *Acta Geodaetica et Geophysica*, vol. 53, no. 1, pp. 15–30, 2018.
- [83] N. Vouillamoz, S. Rothmund, and M. Joswig, "Characterizing the complexity of microseismic signals at slow-moving clay-rich debris slides: the Super-Sauze (southeastern France) and Pechgraben (Upper Austria) case studies," *Earth Surface Dynamics*, vol. 6, no. 2, pp. 525–550, 2018.
- [84] B. Besson, G. Eiríksson, Ó. Thorarinnsson, A. Thórarinnsson, and S. Einarsson, "Automatic detection of avalanches and debris flows by seismic methods," *Journal of Glaciology*, vol. 53, no. 182, pp. 461–472, 2007.
- [85] J. Deparis, S. Garambois, and D. Hantz, "On the potential of ground penetrating radar to help rock fall hazard assessment: a case study of a limestone slab, Gorges de la Bourne (French Alps)," *Engineering Geology*, vol. 94, no. 1–2, pp. 89–102, 2007.
- [86] T. Spillmann, H. Maurer, A. G. Green, B. Heincke, H. Willenberg, and S. Husen, "Microseismic investigation of an unstable mountain slope in the Swiss Alps," *Journal of Geophysical Research: Atmospheres*, vol. 112, no. B7, Article ID B07301, 2007.
- [87] J. Deparis, B. Fricot, D. Jongmans, T. Villemin, L. Effendiantz, and A. Mathy, "Combined use of geophysical methods and remote techniques for characterizing the fracture network of a potentially unstable cliff site (the 'Roche du Midi', Vercors massif, France)," *Journal of Geophysics and Engineering*, vol. 5, no. 2, pp. 147–157, 2008.
- [88] J. Deparis, D. Jongmans, F. Cotton, L. Baillet, F. Thouvenot, and D. Hantz, "Analysis of rock-fall and rock-fall avalanche seismograms in the French alps," *Bulletin of the Seismological Society of America*, vol. 98, no. 4, pp. 1781–1796, 2008.
- [89] S. C. Moran, R. S. Matoza, M. A. Garcés et al., "Seismic and acoustic recordings of an unusually large rockfall at Mount St. Helens, Washington," *Geophysical Research Letters*, vol. 35, no. 19, Article ID L19302, 2008.
- [90] R. Supper, A. Römer, B. Jochum, G. Bieber, and W. Jaritz, "A complex geo-scientific strategy for landslide hazard mitigation – from airborne mapping to ground monitoring," *Advances in Geosciences*, vol. 14, pp. 195–200, 2008.
- [91] I. Vilajosana, E. Suriñach, A. Abellán, G. Khazaradze, D. Garcia, and J. Llosa, "Rockfall induced seismic signals: case study in Montserrat, Catalonia," *Natural Hazards and Earth System Sciences*, vol. 8, no. 4, pp. 805–812, 2008.
- [92] H. Willenberg, S. Loew, E. Eberhardt et al., "Internal structure and deformation of an unstable crystalline rock mass above Randa (Switzerland): Part I — Internal structure from integrated geological and geophysical investigations," *Engineering Geology*, vol. 101, no. 1–2, pp. 1–14, 2008.
- [93] D. Arosio, L. Longoni, M. Papini, M. Scaioni, L. Zanzi, and M. Alba, "Towards rockfall forecasting through observing deformations and listening to microseismic emissions," *Natural Hazards and Earth System Sciences*, vol. 9, no. 4, pp. 1119–1131, 2009.
- [94] G. Senfaute, A. Duperret, and J. A. Lawrence, "Micro-seismic precursory cracks prior to rock-fall on coastal chalk cliffs: a case study at Mesnil-Val, Normandie, NW France," *Natural Hazards and Earth System Sciences*, vol. 9, no. 5, pp. 1625–1641, 2009.
- [95] D. Amitrano, M. Arattano, M. Chiarle et al., "Microseismic activity analysis for the study of the rupture mechanisms in unstable rock masses," *Natural Hazards and Earth System Sciences*, vol. 10, no. 4, pp. 831–841, 2010.
- [96] J. Burjánec, G. Gassner-Stamm, V. Poggi, J. R. Moore, and D. Fäh, "Ambient vibration analysis of an unstable mountain slope," *Geophysical Journal International*, vol. 180, no. 2, pp. 820–828, 2010.
- [97] S. Gaffet, Y. Guglielmi, F. Cappa, C. Pambrun, T. Monfret, and D. Amitrano, "Use of the simultaneous seismic, GPS and meteorological monitoring for the characterization of a large unstable mountain slope in the southern French Alps," *Geophysical Journal International*, vol. 182, no. 3, pp. 1395–1410, 2010.
- [98] J. Got, P. Mourot, and J. Grangeon, "Pre-failure behaviour of an unstable limestone cliff from displacement and seismic data," *Natural Hazards and Earth System Sciences*, vol. 10, no. 4, pp. 819–829, 2010.
- [99] A. Helmstetter and S. Garambois, "Seismic monitoring of Séchilienne rockslide (French Alps): Analysis of seismic signals and their correlation with rainfalls," *Journal of Geophysical Research: Atmospheres*, vol. 115, no. F3, Article ID F03016, 2010.
- [100] C. Lévy, L. Baillet, D. Jongmans, P. Mourot, and D. Hantz, "Dynamic response of the Chamousset rock column (Western Alps, France)," *Journal of Geophysical Research: Atmospheres*, vol. 115, no. F4, Article ID F04043, 2010.
- [101] D. Schneider, P. Bartelt, J. Caplan-Auerbach, M. Christen, C. Huggel, and B. W. McARDell, "Insights into rock-ice avalanche dynamics by combined analysis of seismic recordings and a numerical avalanche model," *Journal of Geophysical Research: Atmospheres*, vol. 115, no. F4, Article ID F04026, 2010.
- [102] J. Travelletti, J. Demand, M. Jaboyedoff, and F. Marillier, "Mass movement characterization using a reflexion and refraction seismic survey with the sloping local base level concept," *Geomorphology*, vol. 116, no. 1–2, pp. 1–10, 2010.
- [103] F. Dammeier, J. R. Moore, F. Haslinger, and S. Loew, "Characterization of alpine rockslides using statistical analysis of seismic signals," *Journal of Geophysical Research: Atmospheres*, vol. 116, no. F4, Article ID F04024, 2011.
- [104] C. Hibert, A. Mangeney, G. Grandjean, and N. M. Shapiro, "Slope instabilities in Dolomieu crater, Réunion Island: From seismic signals to rockfall characteristics," *Journal of Geophysical Research: Atmospheres*, vol. 116, no. F4, Article ID F04032, 2011.
- [105] P. Lacroix and A. Helmstetter, "Location of seismic signals associated with microearthquakes and rockfalls on the sechilienne Landslide, French Alps," *Bulletin of the Seismological Society of America*, vol. 101, no. 1, pp. 341–353, 2011.

- [106] C. Levy, D. Jongmans, and L. Baillet, "Analysis of seismic signals recorded on a prone-to-fall rock column (Vercors massif, French Alps)," *Geophysical Journal International*, vol. 186, no. 1, pp. 296–310, 2011.
- [107] J. R. Moore, V. Gischig, J. Burjánek, S. Loew, and D. Fäh, "Site effects in unstable rock slopes: dynamic behavior of the randa instability (Switzerland)," *Bulletin of the Seismological Society of America*, vol. 101, no. 6, pp. 3110–3116, 2011.
- [108] T. Pánek, K. Šilhán, P. Tábořík et al., "Catastrophic slope failure and its origins: Case of the May 2010 Gírová Mountain long-runout rockslide (Czech Republic)," *Geomorphology*, vol. 130, no. 3–4, pp. 352–364, 2011.
- [109] T. Pánek, P. Tábořík, J. Klimeš, V. Komárková, J. Hradecký, and M. Štátný, "Deep-seated gravitational slope deformations in the highest parts of the Czech Flysch Carpathians: Evolutionary model based on kinematic analysis, electrical imaging and trenching," *Geomorphology*, vol. 129, no. 1–2, pp. 92–112, 2011.
- [110] D. Amtrano, S. Gruber, and L. Girard, "Evidence of frost-cracking inferred from acoustic emissions in a high-alpine rock-wall," *Earth and Planetary Science Letters*, vol. 341–344, pp. 86–93, 2012.
- [111] J. Burjánek, J. R. Moore, F. X. Yugsi Molina, and D. Fäh, "Instrumental evidence of normal mode rock slope vibration," *Geophysical Journal International*, vol. 188, no. 2, pp. 559–569, 2012.
- [112] C. Occhiena, V. Coviello, M. Arattano et al., "Analysis of microseismic signals and temperature recordings for rock slope stability investigations in high mountain areas," *Natural Hazards and Earth System Sciences*, vol. 12, no. 7, pp. 2283–2298, 2012.
- [113] F. Panzera, S. D'Amico, A. Lotteri, P. Galea, and G. Lombardo, "Seismic site response of unstable steep slope using noise measurements: the case study of Xemxija Bay area, Malta," *Natural Hazards and Earth System Sciences*, vol. 12, no. 11, pp. 3421–3431, 2012.
- [114] M. Walter, C. Arnhardt, and M. Joswig, "Seismic monitoring of rockfalls, slide quakes, and fissure development at the Super-Sauze mudslide, French Alps," *Engineering Geology*, vol. 128, pp. 12–22, 2012.
- [115] M. Walter, U. Schwaderer, and M. Joswig, "Seismic monitoring of precursory fracture signals from a destructive rockfall in the Vorarlberg Alps, Austria," *Natural Hazards and Earth System Sciences*, vol. 12, no. 11, pp. 3545–3555, 2012.
- [116] K. Allstadt, "Extracting source characteristics and dynamics of the August 2010 Mount Meager landslide from broadband seismograms," *Journal of Geophysical Research: Earth Surface*, vol. 118, no. 3, pp. 1472–1490, 2013.
- [117] P. Bottelin, D. Jongmans, L. Baillet et al., "Spectral analysis of prone-to-fall rock compartments using ambient vibrations," *Journal of Environmental & Engineering Geophysics*, vol. 18, no. 4, pp. 205–217, 2013.
- [118] A. Burtin, N. Hovius, D. T. Milodowski et al., "Continuous catchment-scale monitoring of geomorphic processes with a 2-D seismological array," *Journal of Geophysical Research: Earth Surface*, vol. 118, no. 3, pp. 1956–1974, 2013.
- [119] R. P. Singh, C. S. Dubey, S. K. Singh et al., "A new slope mass rating in mountainous terrain, Jammu and Kashmir Himalayas: application of geophysical technique in slope stability studies," *Landslides*, vol. 10, no. 3, pp. 255–265, 2013.
- [120] P. Bottelin, D. Jongmans, D. Daudon et al., "Seismic and mechanical studies of the artificially triggered rockfall at Mount Néron (French Alps, December 2011)," *Natural Hazards and Earth System Sciences*, vol. 14, no. 12, pp. 3175–3193, 2014.
- [121] C. Hibert, A. Mangeney, G. Grandjean et al., "Automated identification, location, and volume estimation of rockfalls at Piton de la Fournaise volcano," *Journal of Geophysical Research: Earth Surface*, vol. 119, no. 5, pp. 1082–1105, 2014.
- [122] T. Pánek, F. Hartvich, V. Jankovská et al., "Large Late Pleistocene landslides from the marginal slope of the Flysch Carpathians," *Landslides*, vol. 11, no. 6, pp. 981–992, 2014.
- [123] A. E. Akpan, A. O. Ilori, and N. U. Essien, "Geophysical investigation of Obot Ekpo Landslide site, Cross River State, Nigeria," *Journal of African Earth Sciences*, vol. 109, pp. 154–167, 2015.
- [124] A. Viero, A. Galgaro, G. Morelli, A. Breda, and R. G. Francese, "Investigations on the structural setting of a landslide-prone slope by means of three-dimensional electrical resistivity tomography," *Natural Hazards*, vol. 78, no. 2, pp. 1369–1385, 2015.
- [125] C. Colombero, C. Comina, G. Umili, and S. Vinciguerra, "Multiscale geophysical characterization of an unstable rock mass," *Tectonophysics*, vol. 675, pp. 275–289, 2016.
- [126] F. Dammeier, J. R. Moore, C. Hammer, F. Haslinger, and S. Loew, "Automatic detection of alpine rockslides in continuous seismic data using hidden Markov models," *Journal of Geophysical Research: Earth Surface*, vol. 121, no. 2, pp. 351–371, 2016.
- [127] A. Manconi, M. Picozzi, V. Coviello, F. De Santis, and L. Elia, "Real-time detection, location, and characterization of rockslides using broadband regional seismic networks," *Geophysical Research Letters*, vol. 43, no. 13, pp. 6960–6967, 2016.
- [128] M. Dietze, S. Mohadjer, J. M. Turowski, T. A. Ehlers, and N. Hovius, "Seismic monitoring of small alpine rockfalls – validity, precision and limitation," *Earth Surface Dynamics*, vol. 5, no. 4, pp. 653–668, 2017.
- [129] T. Gracchi, A. Lotti, G. Saccorotti et al., "A method for locating rockfall impacts using signals recorded by a microseismic network," *Geoenvironmental Disasters*, vol. 4, no. 1, article no 26, 2017.
- [130] S. Imposa, S. Grassi, F. Fazio, G. Rannisi, and P. Cino, "Geophysical survey to study a landslide body (north-eastern Sicily)," *Natural Hazards*, vol. 86, pp. 327–343, 2017.
- [131] F. Provost, C. Hibert, and J. Malet, "Automatic classification of endogenous landslide seismicity using the random forest supervised classifier," *Geophysical Research Letters*, vol. 44, no. 1, pp. 113–120, 2017.
- [132] P. Tábořík, J. Lenart, V. Blecha, J. Vilhelm, and O. Turský, "Geophysical anatomy of counter-slope scarps in sedimentary flysch rocks (Outer Western Carpathians)," *Geomorphology*, vol. 276, pp. 59–70, 2017.
- [133] D. Arosio, L. Longoni, M. Papini, M. Boccolari, and L. Zanzi, "Analysis of microseismic signals collected on an unstable rock face in the Italian Prealps," *Geophysical Journal International*, vol. 213, no. 1, pp. 475–488, 2018.
- [134] J. Burjánek, V. Gischig, J. R. Moore, and D. Fäh, "Ambient vibration characterization and monitoring of a rock slope close to collapse," *Geophysical Journal International*, vol. 212, no. 1, pp. 297–310, 2018.
- [135] A. Lotti, V. Pazzi, G. Saccorotti, A. Fiaschi, L. Matassoni, and G. Gigli, "HVSr analysis of rockslide seismic signals to assess the subsoil conditions and the site seismic response," *International Journal of Geophysics*, vol. 2018, Article ID 9383189, 11 pages, 2018.

- [136] M. Del Soldato, V. Pazzi, S. Segoni, P. De Vita, V. Tofani, and S. Moretti, "Spatial modelling of pyroclastic cover deposit thickness (depth to bedrock) in peri-volcanic areas of Campania (southern Italy)," *Earth Surface Processes and Landforms*, vol. 43, no. 9, pp. 1757–1767, 2018.
- [137] L. V. Socco, D. Jongmans, D. Boiero et al., "Geophysical investigation of the Sandalp rock avalanche deposits," *Journal of Applied Geophysics*, vol. 70, no. 4, pp. 277–291, 2010.
- [138] A. Lotti, G. Saccorotti, A. Fiaschi et al., "Seismic monitoring of rockslide: the Torgiovannetto quarry (Central Apennines, Italy)," in *Engineering Geology for Society and Territory*, G. Lollino, Ed., vol. 2, pp. 1537–1540, Springer International Publishing, Switzerland, 2014.
- [139] G. Cassiani, A. Godio, S. Stocco et al., "Monitoring the hydrologic behaviour of a mountain slope via time-lapse electrical resistivity tomography," *Near Surface Geophysics*, vol. 7, no. 5-6, pp. 475–486, 2009.
- [140] F. Fischanger, G. Morelli, G. Ranieri, G. Santarato, and M. Occhi, "4D cross-borehole electrical resistivity tomography to control resin injection for ground stabilization: a case history in Venice (Italy)," *Near Surface Geophysics*, vol. 11, no. 1, pp. 41–50, 2013.
- [141] V. Pazzi, M. Ceccatelli, T. Gracchi, E. B. Masi, and R. Fanti, "Assessing subsoil void hazards along a road system using H/V measurements, ERTs, and IPTs to support local decision makers," *Near Surface Geophysics*, vol. 16, no. 3, pp. 282–297, 2018.
- [142] V. Pazzi, M. Di Filippo, M. Di Nezza et al., "Integrated geophysical survey in a sinkhole-prone area: Microgravity, electrical resistivity tomographies, and seismic noise measurements to delimit its extension," *Engineering Geology*, vol. 243, pp. 282–293, 2018.
- [143] W. Wai-Lok Lai, X. Dérobert, and P. Annan, "A review of Ground Penetrating Radar application in civil engineering: A 30-year journey from Locating and Testing to Imaging and Diagnosis," *NTD and E International*, vol. 96, pp. 58–78, 2018.

Research Article

3D Mafic Topography of the Transition Zone between the North-Western Boundary of the Congo Craton and the Kribi-Campo Sedimentary Basin from Gravity Inversion

Séverin Nguiya,¹ Willy Lemotio ,² Philippe Njandjock Nouck,² Marcelin M. Pemi,^{2,3} Alain-Pierre K. Tokam,² and Evariste Ngatchou²

¹Faculty of Industrial Engineering, University of Douala, P.O. Box 2701, Cameroon

²Faculty of Science, University of Yaoundé 1, P.O. Box 812, Yaoundé, Cameroon

³Department of Renewable Energy, Higher Technical Teachers' Training College (HTTTC), University of Buea, P.O. Box 249, Cameroon

Correspondence should be addressed to Willy Lemotio; willylemotio@gmail.com

Received 25 October 2018; Revised 4 April 2019; Accepted 6 May 2019; Published 2 June 2019

Guest Editor: Stefano Morelli

Copyright © 2019 Séverin Nguiya et al. This is an open access article distributed under the Creative Commons Attribution License, which permits unrestricted use, distribution, and reproduction in any medium, provided the original work is properly cited.

The structure of the transition zone between the north-western boundary of the Congo Craton and the Kribi-Campo sedimentary basin is still a matter of scientific debate. In this study, the existing gravity data are interpreted in order to better understand the geodynamics of the area. Qualitatively, results show that the major gravity highs are associated with long-wavelength shallow sources of the coastal sedimentary basin, while large negative anomalies trending E-W correlate to low dense intrusive bodies found along the northern limit of the Congo Craton. For the delineation of the causative sources, the gravity anomalies have been inverted based on the Parker-Oldenburg iterative process. As inputs, we used a reference depth of 20 km obtained by spectral analysis and successively, the density contrasts 0.19 g/cm^3 and 0.24 g/cm^3 , deduced from available 1D shear wave velocity models. The results reveal an irregular topography of the mafic interface characterized by a sequence of horst and graben structures with mafic depths varying between 15.6 km and 23.4 km. The shallower depths (15.6–17 km) are associated with the uprising of the mafic interface towards the upper crust. This intrusion may have been initiated during the extension of the Archean Ntem crust resulting in a thinning of the continental crust beneath the coastal sedimentary basin. The subsidence of the mafic interface beneath the craton is materialized by 2 similar graben structures located beneath both Matomb and Ebolowa at a maximum depth of 23.4 km. The intermediate depths (18–22 km) are correlated to the suture zone along the Pouma-Bipindi area. The location of some landslides across the area matches within the northern margin of the Congo Craton and suggests that this margin may also impact on their occurrence. This work provides new insights into the geodynamics, regional tectonics, and basin geometry.

1. Introduction

South Cameroon region is known to be an interesting area of mining research and oil exploration. All mining experts agree that the area is a hidden treasure in terms of the substantial mining resources it possesses. The use of spectral methods to investigate the crustal density structure in the south region of Cameroon remains among many mathematical tools the most employed approach in geophysical data analysis and the interpretation of tectonic structure. One such application is the spectral estimation of the depth to the bottom of the gravity sources due to the variation of crustal layers beneath

the north-western margin of the Congo Craton [1–3]. The depth estimation of density interfaces from potential fields beneath the Congo Craton was done by means of the gravity power spectra [4], which showed that the slopes of logarithms of energy spectra are linked to the thickness of the anomalous gravity sources.

In order to explain the geodynamic process of density layers from the uppermost mantle to the lower crust, the fluctuation of the power spectrum function permitted [1–3] and Owona et al. [5] to delineate the frequency limits corresponding to the major crustal discontinuities; the mean depth results obtained for those authors reveal a crustal

thickness around 45 km beneath the Congo Craton area and about 28 km thick for the continental part of the Kribi-Campo area. Despite a good correlation with the estimation of the crustal thickness within the transition zone between the Congo Craton and the Kribi-Campo subbasin derived from seismological studies [6], there is no consensus with the presence of the mafic composition for the lower crust [1, 3, 5]. Therefore, works of Tokam et al. [6], based on the joint inversion of the Rayleigh wave group velocities and P-receiver functions, reveal the presence of mafic formations that occupy almost the entire lower crust, with thicknesses varying from 10 km under the continental basin to nearly 25 km beneath the Craton. Moreover, results obtained by Owona et al. [5], by joining other geophysical data analyses, have pointed the similar conclusion.

This paper aims to provide a map showing the spatial distribution of the intracrustal mafic discontinuity in the transitional zone between the north-western edge of the Congo Craton (CC) and the Kribi-Campo area. In order to improve the knowledge of the mafic structure beneath the region, a 2D spectral analysis of existing gravity data is carried out. This spectral method is applied in a rectangular grid size of 157 km \times 201 km expanded using the maximum entropy prediction which is useful in minimizing edge effects when working with data containing systematic high frequency [7–10]. Then, a code for 3D inversion of gravity data [11] has been used to obtain the 3D topographical image caused by the mafic interface density considering the density contrast between two media. The main purpose of this paper is to show the geodynamic implication of the intracrustal mafic discontinuity in the north-western portion of the Congo Craton based on the analysis and the gravity inversion constrained by seismic information and its implication to the occurrence of landslides across the area. Factors as faults, earthquake, volcanism, and geomorphology are known as potential triggers of landslides. By correlating the location of some observed landslides and the gravity data, new insights on the regional tectonic can be inferred.

2. Geological and Tectonic Settings

The study area lies between latitudes 2.32° and 4.20°N and longitudes 9.85° and 11.3°E (Figure 1); three major tectonic features characterize the region (Figure 2): the Kribi-Campo subbasin, located in the Gulf of Guinea, is the littlest coastal basin in Cameroon and constitutes the southern part of the Douala/Kribi-Campo basin [12], the north-western portion of the Congo Craton (CC), known in Cameroon as the Ntem Complex, is mostly composed of Archean rocks including intrusive rocks with a predominance of magmatic rocks, and metasediments and mafic-ultramafic intrusive rocks and the Pan-African Belt of Central Africa (CAPB), situated between the West African and Congo Craton, represent the Yaoundé group in our study area [13–17].

The region of interest bears traces of the different tectonic events that have marked the African continent. The more prominent tectonic feature is the north-western part of the Congo Craton which is known in Cameroon as the Ntem Complex. This complex is divided into two main

structural units: the Nyong unit, to the northwest end, and the Ntem unit, in the south-central region [18, 19]. The Archean Ntem unit is dominated by gneisses intrusive complexes primarily consisting of Tonalite Trondhjemites and Granodiorites (TTG) suite rocks [20–22]. The intrusive rocks of the tectonic unit have a charnockitic character with predominance of granitic, tonalitic, and syenitic formations. The Archean terranes in the Ntem Complex are mostly formed of Horst and Graben tectonics linked to diapiric movements in the mid to lower crust [23]. The whole unit appears to have been coaxially strained [23]. Some authors reveal that the presence of dome and basin structures is the result of gravitational instabilities [24–27]. Thus, works from Owona et al. [5] confirmed this theory by proposing a 2D 1/2 gravity modelling showing that the interface separating the lower mafic crust and the upper crust is undulating. They supposed that the mafic layer also contributes to the variation of the gravity field along the gravity profile crossing the transition zone between the Congo Craton and the Kribi-Campo basin. The Ntem Complex is also marked by the past magmatic activities with several bodies of dense rocks such as amphibolites, gabbros, charnockites, and granodiorites [5, 6].

The last mafic event, dated at the period before 2.1 Ga, is marked by the rifting of the Archean Ntem crust [5, 28, 29] and has resulted in the emplacement of swarms of mafic doleritic dykes [5, 28–31]. The continental crust of our study area is mainly composed of Nyong unit formations. According to some geologist, the Nyong unit may be relict features from the collision between the Congo Craton and the Sao Francisco (Brazil) Craton in the lower Proterozoic [21, 32]. The Nyong unit also carries imprints of past magmatic event, which are characterized by the neoproterozoic intrusion of nepheline syenites in the sinistral shear zone [29, 33]. Apart from the Douala basin, the Kribi-Campo subbasin is the only sedimentary coastal basin in the south region of Cameroon. It constitutes the northern limit of the Gabo-Equato Guinean basin [34]. The Archean basement is mostly composed of green rocks belt, charnockites, and potassic granitoids [35]. Ntamak-Nida et al. [12] mentioned that the western limit of the subbasin appears to be widely defined by a major oceanic fracture zone, the Kribi Fracture Zone (noted KFZ) [36, 37]; the continental sector of the KFZ, known as the Kribi-Campo fault (KCF), is the major fault that crosses the transition zone between the Congo Craton and the Kribi-Campo area. The interpretation of geophysical model shows that this resulting suture may be assimilated to the thrusting of the central Africa mobile belt rocks onto the Congo Craton (CC) [5].

3. Data and Method

3.1. Data Acquisition. The data were collected during gravity campaign operated in Cameroon between 1963 and 1990 by various organizations and researchers [5]. The earliest data were those carried out by ORSTOM (Office de la Recherche Scientifique et Technique d'Outre-Mer); to these data have been added those acquired by [39], Société E.L.F. (Essences et Lubrifiants Français), IRGM (Institut de la Recherche Géologique et Minière) and University of Leeds (1984–1985 and 1986). Gravimeters Worden (N° 313, 600, 69, and 135) and

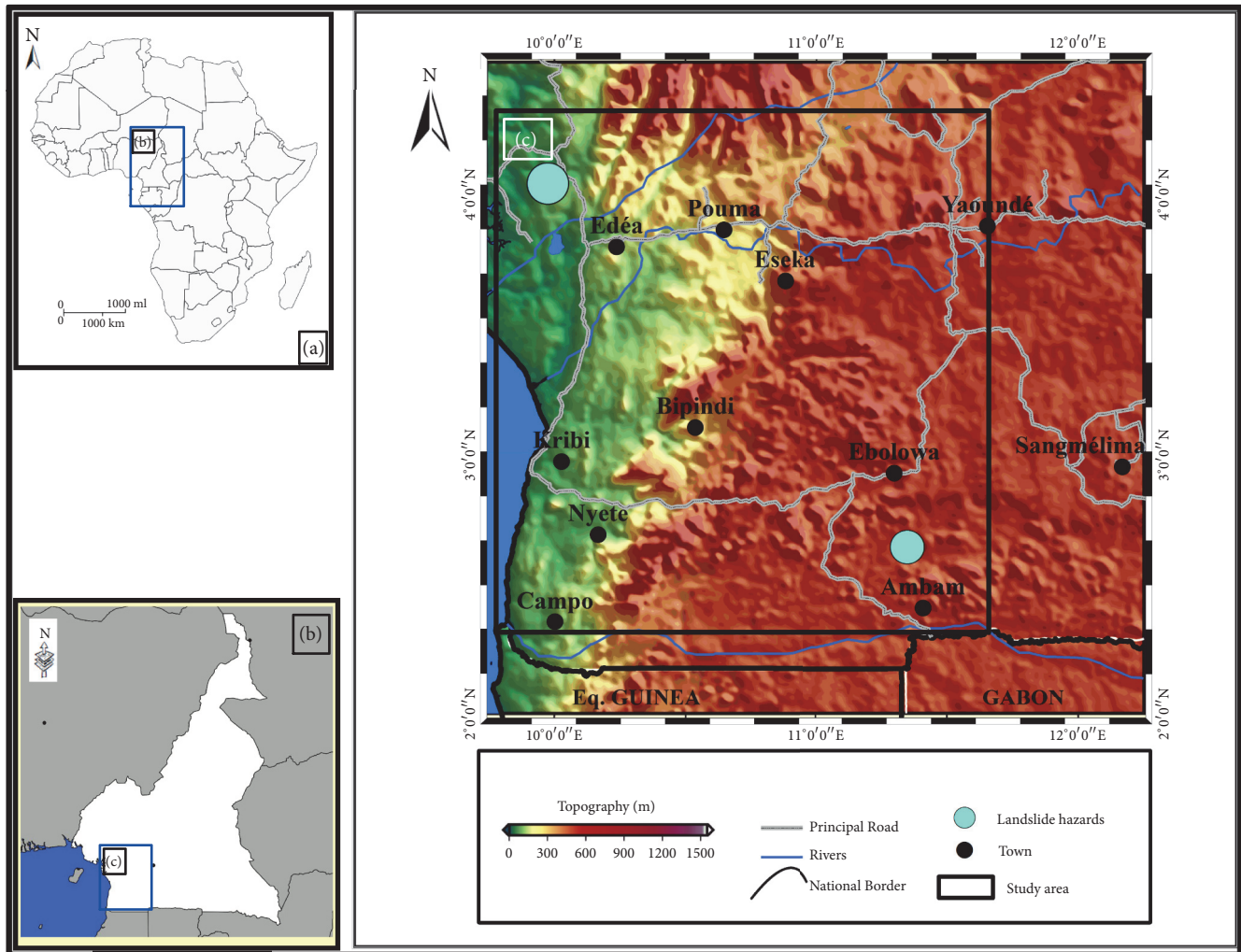


FIGURE 1: Topographic map showing the study area (landslide document is taken from Tchindjang, [38]).

Lacoste & Romberg (model G, No 471 and 828) were used for the gravity measurement with a resolution of 0.01 mGal.

The gravity measurements were done along roads and trails and the space between stations varied from 4 to 5 Km including base stations. The coordinates of gravity stations have maximum error ranging between 200 and 2000 m and the measurement accuracy of gravity values was about 0.2 mGal. The data were uniformly reduced to Earth-tide effects and instrumental drift, free air reduction was also applied to the data, and a reduction density of $2,67 \text{ g/cm}^3$ was used for the Bouguer correction. The Hammer (1939) method [41] was used for the terrain corrections [42]. The available dataset used in this study derived from 256 gravity stations covering an area of about $157 \text{ km} \times 201 \text{ km}$ size. The study includes only terrestrial data because of the difficulties to access data from the sea. The Kriging method was used in order to achieve a meaningful spatial distribution of gravity data within the region. The kriging interpolation process was executed using Surfer 13 software. The Bouguer values were then plotted to obtain the Bouguer anomaly map, with a grid spacing of

2,02 km giving a total grid size of 100 rows by 79 columns (Figure 3).

3.2. Method. To better characterize the mafic structure along the transition zone between the Kribi-Campo and the Congo Craton, the methodology along the paper is based on the 2D spectral analysis followed by the regional/residual separation and the 3D inversion of the regional gravity map.

3.2.1. Power Spectrum Analysis. The Fast Fourier Transform method was commonly used in geophysical studies for the depth estimation of the causative bodies. The power spectrum graph was obtained by a careful choice of the gravity profiles crossing the significant anomalies on the Bouguer anomaly map computed [3, 5, 43]. Herein, the 2D spectral analysis was applied to the gravity grid data and allows calculation of an average depth to a set of causative anomaly sources [10, 44, 45]. The method proves to be an appropriate technic where the calculation of the power spectrum should not be

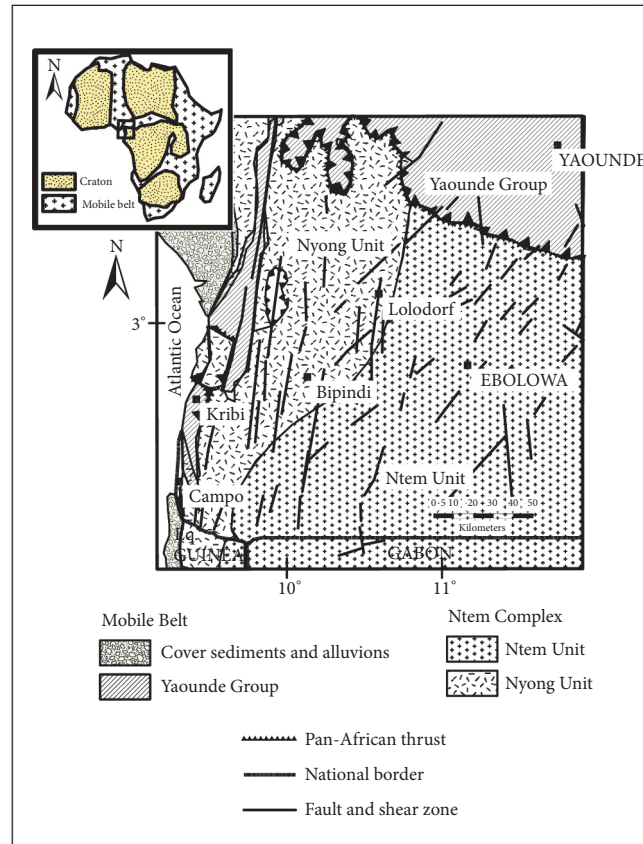


FIGURE 2: Simplified geological map of the South Cameroon showing the principal units and the main lithological formations (modified after Tchameni et al. [40]).

dominated by biases and it should be statistically meaningful [45–48].

The 2D power spectrum energy is obtained by averaging over the set of independent computed power spectra energy; then the current two-dimensional problem was transformed to one dimension, and we can compute the logarithm of the energy spectrum that provides the mean depth of density interfaces [45, 49, 50].

Prior to spectra calculation, data grids need to be expanded in order to avoid edge effects [7]. The maximum entropy method (MEM) is a powerful tool to minimize boarding effects. The MEM samples the original data near the grid edges to determine its spectral content. It then predicts a data function that would have the same spectral signature as the original data and computes the extrapolated data of the same nature and the real data adjacent to it. Furthermore, the predicted grid data will not significantly modify the energy spectrum that would result only from the original data. This process runs along lines in several directions and applied weighting along adjacent lines to eliminate line divergences.

Errors on the depth estimation of causatives sources increase with depth, but also depend on the size of the grid. Thus, for simple shape structures used for two-dimensional gravity models, Naidu [51] considers that the size of a grid

must be 10-20 times greater in extent than the mean depth of the anomaly source sought. In our case, the Bouguer anomaly map has been expanded to a square grid of $225 \text{ km} \times 225 \text{ km}$ by using the MEM (Figure 4). It is preferable to use a square grid to compute the radially averaged spectrum (this is to use the same frequency in both x- and y-directions, so the radial average spectrum is not biased by a frequency different from the other). For the determination of the mafic discontinuity, assuming a value of 16 to 20 km for its mean depth, our expanded grid has the required size for these estimates. The aim of spectral analysis is to determine the mean depth of the mafic discontinuity for the grid in order to study its spatial distribution in the crust. Once power spectrum is computed, the top depth of the density interface is estimated as half of the slope of the straight line adjusted to the natural log of energy spectrum versus the radial frequency by considering the theory of Spector and Grant [4].

3.2.2. Regional/Residual Separation. The observed gravity anomalies are the sum of gravity effects of density fluctuations at different depths in the basement half space. Before inverting the mafic density interface, the target anomalies should first be separated from the Bouguer anomaly map. In the literature, there are several filtering methods

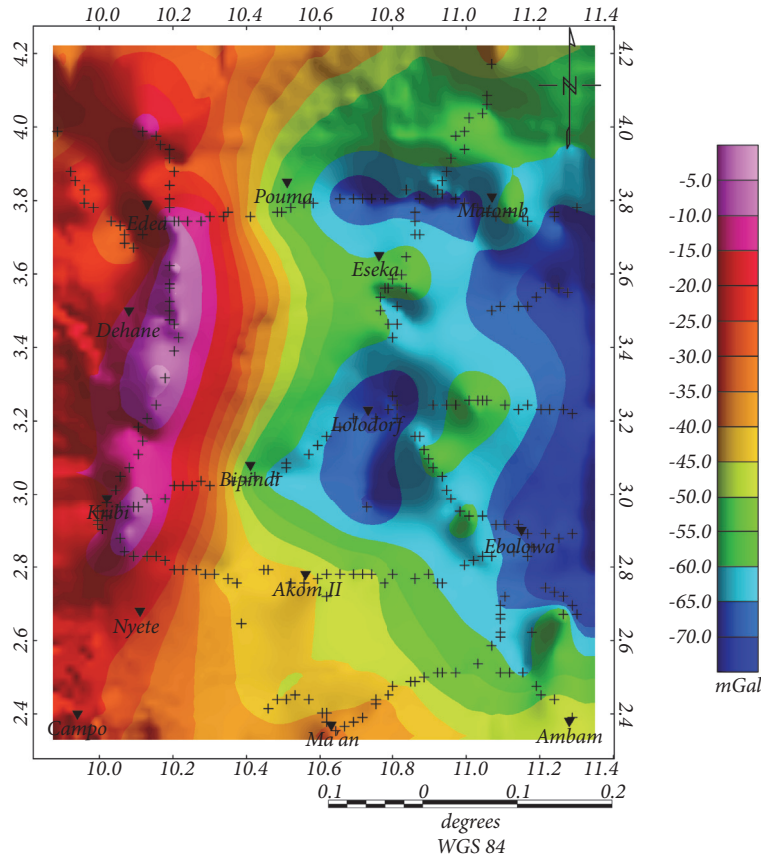


FIGURE 3: Gravity data distribution and Bouguer gravity anomaly map of the study area (Contour interval: 5 mGals; color-scale unit: mGal; projection: Mercator). Data are recorded at stations shown here as black cross and were collected following all available roads and tracks.

where regional/residual separation was performed [4, 52–54]. Herein, an Upward Continuation filtering method was used. It is the suitable method to dissociate the regional gravity anomaly resulting from deep sources from the observed gravity. The regional/residual separation by using the Upward Continuation method consists of selecting a height at which the continuation is most closely linked to the known regional anomaly at a standard observation. The spectral analysis permits us to get the average depth estimate at which the mafic discontinuity was located; the obtained depth will be taken as the optimum continuation height for the regional-residual separation [55, 56]. The upward continuation process by attenuating the shallow source anomalies allows a better accentuation of deeper anomaly sources with the increase of the upward continuation height [57].

3.2.3. 3D Gravity Inversion. At the aim of producing a full map showing the spatial distribution of the intracrustal mafic formation within the crust, a 3D gravity inversion will be performed on the regional gravity data. The method allows computing the geometry of a three-dimensional density interface from the gravity anomaly data. The inversion procedure is based on the Parker and Oldenburg iterative process [58, 59] and it can be established as follows:

$$F[h(x)] = -\frac{F[\Delta g(x)] e^{(-kz_0)}}{2\pi G\rho} - \sum_{n=2}^{\infty} \frac{k^{n-1}}{n!} F[h^n(x)] \quad (1)$$

where $F(\Delta g)$ is the Fourier transform of the gravity field, G is the gravitational constant, ρ is the density contrast between two layers, k is the wave number, $h(x)$ is the depth to the interface (considered positive downwards), and z_0 is the average depth of the density interface.

The relation (1) is the fundamental theory used by [11] that permits them to develop a 3DINVER MATLAB code for the computation of the depth interfaces related to the gridded gravity anomaly. By considering the mean depth interface, the density contrast between two media, and the input filtered gravity anomaly, the depth interface values are iteratively computed and the inversion procedure ends when the difference between two consecutive topography interfaces is less than a given error level used as convergence criterion or until a maximum of iterations is accomplished.

The instability of the inversion operation (1) due to high-frequency anomaly sources allowed Oldenburg [59] and Nagendra et al. [60] to introduce a high-cut filter $HCF(k)$ in order to achieve the convergence of series. Two other filter parameters WH and SH are used for the adjustment during the convergence process. The filter is defined by

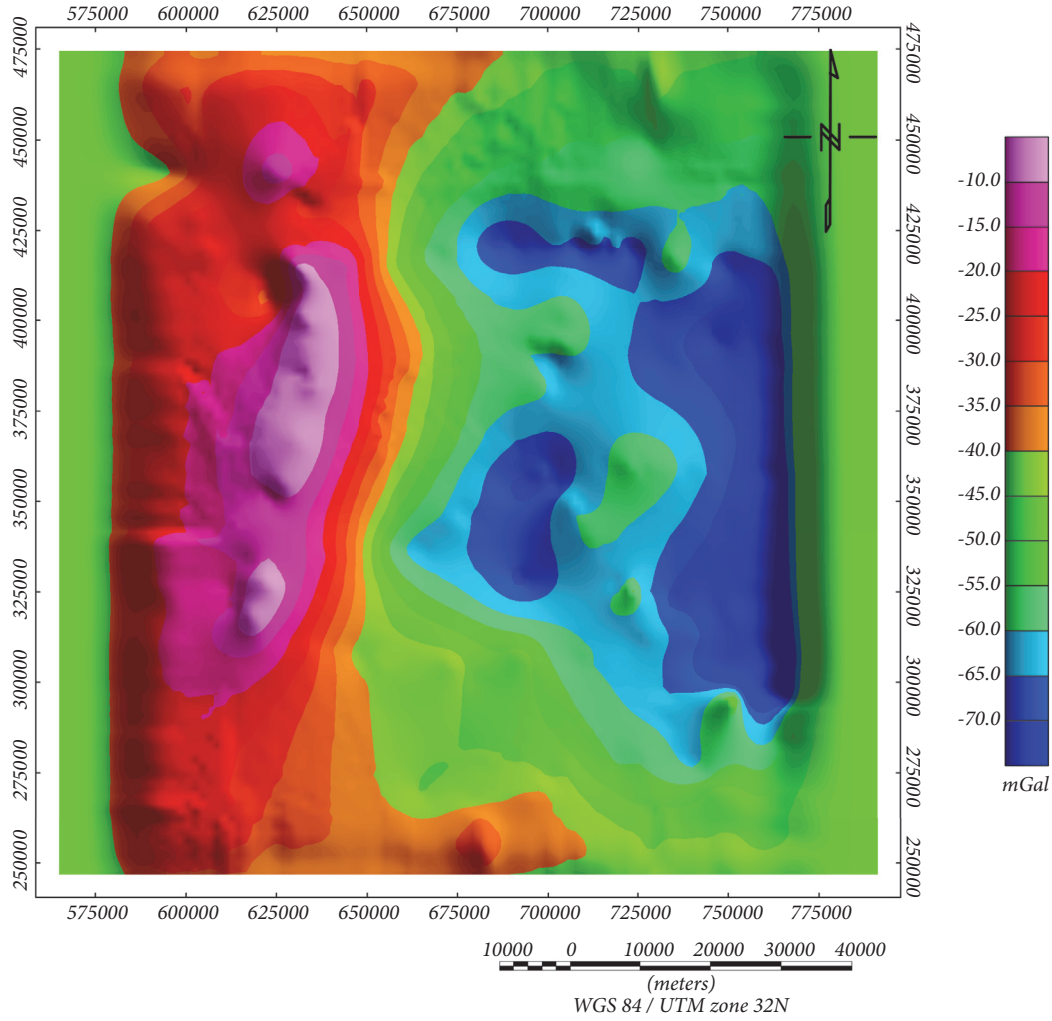


FIGURE 4: Grid map expanded using the Maximum Entropy Method (Burg, 1967) conserving the same spectral signature as the previous Bouguer anomaly map.

$$HCF(k) = \frac{1}{2} \left[1 + \cos \left(\frac{k - 2\pi WH}{2(SH - WH)} \right) \right] \quad (2)$$

For middle frequencies, there is a rectangular window with a value of 1 for low frequencies (WH) and 0 for high frequencies (SH) equivalent to a hamming window. k is the wavenumber expressed as $1/\lambda$, where λ is the wavelength in kilometers.

The MATLAB function 3DINVER performed by [11] was used in this paper to study the 3D geometry of the intracrustal mafic discontinuity in the area. So this study was carried out on a rectangular filtered gravity map with a size of 157 km \times 201 km, made up of 256 gravity stations irregularly spaced. Before initiating the inversion procedure, it is recommended to expand the grid because the Fast Fourier transform (FFT) function introduces some edge effects during filtering, then invert the data, and finally remove the grid extension in order to retain only the original grid size. So any edge effects are removed from the study area. Herein, the previous original grid map was extended to a square grid size of 225 km \times 225 km by applying the MEM [7]. Usually, a 10% expansion

of the grid is enough to avoid boarding effects. Two other parameters are important for the inversion process: the mean depth reference of the interface and the density contrast across the interface. The iteration is at which the inversion process is stopped and the RMS is also displayed by the function. After convergence has been obtained, the best way to determine if the inverted interface is an acceptable solution is to compare the observed filtered gravity anomaly with the computed gravity data associated with the inverted interface. If the differences between both gravity maps are only a few mGal, the model can be validated; if not, some parameters of the inversion should be changed. The data processing was conducted by following the procedure summarized on the chart (see Figure 8).

4. Results

4.1. Analysis of the Bouguer Anomaly Map. The Bouguer anomaly map (Figure 3) reflects the combined effects of

shallower and deeper crustal basement due to the lateral variations in the density of unknown subsurface materials. A global look of this map shows a couple of positive and negative anomalies delineated by strong NE-SW gradients. The appearance of these gradients could be associated with the fault network that occurs in the Precambrian oceanic area and extends to the continental domain crossing the Kribi Campo and the Congo Craton regions. This fault system, known as the Kribi-Campo Fault (KCF), resulted from the frontal collision between the two large structures, the Congo Craton (CC) and the Pan-African Mobile Belt (PMB) [61].

The Lolodorf zone and the Pouma-Matomb area are marked by long wavelength gravity anomalies with low amplitude of about -65 mGal. Both anomalies seem to be linked to the large gravity low observed in the eastern part of the Bouguer map with a minimum amplitude of -69 mGal and N-S trend. The gravity low seem to be caused by a downwarp in the basement and can be attributed to the crustal thickening due to the granitic intrusion with the low density contrast within the Northern portion of the Congo Craton [3]. This explanation corroborates well with the isostasy theory, in comparison with the topographic map (Figure 1), showing that elevated area is generally linked to the low anomaly sources constituting the crust. The Bouguer map shows a relative high (amounting to -10 mGal) around the Kribi-Edea region. The high values can be attributed to the intrusion of magmatic formations and their subsequent metamorphism (granulites body) or the uprising of some mantle materials (syenitic, mafic formations). Thus, geological studies indicate an important mafic magmatic activity during the rift extension [62]. The isoanomaly contours in the map going from the coastal area to the continental domain follow almost the NE-SW trend and reflect the onshore transition of the continental crust.

4.2. Mean Depth Estimation of Density Interfaces. The power spectrum graph of Figure 5 illustrates a sketch of the natural logarithm of the power spectrum versus the frequency. The graph is divided into three frequency domains. The first one, domain A, in the low frequency ranging from 0.02 to 0.22 km^{-1} , represents the deeper density interface with a mean depth of 20.01 ± 0.9 km. The second one, domain B, corresponds to the high frequency ranging from 0.25 to 0.75 km^{-1} and belongs to the shallower sources with a mean depth value of 5.7 ± 0.3 km. The final part of the power spectrum graph does not have a geological meaning and corresponds to the white noise. Depth estimates of 20.01 ± 0.9 km may possibly correspond to the intracrustal mafic interface beneath the transitional zone between the Kribi-Campo and the Congo craton area. This result is in good agreement with seismic studies from Tokam et al. [6] revealing that the crust is divided into several layers with a lower thick mafic layer at depth below 18 km beneath the region. The shallower sources' depths of 5.7 ± 0.3 km may be attributed to the dense mantle formations within the sedimentary coastal basin responsible for the observed positive gravity anomalies in the coastal area.

After identifying the main sources responsible for the observed gravity anomalies of the study area, the study will

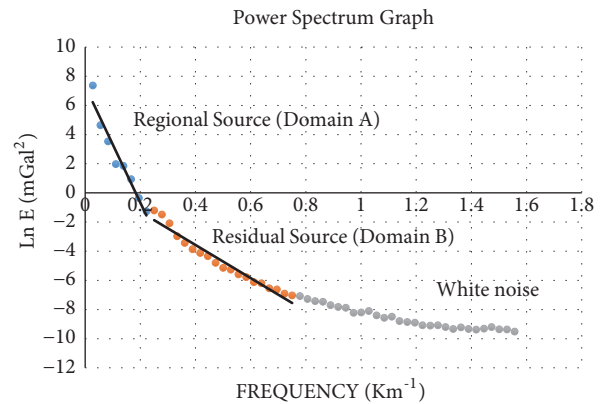


FIGURE 5: Power spectrum graph of the gridded Bouguer data showing 2 frequency domains. The first one with blue circles represents the regional source, the second domain with orange circles corresponds to residual source, and the gray circles represent white noise.

be now focused on the anomaly sources situated in the low frequencies associated with the deeper mafic formation. We will apply a filter to the Bouguer map to isolate the gravity signatures corresponding to the 20 km mean depth interface.

4.3. Regional and Residual Gravity Maps. The regional gravity map (Figure 6) shows anomalies ranging from -56 to -24 mGal; the anomalies consist of a western gravity high and an eastern gravity low almost oriented N-S and separated by strong gradients. The gravity highs are observed in the Kribi-Dehane area with a slight extension towards Campo and a maximum amplitude of -25 mGal. These anomalies are enclosed by gravimetric gradients which extend towards the Pouma-Bipindi area. The enhancement of these gradients on the central part of the regional map confirmed the presence of fault system in the area and also revealed that the major faults crossing the transitional zone between the Kribi-Campo and Congo Craton area had a deep origin and in the same way could explain the seismicity of the zone. The upward continued map also illustrates the change in anomaly character with a minimum value of -56 mGal along Ebolowa-Matomb axis. This can suggest that the lower crust formations are deepening towards the east of the region. As such, the 20 km upward continued data present a suitable regional map for gravity inversion studies to help define the basement characteristics of the mafic discontinuities and associated intrusive bodies from the Pan-African belt.

To highlight local anomalies, the regional component of the gravity anomaly field is commonly subtracted from the Bouguer anomaly map, generating a residual map (Figure 7) that shows exactly shallow density structures. The computed residual gravity map is characterized like the Bouguer anomaly map by a broad positive anomaly zone with a NE-SW orientation. This zone can be related to the shallow response of mafic rocks such as gabbros [5, 30]. Gravity lows with a ring shape observed at Pouma, Matomb, and Bipindi-Lolodorf area appear to be the signature of intrusive igneous

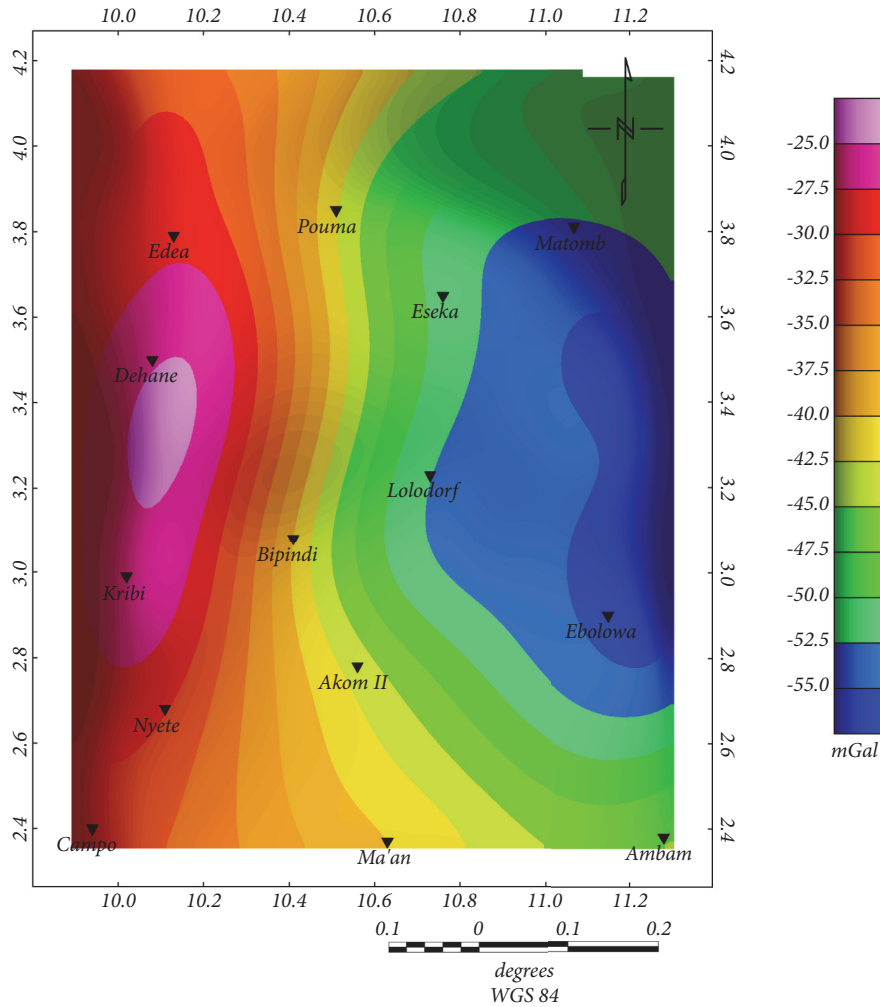


FIGURE 6: Regional gravity map obtained by applying the upward continuation filtering method to the Bouguer anomaly map (contour interval: 2.5 mGals; color-scale unit: mGal; and projection: Mercator).

rocks in the upper crust such as granites, syenites, and Tonalite Trondhjemites and Granodiorites (TTG) formations [30, 63].

4.4. 3D Topography of the Mafic Interfaces. Taking into account the importance of the inversion parameters such as the density contrast between the two media (the lower mafic crust and the upper crust) and the mean reference depth of the mafic interface, we considered a mean depth of 20 km derived from the results of the spectral analysis. We also made the choice to vary the density contrast depending on whether we are in coastal area or beneath the craton (Table 1).

For each density contrast, we compute the corresponding mafic depths in order to obtain the topography of the underlying mafic interfaces (Figure 9). The constraints from the shear wave velocity model [5, 6] helped to compute the density contrast beneath the Kribi-Campo area and within the Congo Craton. The convergence criterion was set at 0.02 km; the RMS errors between the two consecutive topography values and the iteration at which the inversion process is stopped are presented in Table 1. We denote that for both

geological terrains the iterative procedure was achieved at the third iteration and that the change in density contrast does not significantly alter the depth variation of the mafic interface; this allows us to deduce that we are practically under the same tectonic unit. Regarding the mafic depth map, when increasing the density contrast from 0.19 to 0.24 g/cm³, the magnitude of the upper crust thickness increases around 0.95 km within the coastal area, while it decreases about 1.68 km beneath the Congo Craton. The MATLAB function also displays the gravity anomaly associated with the inverted mafic interfaces and the residual error between the observed gravity anomalies and the computed anomalies (Figure 10).

This later appears to be very close to the input gravity signal with a residual error map revealing that the differences are minor and are in the range of -2.5 to 1.8 mGal. So we can rely on the estimate of the resulting inverted mafic interface.

The resulting mafic depth map represents the depth variations of the boundary between the upper crust and the lower mafic body. The upper crust thickness seems to increase

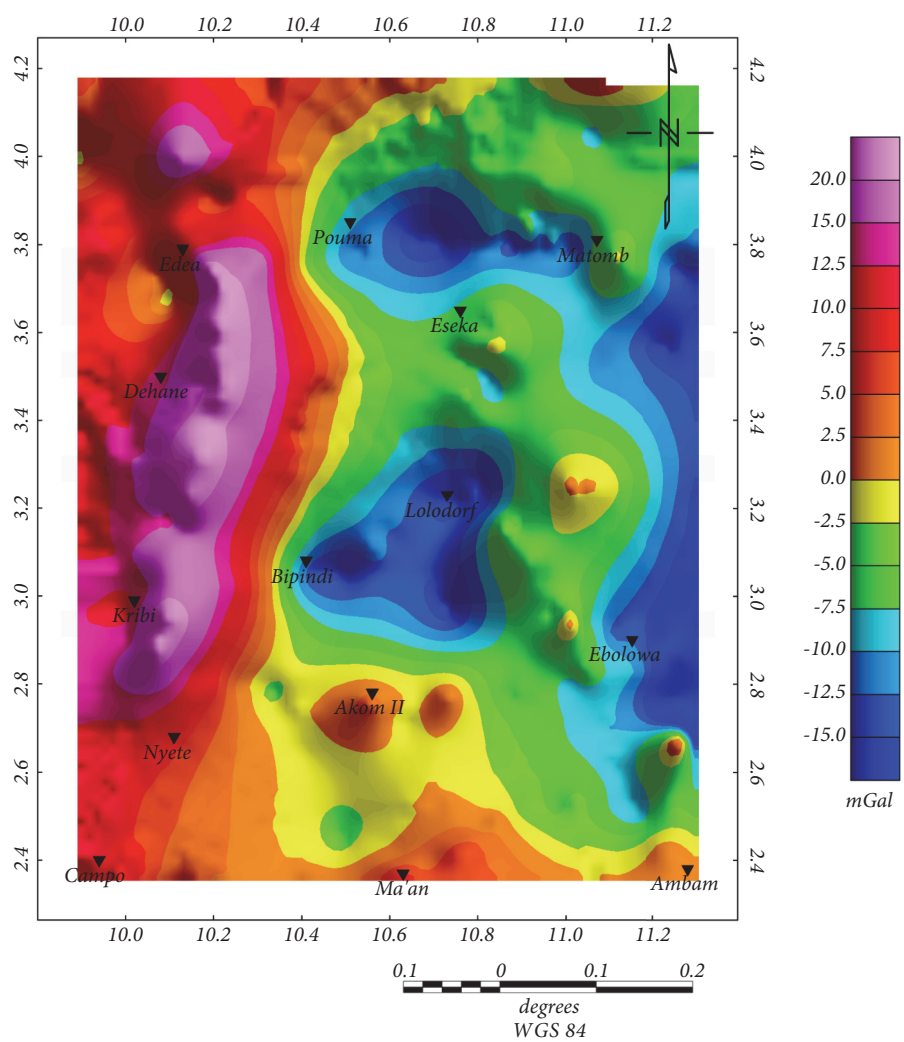


FIGURE 7: Residual gravity map of the study area obtained by subtracting the regional gravity map from the Bouguer anomaly map (contour interval: 2.5 mGals; color-scale unit: mGal; and projection: Mercator).

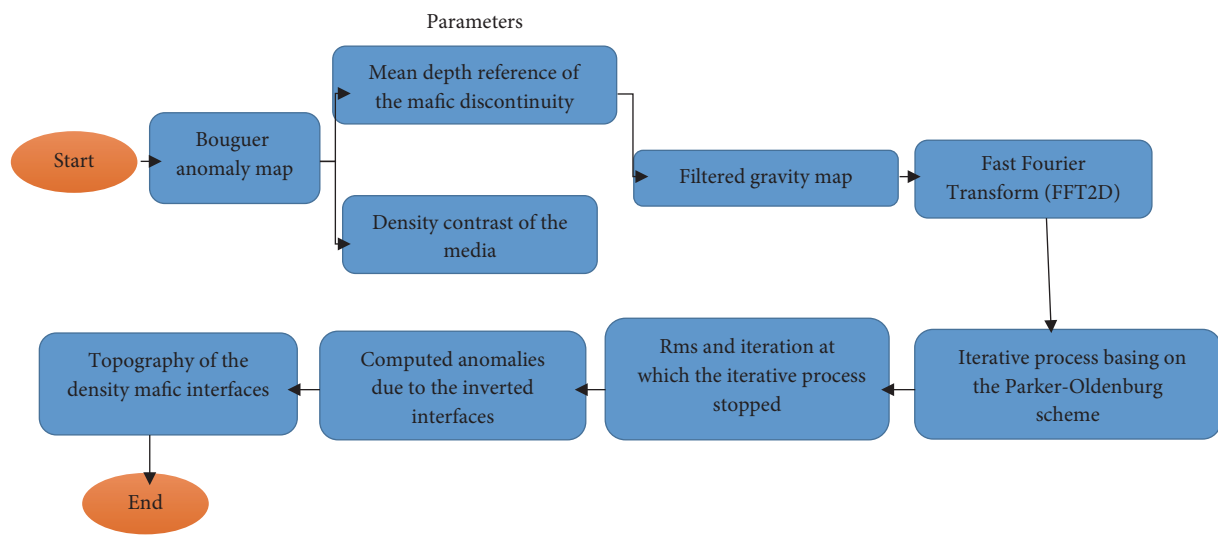


FIGURE 8: Summary of the 3D inversion process.

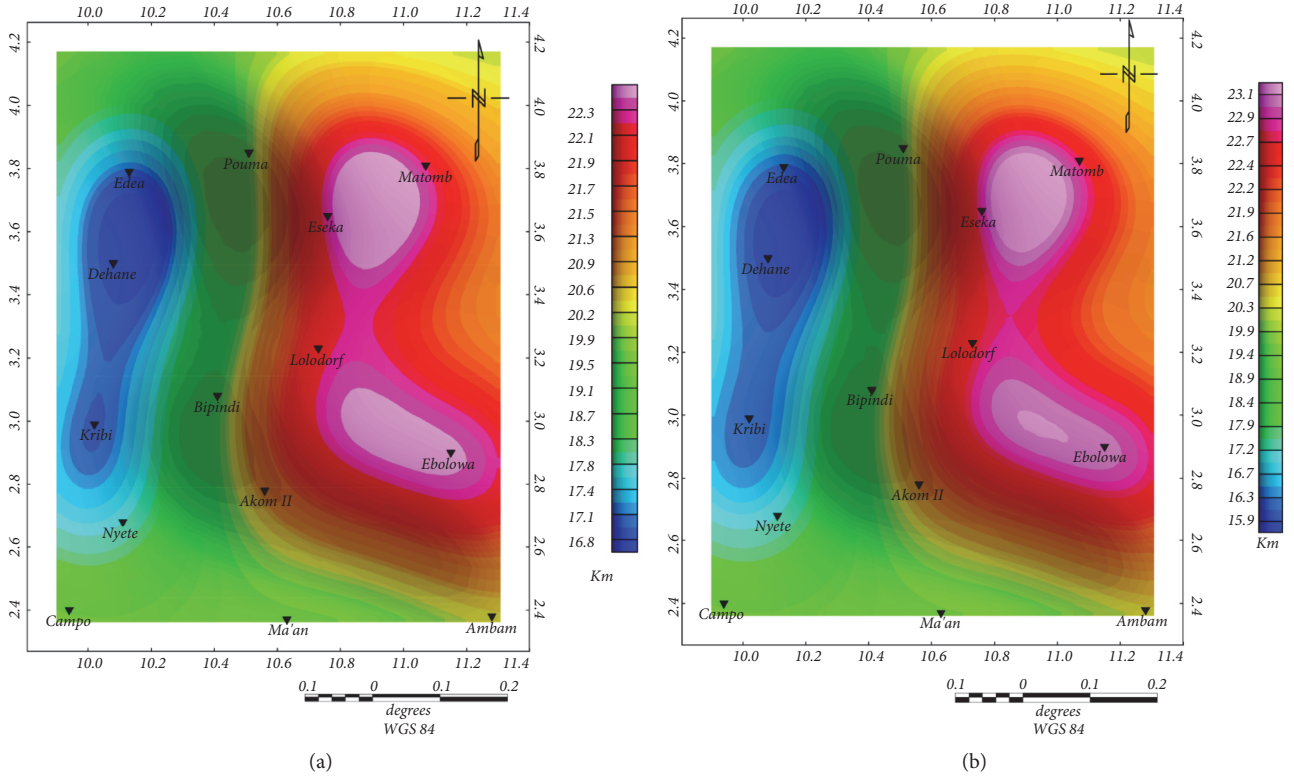


FIGURE 9: (a) Computed contour map of the mafic depth by using the 3D gravity inversion of the study area. Density contrast $\Delta\rho = 0.24 \text{ g/cm}^3$. (b) Computed contour map of the mafic depth by using the 3D gravity inversion of the study area. Density contrast $\Delta\rho = 0.19 \text{ g/cm}^3$, contour interval 0.1 mGal. Geographical coordinates.

TABLE 1: Inversion efficacy by geological unit.

Mean depth reference: Z_0	Density contrast	
$Z_0 = 20 \text{ Km}$	Kribi-Campo terrain	Congo Craton terrain
	$\Delta\rho = 0.19 \text{ g/cm}^3$	$\Delta\rho = 0.24 \text{ g/cm}^3$
	ITER=3	ITER=3
	RMS=0.0031 Km	RMS=0.0015 Km

eastwards from approximately 16 km (coastal sedimentary basin) to about 22 km (continental craton), with dominated N-S strong gradients that cover the Pouma-Bipindi area. The lower mafic depths are observed in the western part of the area precisely in the Kribi-Edea axis. This area is marked by dome structures with a minimum depth of about 15 and 16 km observed both in Dehane and Kribi regions. Despite the poor data coverage beneath the coastal sedimentary basin, the mafic depth distribution is in agreement with previous studies [5, 6]. The authors revealed a depth of 18 km for the mafic formations beneath the basin, while in this study, we find a depth varying from 15.6 to 17 km. The dome structures observed in some coastal regions show that the mafic discontinuity is uprising toward the upper crust (see Figure 11). The mafic interface becomes deeper from the center region to the eastern edge of the study area where a depth of up to 23 km is reached at Ebolowa and in the vicinity of Matomb. These collapse zones seem to describe two grabens structure of the same nature. Although the

two depressions seem to be a bit similar in their shape, magnitude, and strike direction, it is difficult to link the two tectonic features because they could have been put in place at different geologic period. Furthermore, geological studies reveal that the Ebolowa sector is dominated by low Archean terrain with occurrence of low syenitic intrusion [24, 40, 64]. This Archean period of deformation can explain the presence of the large basin structure in the Ebolowa area and its gravitational incidence in our gravity model. At a first glance, the intermediate depth going from 18 to 22 km in the central part of the inverted interface map defines contours patterns identical to those of gravity anomaly derived from the computed data.

The linear characteristics, crossing the Pouma-Bipindi area, follow almost the N-S trend direction and correspond to the faults network which correlate well with the geological map. These faults features may be responsible of the subsidence of the lower mafic interface beneath the Matomb-Ebolowa area.

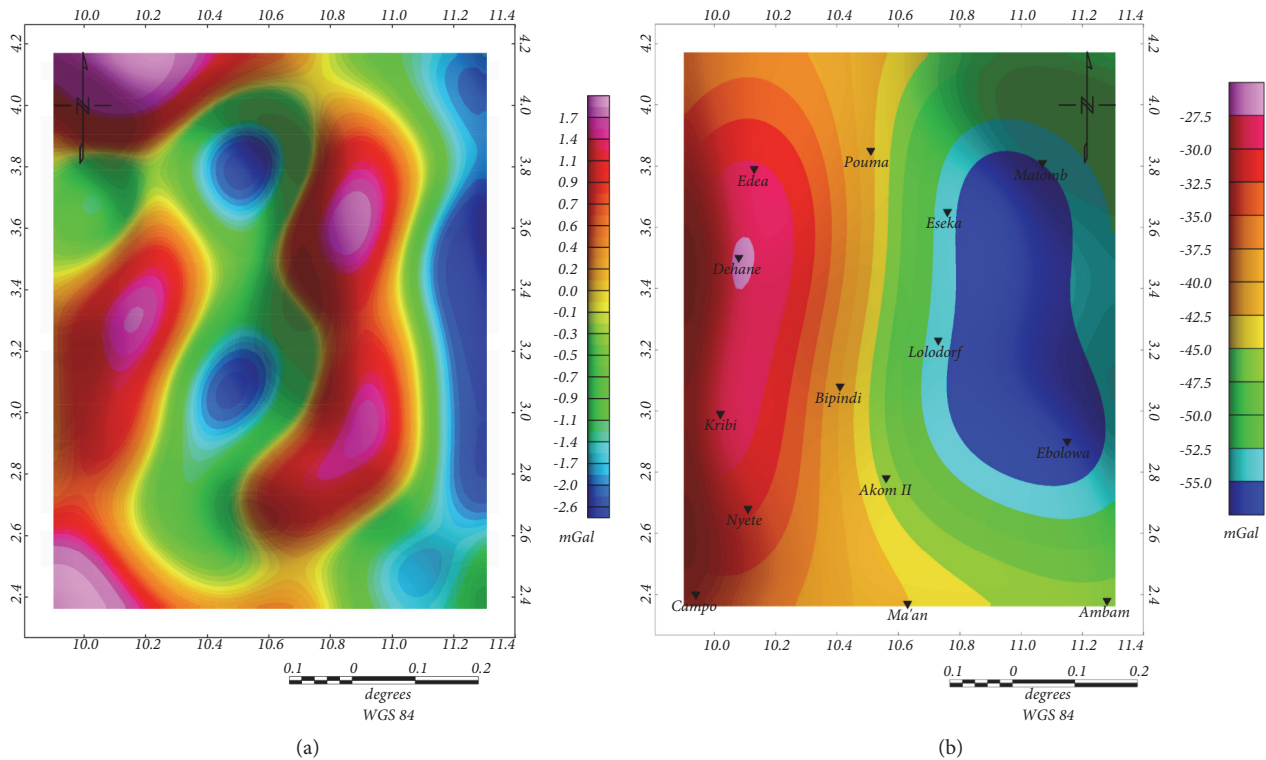


FIGURE 10: (a) Difference between the regional gravity map and the one due to the inverted mafic interface. Contour interval 0.1 mGal. Geographical coordinates. (b) Gravity anomaly map associated with the inverted mafic interfaces. Contour interval 2.5 mGal. Geographical coordinates.

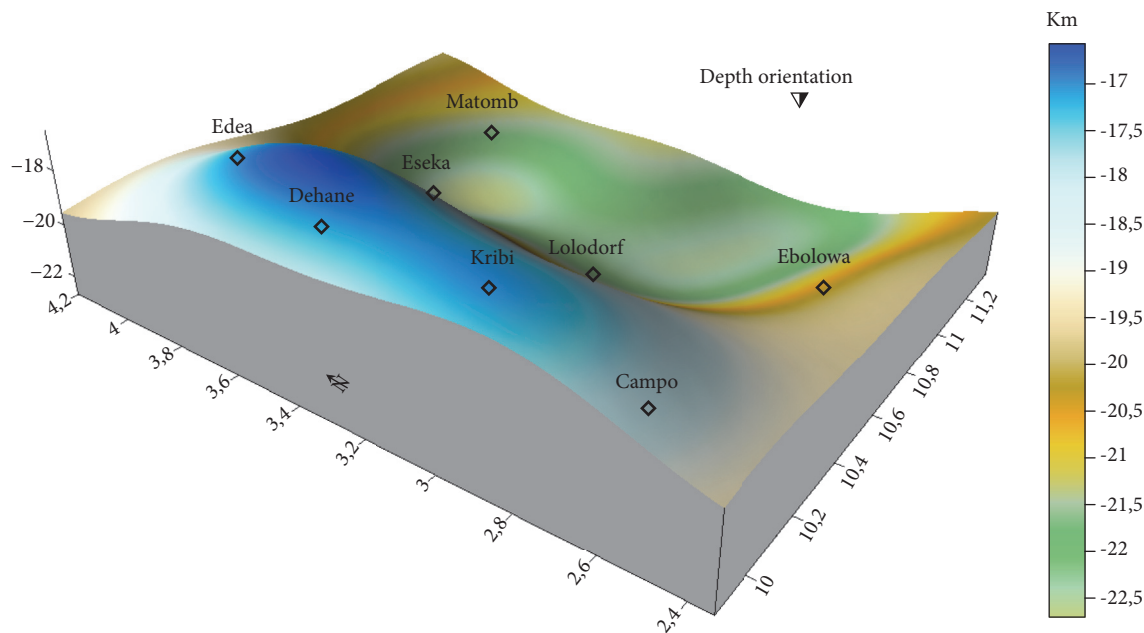


FIGURE 11: 3D view of the mafic depth showing the topography of the mafic density interfaces along the transition zone between the Kribi-Campo area and the Congo Craton.

5. Discussion

The investigation of the intracrustal mafic discontinuity beneath the transition zone between the Congo Craton and the Kribi-Campo area by using gravity data analysis and 3D gravity inversion method has allowed a better understanding of the mafic interfaces behavior within the continental crust. The results prove that the lower/upper crust boundary is not homogeneous and present discrepancies due to lateral density variation in Earth interior. To achieve this, a rectangular grid size of 157 km \times 201 km was selected to perform the two-dimensional (2D) spectral analysis. Prior to this transformation, the gridded data was expanded to a square grid size of 225 km \times 225 km to avoid side effects and to obtain more reliable source depth estimations. Poudjom et al. [1] used the same process to build the crustal thickness contour map of the West central Africa; they have selected 33 subgrids to estimate the crustal thickness (T_c) and studied its variation beneath the area by spectral analysis of the gravity data. The power spectrum graph allows us to identify two density domains: one situated in the high frequencies and a mean depth value of 5.7 km, another located on the low frequencies and an average depth of 20.01 km. The first estimate corresponds to dense formations within the Kribi-Campo subbasin. Tadjou et al. [65], by investigating the anomalous density structure beneath the Kribi-Campo sedimentary subbasin, have estimated the dense bodies in the same area at 6.5 km depth; so just a minor difference of 0.8 km was obtained; this can be explained by the permanent tectonic activity affecting the basin and the gravity effect of the other dense materials within the upper-crust layer. In order to elucidate ambiguities on the dense bodies origin and to bring out more explanation about the gravitational instabilities observed along the above transition zone, the 20 km mean depth interface attributed to the intracrustal mafic discontinuities was chosen as a fundamental parameter for the 3D gravity inversion. The inversion procedure constrained by seismic information was applied on the filtered gravity data with the aim to construct a mafic depth map. The mafic interface is uplifted in the Kribi-Edea area with the crust thinning beneath the continental basin where the Moho is found at about 28 km [5, 6, 65].

This result suggests that the observed dense materials have a mantle origin during the past magmatic event as Tadjou et al. [65] mentioned in their gravity studies, but our model reveals shallow mafic intrusion beneath the Kribi-Campo area which could be the consequence of the relamination process during the Archean subduction [66–68]. The mafic intrusion also influences the deformation of the sedimentary rocks and exhibits some control on the basin geometry. The mafic depth becomes deeper from the center map to the east with a slight extension in the Matomb-Ebolowa area. The computed topography contour map also reveals clearly a linear characteristic of N-S trend along the Pouma-Bipindi axis which approximately corresponds to the faults feature. Geological studies reveal that this area is characterized by a faulting deformation responsible for development of blastomylonitic shear zones [29, 30]. The resulting deformation may be interpreted from the model

as the thrusting of mafic interfaces onto the east side of the Lolodorf region. The symmetric graben structure observed both in Ebolowa and in the vicinity of Matomb resulted from the subsidence of the mafic intrabasement with a major depth of 23.4 km, so 3.4 km below the reference depth. The fact that the south-central part of the Congo Craton is dominated by low-density Archean rocks could explain the presence of these graben tectonic structures. Our results also provide new insights concerning the geodynamic behavior of the top of the lower mafic crust along the transition zone. It appears to be shallower in the Kribi-Campo area and deeper beneath the Congo Craton. The same process was observed for the Moho discontinuity where seismic work of Tokam et al. [6] demonstrates that the Moho is shallower beneath the coastal basin and becomes deeper within the Congo Craton. In addition, the results of our gravity inversion correlate well with those obtained by Owona et al. [5], but we noticed some discrepancies. Indeed, our model integrates a thin upper/middle-crust layer in the Kribi-Campo domain where the lower limit is located at almost 15 km and a thicker upper/middle-crust layer \sim 23 km beneath the CC. Otherwise, since our study was based on the processing of the long wavelength gravity signal; the undulation of the mafic interface going from the coastal plain to the Archean continental crust plays a crucial role on the gravity instability on the surface geology and its geodynamic process has been better highlighted in this study.

The high gravity gradient observed on the Bouguer map associated with the Kribi-Campo fault (KCF) is part of the lineaments known as Sanaga fault. Ngatchou et al. [69] analyzed broadband seismogram and determined the source mechanism of the March 19, 2005 Monatele earthquake. Their results show the evidence that the contact between the Congo Craton and the Pan-African Mobile Belt (PMB) is still seismically active. Moreover, Owona et al. [70, 71] also pointed out the existence of some other fault systems in the area that may be also active. The location of some historical landslides across the area [38] matches with the location of some major tectonic features within the area and suggests that this major tectonic element may control the occurrence of landslides in the study area.

6. Conclusion

By using a 3D gravity inversion program based on the Parker-Oldenburg method and developed by [11], we carry out a gravity data analysis, using seismic information as constraints [6], to build a Mafic depth map showing the spatial distribution of the mafic density interfaces beneath the transition zone between the Kribi-Campo and the Congo Craton. The inversion of the mafic structure generated by a standard density model was based on the approximating assumption that the density contrast between the layers above and below the interface takes a constant value. The study allows us to deduce that the gravity lows and highs of circular or semicircular nature observed on the theoretical gravity map were attributed to mafic intrusions in terms of basement uplifts and depressions, proving that the mafic interfaces have a great incidence on the gravity anomalies within the

region. From a mean reference depth of 20 km, the 3D view of the mafic depth shows uplifts reaching over 15.6-17 km in both Kribi and Dehane regions and two symmetrical mafic depressions, while centre parts extend up to a depth of 23.4 km beneath both Ebolowa and Matomb areas. The flock of depth contours almost trending N-S direction has increased values towards the east in the vicinity of Lolodorf. It suggests the existence of fault systems controlling the subsidence of mafic interfaces beneath the craton subsurface and impacting the occurrence of landslides in the area. Thus, the gravity inversion by using the Parker-Oldenburg 3D inversion method proves to be a powerful tool for the gravity data analysis and the tectonic interpretation.

Data Availability

The data used to support the findings of this study are available from the corresponding author upon request.

Conflicts of Interest

The authors reveal that there are no conflicts of interest regarding the publication of this paper.

Acknowledgments

The authors are indebted to IRD (Institut de Recherche pour le Développement) for providing them with the data used in this work. Most of the figures in the paper were produced using Geosoft software developed by Ian Macleod and Tim Dobush for Exploration Geophysics. We also thank the anonymous referees for their helpful suggestions and comments.

References

- [1] Y. H. Djomani, J. M. Nnange, M. Diamant, C. J. Ebinger, and J. D. Fairhead, "Effective elastic thickness and crustal thickness variations in west central Africa inferred from gravity data," *Journal of Geophysical Research: Atmospheres*, vol. 100, no. 11, pp. 22047–22070, 1995.
- [2] J. M. Nnange, V. Ngako, J. D. Fairhead, and C. J. Ebinger, "Depths to density discontinuities beneath the Adamawa Plateau region, Central Africa, from spectral analyses of new and existing gravity data," *Journal of African Earth Sciences*, vol. 30, no. 4, pp. 887–901, 2000.
- [3] J. M. Tadjou, R. Nouayou, J. Kamguia et al., "Gravity analysis of the boundary between the Congo craton and the pan-african belt of Cameroon," *Austrian Journal of Earth Sciences*, vol. 102, 2009.
- [4] A. Spector and F. S. Grant, "Statistical models for interpreting aeromagnetic data," *Geophysics*, vol. 35, no. 2, pp. 293–302, 1970.
- [5] M. L. C. Owona Angue, S. Nguia, R. Nouayou, A. P. Tokam Kamga, and E. Manguelle-Dicoum, "Geophysical investigation of the transition zone between the Congo Craton and the Kribi-Campo sedimentary basin (Southwestern Cameroon)," *South African Journal of Geology*, vol. 114, no. 1, pp. 145–158, 2011.
- [6] A.-P. K. Tokam, C. T. Tabod, A. A. Nyblade, J. Julià, D. A. Wiens, and M. E. Pasyanos, "Structure of the crust beneath Cameroon, West Africa, from the joint inversion of Rayleigh wave group velocities and receiver functions," *Geophysical Journal International*, vol. 183, no. 2, pp. 1061–1076, 2010.
- [7] J. P. Burg, "Maximum entropy spectral analysis," in *Proceedings of the 37th Annual International Meeting, Soc. of Explor. Geophys.*, vol. 31, Oklahoma City, Okla, USA, 1967.
- [8] J. P. Burg, "A new analysis technique for time series data," NATO Advanced Study Institute on Signal Processing, Enschede, Netherlands, 1968.
- [9] R. McDonough, "Maximum-entropy spatial processing of array data," *Geophysics*, vol. 39, no. 6, pp. 843–851, 1974.
- [10] A. R. Bansal, V. P. Dimri, and G. V. Sagar, "Depth estimation from gravity data using the maximum entropy method (MEM) and the multi taper method (MTM)," *Pure and Applied Geophysics*, vol. 163, no. 7, pp. 1417–1434, 2006.
- [11] D. Gómez-Ortiz and B. N. P. Agarwal, "3DINVER.M: a MATLAB program to invert the gravity anomaly over a 3D horizontal density interface by Parker-Oldenburg's algorithm," *Computers & Geosciences*, vol. 31, no. 4, pp. 513–520, 2005.
- [12] M. J. Ntamak-Nida, S. Bourquin, J.-C. Makong et al., "Sedimentology and sequence stratigraphy from outcrops of the Kribi-Campo sub-basin: Lower Mundek Formation (Lower Cretaceous, southern Cameroon)," *Journal of African Earth Sciences*, vol. 58, no. 1, pp. 1–18, 2010.
- [13] B. F. Windley and D. Bridgwater, "The evolution of Archaean low-and high grade terrains," *Geological Society of Australia Special Publication*, vol. 3, pp. 33–46, 1971.
- [14] S. B. Shirey and G. N. Hanson, "Mantle heterogeneity and crustal recycling in Archean granite-greenstone belts: Evidence from Nd isotopes and trace elements in the Rainy Lake area, Superior Province, Ontario, Canada," *Geochimica et Cosmochimica Acta*, vol. 50, no. 12, pp. 2631–2651, 1986.
- [15] B. Luais and C. J. Hawkesworth, "The generation of continental crust: An integrated study of crust-forming processes in the archaean of Zimbabwe," *Journal of Petrology*, vol. 35, no. 1, pp. 43–94, 1994.
- [16] S. B. Lobach-Zhuchenko, V. P. Chekulaev, N. A. Arestova, A. B. Vrevsky, and A. V. Kovalenko, "Genesis of the earliest (3.20–2.83 Ga) terranes of the Fennoscandian shield," *Russian Journal of Earth Sciences*, vol. 5, no. 2, pp. 75–91, 2003.
- [17] R. S. Sharma and M. K. Pandit, "Evolution of early continental crust," *Current Science*, vol. 84, no. 8, pp. 995–1001, 2003.
- [18] C. A. Basseka, Y. Shandini, and J. M. Tadjou, "Subsurface structural mapping using gravity data of the northern edge of the Congo Craton, South Cameroon," *Geofizika*, vol. 28, no. 2, pp. 229–245, 2011.
- [19] J. Ndema Mbongue, T. Ngnotue, C. Ngo Nlend, J. Nzenti, and E. Cheo Suh, "Origin and evolution of the formation of the Cameroon Nyong Series in the western border of the Congo Craton," *Journal of Geosciences and Geomatics*, vol. 2, pp. 62–75, 2014.
- [20] A. Nedelec, E. N. Nsifa, and H. Martin, "Major and trace element geochemistry of the Archaean Ntem plutonic complex (south Cameroon): petrogenesis and crustal evolution," *Precambrian Research*, vol. 47, no. 1–2, pp. 35–50, 1990.
- [21] S. F. Toteu, W. R. Van Schmus, J. Penaye, and J. B. Nyobé, "UPb and SmNd evidence for Eburnian and Pan-African high-grade metamorphism in cratonic rocks of southern Cameroon," *Precambrian Research*, vol. 67, no. 3–4, pp. 321–347, 1994.
- [22] C. K. Shang, M. Satir, W. Siebel et al., "TTG magmatism in the Congo craton; a view from major and trace element geochemistry, Rb-Sr and Sm-Nd systematics: case of the Sangmelima

- region, Ntem complex, southern Cameroon," *Journal of African Earth Sciences*, vol. 40, no. 1-2, pp. 61-79, 2004.
- [23] R. Tchameni, "Géochimie et géochronologie des formations de l'Archéen et du Paléoprotérozoïque du Sud-Cameroun (Groupe du Ntem, Craton du Congo)," *Orléans*, 1997.
- [24] J. P. Brun and J. Pons, "Strain patterns of pluton emplacement in a crust undergoing non-coaxial deformation, Sierra Morena, Southern Spain," *Journal of Structural Geology*, vol. 3, no. 3, pp. 219-229, 1981.
- [25] W. J. Collins, "Polydiapirism of the Archean Mount Edgar Batholith, Pilbara Block, Western Australia," *Precambrian Research*, vol. 43, no. 1-2, pp. 41-62, 1989.
- [26] H. Bouhallier, P. Choukroune, and M. Ballèvre, "Diapirism, bulk homogeneous shortening and transcurrent shearing in the Archean Dharwar craton: the Holenarsipur area, southern India," *Precambrian Research*, vol. 63, no. 1-2, pp. 43-58, 1993.
- [27] P. Choukroune, H. Bouhallier, and N. T. Arndt, "Soft lithosphere during periods of Archean crustal growth or crustal reworking," *Geological Society, London, Special Publications*, vol. 95, pp. 67-86, 1995.
- [28] J. P. Vicat, J.-M. Léger, E. Nsifa et al., "Distinction, au sein du craton congolais du sud-ouest du Cameroun, de deux épisodes doléritiques initiant les cycles orogéniques éburnéen (Paléoprotérozoïque) et panafricain (Néoprotérozoïque)," *Comptes Rendus de l'Académie des Sciences. Série 2. Sciences de la Terre et des Planètes*, vol. 323, pp. 575-582, 1996.
- [29] N. Nsifa, "Magmatisme et evolution géodynamique de l'archéen au protérozoïque de la bordure nord-ouest du Craton du Congo (Complexe du Ntem) au Sud-Ouest Cameroun," *These de Doctorat d'Etat*, 2006.
- [30] P. Maurizot, A. Abessolo, J. Feybesse, V. Johan, and P. Lecomte, "Etude et prospection minière du Sud-Ouest Cameroun. Synthèse des travaux de 1978 à 1985," *Rapport BRGM 85 CMR*, vol. 66, article 274p, 1986.
- [31] R. Tchameni, K. Mezger, N. E. Nsifa, and A. Poulet, "Neoproterozoic crustal evolution in the Congo Craton: Evidence from K rich granitoids of the Ntem Complex, southern Cameroon," *Journal of African Earth Sciences*, vol. 30, no. 1, pp. 133-147, 2000.
- [32] J. Feybesse, L. P. Barbossa, C. Guerrot et al., "Paleoproterozoic tectonic regime and markers of the archean/proterozoic boundary in the Congo-Sao Francisco craton EUG 8," *Terra Abstracts*, vol. 100, 1995.
- [33] F. Koumetio, D. Njomo, C. N. Tatchum, A. P. Tokam, T. C. Tabod, and E. Manguelle-Dicoum, "Interpretation of gravity anomalies by multi-scale evaluation of maxima of gradient and 3D modeling in Bipindi region (South-West Cameroon)," *International Journal of Geosciences*, vol. 5, no. 12, pp. 1415-1425, 2014.
- [34] N. Nfomou, A. F. Tongwa, U. R. Ubangoh, A. Bekoa, N. J. Metuk, and H. J. Victor, "The July 2002 earthquake in the Kribi region: Geological context and a preliminary evaluation of seismic risk in southwestern Cameroon," *Journal of African Earth Sciences*, vol. 40, no. 3-4, pp. 163-172, 2004.
- [35] J. Nzenti, *L'Adamaoua panafricain (région de Banyo): une zone clé pour un modèle de la chaîne panafricaine nordéquatoriale au Cameroun [These Doctorat D'Etat]*, Université Cheikh Anta Diop-Université de Nancy I, 1998.
- [36] B. R. Rosendahl and H. Groschel-Becker, "Deep seismic structure of the continental margin in the Gulf of Guinea: a summary report," *Geological Society, London, Special Publications*, vol. 153, pp. 75-83, 1999.
- [37] P. G. Wilson, J. P. Turner, and G. K. Westbrook, "Structural architecture of the ocean-continent boundary at an oblique transform margin through deep-imaging seismic interpretation and gravity modelling: Equatorial Guinea, West Africa," *Tectonophysics*, vol. 374, no. 1-2, pp. 19-40, 2003.
- [38] M. Tchindjang, "Paradoxes et risques dans les hautes terres camerounaises: multifonctionnalité naturelle et sous valorisation humaine," in *Paradoxes et risques dans les hautes terres camerounaises: multifonctionnalité naturelle et sous valorisation humaine*, Université de Paris, Paris, France, article 266 edition, 2012.
- [39] J. D. Hedberg, *A Geological Analysis of the Cameroon trend*, Princeton University, 1969.
- [40] R. Tchameni, K. Mezger, N. E. Nsifa, and A. Poulet, "Crustal origin of early proterozoic syenites in the congo craton (ntem complex), south cameroon," *Lithos*, vol. 57, no. 1, pp. 23-42, 2001.
- [41] S. Hammer, "Terrain corrections for gravimeter stations," *Geophysics*, vol. 4, no. 3, pp. 184-194, 1939.
- [42] J. M. Nnange, *The Crustal Structure of the Cameroon Volcanic Line and the Fombar Shear Zone Based on Gravity and Aeromagnetic Data*, University of Leeds, 1991.
- [43] Y. N. Shandini, J. M. Tadjou, C. T. Tabod, and J. D. Fairhead, "Gravity data interpretation in the northern edge of the Congo Craton, South-Cameroon," *Anuário do Instituto de Geociências*, vol. 33, 2010.
- [44] D. Gómez-Ortiz, R. Tejero-López, R. Babín-Vich, and A. Rivas-Ponce, "Crustal density structure in the Spanish central system derived from gravity data analysis (Central Spain)," *Tectonophysics*, vol. 403, no. 1-4, pp. 131-149, 2005.
- [45] D. J. Thomson, "Spectrum estimation and harmonic analysis," *Proceedings of the IEEE*, vol. 70, no. 9, pp. 1055-1096, 1982.
- [46] J. M. Lees and J. Park, "Multiple-taper spectral analysis: a stand-alone C-subroutine," *Computers & Geosciences*, vol. 21, no. 2, pp. 199-236, 1995.
- [47] D. B. Percival and A. T. Walden, *Spectral Analysis for Physical Applications*, Cambridge University Press, 1993.
- [48] M. Ghil, M. R. Allen, and M. D. Dettinger, "Advanced spectral methods for climatic time series," *Reviews of Geophysics*, vol. 40, no. 1, pp. 3-1-3-41, 2002.
- [49] D. Slepian, "Prolate spheroidal wave functions, fourier analysis, and uncertainty—V: the discrete case," *Bell System Technical Journal*, vol. 57, no. 5, pp. 1371-1430, 1978.
- [50] J. Park, C. R. Lindberg, and F. L. Vernon, "Multitaper spectral analysis of high-frequency seismograms," *Journal of Geophysical Research: Atmospheres*, vol. 92, no. B12, pp. 12675-12684, 1987.
- [51] P. S. Naidu, "Statistical structure of aeromagnetic field," *Geophysics*, vol. 35, no. 2, pp. 297-292, 1970.
- [52] F. J. R. Syberg, "A fourier method for the regional-residual problem of potential fields," *Geophysical Prospecting*, vol. 20, no. 1, pp. 47-75, 1972.
- [53] B. H. Jacobsen, "A case for upward continuation as a standard separation filter for potential-field maps," *Geophysics*, vol. 52, no. 8, pp. 1138-1148, 1987.
- [54] L. L. Nettleton, "Regionals, residuals, and structures," *Geophysics*, vol. 19, no. 1, pp. 1-22, 1954.
- [55] L. Guo, X. Meng, and Z. Chen, "Preferential upward continuation and the estimation of its continuation height," in *Proceedings of the Beijing 2009 International Geophysical Conference and Exposition*, vol. 2009, pp. 227-227, Beijing, China, 2009.

- [56] H. Zeng, D. Xu, and H. Tan, "A model study for estimating optimum upward-continuation height for gravity separation with application to a Bouguer gravity anomaly over a mineral deposit, Jilin province, northeast China," *Geophysics*, vol. 72, no. 4, pp. 145–150, 2007.
- [57] R. Roberts, W. Hinze, D. Leap, and S. Ward, "Data enhancement procedures on magnetic data from landfill investigations," *Geotechnical and Environmental Geophysics*, vol. 2, pp. 261–266, 1990.
- [58] R. L. Parker, "The rapid calculation of potential anomalies," *The Geophysical Journal of the Royal Astronomical Society*, vol. 31, no. 4, pp. 447–455, 1973.
- [59] D. W. Oldenburg, "Inversion and interpretation of gravity anomalies," *Geophysics*, vol. 39, no. 4, pp. 526–536, 1974.
- [60] R. Nagendra, P. V. S. Prasad, and V. L. S. Bhimasankaram, "Forward and inverse computer modeling of a gravity field resulting from a density interface using Parker-Oldenberg method," *Computers & Geosciences*, vol. 22, no. 3, pp. 227–237, 1996.
- [61] K. Burke, L. D. Ashwal, and S. J. Webb, "New way to map old sutures using deformed alkaline rocks and carbonatites," *Geology*, vol. 31, no. 5, pp. 391–394, 2003.
- [62] J. Vicat, G. Moloto-A-Kenguemba, and A. Pouclet, "Granitoids of the Proterozoic cover of the Congo craton northern edge (South-East of Cameroon and South-West of the Central African Republic), witnesses of a post-Kibarian to pre-Pan-African magmatic activity," *Comptes Rendus de l'Académie des Sciences-Series IIA-Earth and Planetary Science*, vol. 332, no. 4, pp. 235–242, 2001.
- [63] F. Koumetio, D. Njomo, C. T. Tabod, T. C. Noutchogwe, and E. Manguelle-Dicoum, "Structural interpretation of gravity anomalies from the Kribi-Edea zone, South Cameroon: A case study," *Journal of Geophysics and Engineering*, vol. 9, no. 6, pp. 664–673, 2012.
- [64] R. Tchameni, C. Lerouge, J. Penaye et al., "Mineralogical constraint for metamorphic conditions in a shear zone affecting the Archean Ngoulamakong tonalite, Congo craton (Southern Cameroon) and retentivity of U-Pb SHRIMP zircon dates," *Journal of African Earth Sciences*, vol. 58, no. 1, pp. 67–80, 2010.
- [65] J. Tadjou, E. Manguelle-Dicoum, S. Nguiya, and J. Kamguia, "Caractéristiques des anomalies gravimétriques du sous-bassin sédimentaire de Kribi-Campo (Sud-Cameroun)," *Africa Geo-science Review, Special Publication*, vol. 1, pp. 39–50, 2008.
- [66] R. L. Rudnick and D. M. Fountain, "Nature and composition of the continental crust: A lower crustal perspective," *Reviews of Geophysics*, vol. 33, no. 3, pp. 267–309, 1995.
- [67] O. Jagoutz and P. B. Kelemen, "Role of arc processes in the formation of continental crust," *Annual Review of Earth and Planetary Sciences*, vol. 43, pp. 363–404, 2015.
- [68] B. Maunder, J. van Hunen, V. Magni, and P. Bouilhol, "Relamination of mafic subducting crust throughout Earth's history," *Earth and Planetary Science Letters*, vol. 449, pp. 206–216, 2016.
- [69] H. Ngatchou, S. Nguiya, M. Owona Angue, P. Mouzong, and A. Tokam, "Source characterization and tectonic implications of the M4.6 Monatélé (Cameroon) earthquake of 19 March 2005," *South African Journal of Geology*, vol. 121, no. 2, pp. 191–200, 2018.
- [70] O. A. Clotilde, A. S. Patrick, N. Nfor et al., "Determination of the structural lineaments in the Kribi-Campo-Ma'an Area from a multi-scale analysis of gravity data using the HGM and euler 3D deconvolution approaches," *International Journal of Geosciences*, vol. 07, no. 09, pp. 1122–1143, 2016.
- [71] O. A. M. L. Clotilde, T. C. Tabod, N. Séverin, K. J. Victor, and T. K. A. Pierre, "Delineation of lineaments in south cameroon (central africa) using gravity data," *Open Journal of Geology*, vol. 3, article 331, 2013.

Research Article

The Mitla Landslide, an Event That Changed the Fate of a Mixteco/Zapoteco Civilization in Mesoamerica

V. H. Garduño-Monroy ¹, A. Figueroa-Soto,² N. Magaña-García,³ A. Ruiz-Figueroa,⁴ J. Gómez-Cortés,⁴ A. Jiménez-Haro,³ and V. M. Hernández-Madrigal¹

¹UMSNH-INICIT-MGPT, Edificio U Ciudad Universitaria, Morelia, Mich., Mexico

²CONACyT-Instituto de Investigaciones en Ciencias de la Tierra, UMSNH, Mexico

³GEMEX, Mexico

⁴MGYPT-UMSNH, Mexico

Correspondence should be addressed to V. H. Garduño-Monroy; vhgardunom@gmail.com

Received 26 November 2018; Revised 6 February 2019; Accepted 24 March 2019; Published 2 May 2019

Academic Editor: Marek Grad

Copyright © 2019 V. H. Garduño-Monroy et al. This is an open access article distributed under the Creative Commons Attribution License, which permits unrestricted use, distribution, and reproduction in any medium, provided the original work is properly cited.

Before the arrival of the Spanish conquerors, Mitla was the second most important city in the valleys of Oaxaca, México. However, the ruins that are visible today do not seem to match the size of a city of more than 10,000 inhabitants. Geological and geophysical studies suggest that part of the city was covered by the deposits of a dry landslide likely to have been caused by an earthquake with a magnitude that could vary between 6 and 7. This landslide is monolithological, which is why two geophysical methods were used in order to evaluate its geometrical characteristics and to suggest the possible existence of archeological remains under the landslide.

1. Introduction

Many hypotheses regarding the collapse of Mesoamerican cultures have been linked to wars, conquests, epidemics, or climate changes. However, Mesoamerica is located in a context presenting exceptional seismic, volcanic, and meteorological phenomena. Past and current events in México (Tehuantepec, Pinotepa Nacional or Morelos-Puebla earthquakes ~M8, SSN) indicate that tsunamis, earthquakes, and volcanic eruptions countered the development of many important civilizations. For instance, the collapse of Maya culture is insistently related to a large drought, yet very few theories associate these human extinctions with exceptional events. Much of this disaster information was written in the codices. These documents contain data with place and time specifications, also providing information on natural disaster scenarios. For example, in the Telleriano-Remensis codex, tlacuilos recorded approximately 12 seismic events that include glyphs that suggest a scale of environmental effects that appears similar to ESI2007 [1].

The location of Mesoamerica compels us to think that those cultures witnessed very important seismic and volcanic

events. For instance, the birth of the Tarascan empire is clearly linked to changes in the landscape due to an earthquake and to the birth of Capaxtiro volcano [2]. Besides the areas towered by volcanos, earthquakes caused important imbalances or prophecies, such as the fourth bad omen described by León Portilla [3], which warned the Aztecs about the arrival of the Spanish conquerors (The burning lake, *El Lago en Llamas*): “Texcoco Lake burned, its boiling waters swelled and swept the houses, killing many”. This description is certainly very close to an account of the formation of a tsunami caused by an earthquake.

On the other hand, the ongoing seismic activity in the State of Oaxaca brought about a particular architectural practice: in order to resist violent earthquakes, the churches have very thick walls, huge buttresses, and short towers (Figure 1).

The study of the effects of important earthquakes can be carried out according to different environmental or anthropogenic results. In present case the research focuses on the geophysical analysis of the Mitla Landslide. As in this case the collapse was caused by an earthquake, the techniques selected were ground-penetrating radar and electrical tomography

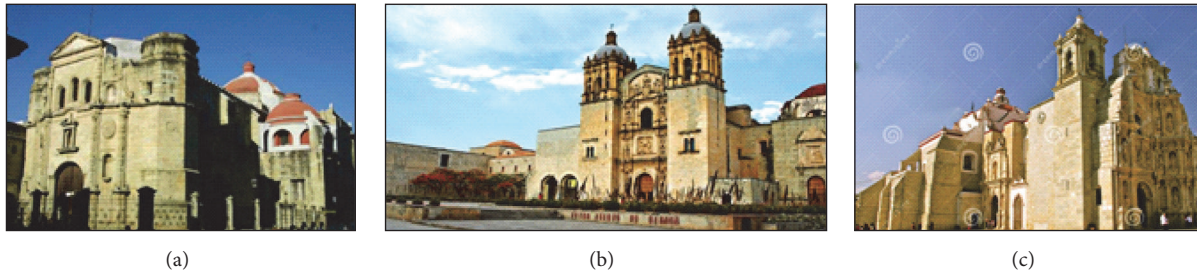


FIGURE 1: Churches in Oaxaca City feature short towers and huge buttresses. (a) La Compañía Church, (b) Church of Santo Domingo, and (c) Basílica of Our Lady of Solitude.

and cross- correlations of seismic ambient noise records. The two last were those that yielded the best results. Eventually the use of the radar was not a good option due to the homogeneity of the landslide and for the little penetration of this, which in this case is monolithologic. Conversely, electrical tomography was an adequate method. The use of seismic noise and the advantage of a regional earthquake register allowed us to find a clear lithological contrast.

2. Tectonic Setting of Oaxaca

Oaxaca is one of the major earthquake zones of México, due to the Cocos plate subduction under the North American plate and the seismic activity related to intraplate structure that causes shallow quakes, such as the Xalapa earthquake of 1920. Oaxaca has been affected by a large number of seismic events with magnitudes above 7 (Table 1, data provided by the Servicio Sismológico Nacional (SSN), UNAM 2018), so much so that Fray Juan de Córdova's *Vocabulario en lengua zapoteca* (1578) contains words to designate the tremor of the earth: *xoo*, but also a name for the deity of earthquakes: *Pitao xoo*.

Beside subduction earthquakes, Oaxaca presents intraplate faulting related to the limits of tectonic terranes expressed in the Central and Tehuacan valleys. The Central valleys of Oaxaca are part of the Oaxaca fault system, which is formed at the borders between the Zapoteco and Cuicateco terranes (Figure 2(a)), and besides its normal component has always been thought to have a horizontal component in arguable direction (Figure 2(c), [4].

The seismicity reported by the Servicio Sismológico Nacional (SSN) and presented in Figure 2(c) corresponds to the intraplate events zone in the south-east zone of México named by Zúñiga et al. [5] as NAM and matches the intraplate seismicity of the southeastern zone of México that is not related to the volcanism of the Trans Mexican Volcanic Belt; its maximum depth has been measured at 20 km.

The focal mechanisms presented in Figure 2(b) correspond to quakes of magnitude over 7 and were taken from the IRIS (Incorporated Research Institution for Seismology) consortium. Most of these focal mechanisms are associated with the zone of strong coupling between the Cocos and North American tectonic plates (interplate, reverse faulting) and others to rupture processes of the subducted Cocos plate (normal faulting).

Recently, in 2017 and 2018, major events occurred again in Oaxaca, the first on September 7 with magnitude 8.2 Mw

and epicenter located in the Gulf of Tehuantepec, 137 km southeast of Pijijiapan (Chiapas), and 46 km deep. This event is mainly related to normal faulting (79° dip) that caused the complete rupture of the lithosphere in a zone related to the seismic gap of Tehuantepec, in which no event of this magnitude had taken place since 1787, when an earthquake of $M_w \approx 8.6$ occurred [6].

The second event happened on Friday February 16, 2018, of magnitude 7.2 Mw and epicenter 11 km from Pinotepa Nacional, Oaxaca. Both events caused material and human losses.

It is important to mention that regarding recurrence periods for the central zone of the State of Oaxaca, Zúñiga et al. [5] report periods of 6 years for quakes with magnitudes above 5 occurring in the NAM zone (shallow events with depth under 20 km), periods of 109 years for magnitudes above 7 taking place within the subducted Cocos plate (intraplate events with depths of 40 to 180 km), and periods of 37 years for quakes of magnitudes above 7.5 occurring in the coupling zone of the Cocos and North American tectonic plates (subduction area).

On the other hand, previous refraction and reflection studies across the Oaxaca fault [7, 8] did not confirm that it runs as deep as presumed. Supporting this result, the regional magnetotelluric study by Jödicke [9] did not detect the expected large electric contrast across the Oaxaca fault at crustal depths along a transect passing south of Oaxaca City. By analyzing the electrical impedance along a regional transect, Jording et al. [10] concluded that the major structural change at depth in this region is displaced northeastwards of the Mitla Valley, about 30 km east from the generally accepted Oaxaca-Juárez terrane boundary. A more detailed MT study of the region [11] concluded that the Oaxaca fault system does not appear to penetrate deep into the crust but remains relatively shallow (5 km). Other results [12] also suggest that the contact between the Oaxaca and Juárez terranes at crustal depths occurs along a SW-dipping interface south of Oaxaca City [13].

3. Study Zone and Landslide

The town of Mitla is located south of Oaxaca City ($16^\circ 55' 41.3''$ - $96^\circ 21' 33.8''$ - 1706 m a.s.l.) in a vale of NW-SE orientation. It presents evident morphological contrasts that have molded Precambrian, Tertiary, and current rocks, thereby forming sierra and valleys in the same direction, and

TABLE 1: Earthquakes above M7 in Oaxaca from 1787 to 2018 (Servicio Sismológico Nacional, UNAM 2018).

Year	Month	Day	Magnitude	Depth	Reference
1787	3	28	8.6	?	Tehuantepec Ridge. Tsunami in the Coast of Oaxaca
1916	6	2	7	150.0	42 km south of SAYULA DE ALEMAN, VER
1928	3	21	7.5	33.0	12 km southeast of CRUECITA, OAX
1928	6	16	7.6	33.0	11 km west of MIAHUATLAN, OAX
1928	8	4	7.4	33.0	49 km south of H TLAXIACO, OAX
1928	10	8	7.5	33.0	35 km northeast of RIO GRANDE, OAX
1931	1	15	7.4	40.0	30 km west of MIAHUATLAN, OAX
1937	12	23	7.4	33.0	46 km southwest of H TLAXIACO, OAX
1948	1	6	7	80.0	45 km southeast of H TLAXIACO, OAX
1950	12	14	7.2	33.0	47 km west of H TLAXIACO, OAX
1951	12	11	7	100.0	59 km east of MATIAS ROMERO, OAX
1965	8	23	7.5	12.0	53 km northeast of CRUECITA, OAX
1968	8	2	7.3	16.0	39 km northeast of PINOTEPA NACIONAL, OAX
1973	8	28	7.3	82.0	30 km southwest of TIERRA BLANCA, VER
1978	11	29	7.6	23.0	32 km northwest of S PEDRO POCHUTLA, OAX
1980	10	24	7.1	65.0	19 km west of ACATLAN DE OSORIO, PUE
1982	6	7	7	19.0	20 km southeast of OMETEPEC, GRO
1995	9	14	7.3	21.0	29 km northeast of OMETEPEC, GRO
1996	2	24	7.1	15.0	52 km south of PINOTEPA NACIONAL, OAX
1999	6	15	7	63.0	29 km southwest of S GABRIEL CHILAC, PUE
1999	9	30	7.4	39.0	22 km northeast of PUERTO ESCONDIDO, OAX
2012	3	20	7.5	18.0	46 km south of OMETEPEC, GRO
2017	9	7	8.2	45.9	140 km southwest of PIJIJAPAN, CHIS
2017	9	19	7.1	38.5	9 km northeast of CHIAUTLA DE TAPIA, PUE
2018	2	16	7.2	12.0	11 km south of PINOTEPA NACIONAL, OAX

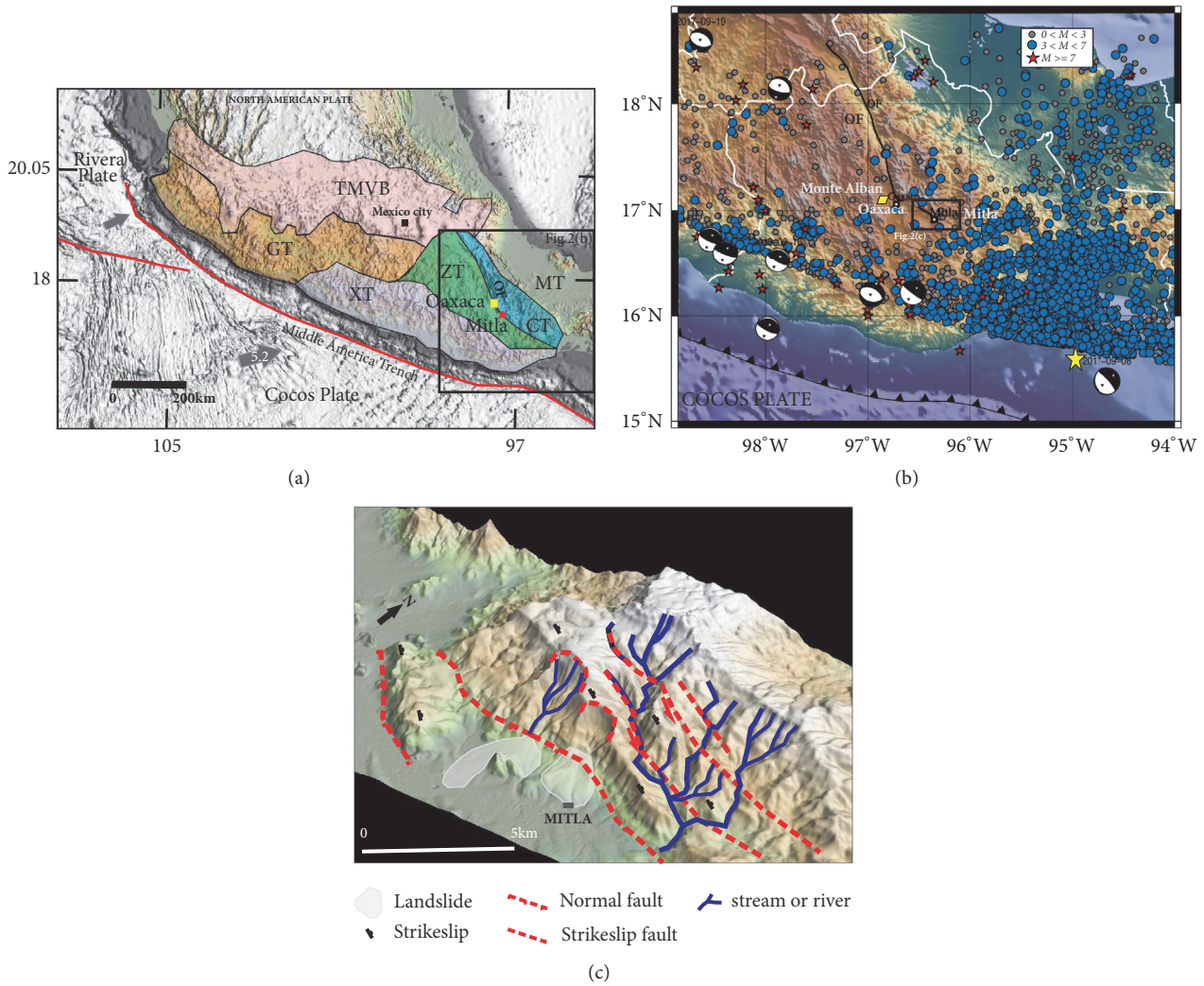


FIGURE 2: (a) Tectonic scheme of the south of México: TMVB (Transmexican Volcanic Belt), GT (Guerrero Terrane), ZT (Zapoteco Terrane), XT (Xolapa Terrane), CT (Cuicateco Terrane), MT (Maya Terrane), OF (Oaxaca Fault). (b) Seismicity reported by SSN with depths between 0 and 20 km deep and (c) structural scheme of the Mitla area in Oaxaca.

where sometimes the N-S drainage system is modified by NW-SE structures (Figure 2(c)).

The word Mitla or Mictlán is nahuátl and means “Place of the Dead” or “Underworld”. In Zapotec it is called *Lyobaa* which means: “place of graves” or “place of burials”, from the etymology *Lio*: Place and *Baa*: grave or burial [14]; in mexica it remained Mictlán, “Place of the Dead”, or “place of many corpses”, and was hispanicized to Mitla. Contrary to Monte Albán, the heyday of Mitla occurred between 950 and 1521 AD. The settlements of Mitla have been estimated to be over 7,000 km² large, with a population of around 10,000 inhabitants. One of its main characteristics are constructions decorated with elaborate mosaic fretwork (*grecales*) featuring variations of the same geometric design, and the cross-shaped tombs that have been found under the palaces, in which important people and priests were probably buried. The archeological complex includes several structures, two of which were covered with Christian buildings, the most important of which was constructed in 1590. The San Pablo

church was erected in one of the prehispanic courts of Mitla using stones from the temples themselves. The basic architectural form of the few pyramids shows paraseismic techniques, visible both in the Las Columnas site as in the Grupo Arroyo, where notches appear in the frames of all the entrances to the rooms.

During our field work the avalanche deposit was identified for the first time in all the surroundings of the archeological remains of San Pablo Villa de Mitla. Previous works mapped the avalanche as part of pyroclasts deposits [15]. Its distal facies seem to have covered part of the pyramids, as shown hereunder and on Figure 3.

4. Methodology

The methodology of this study focused on 5 main guidelines: (a) the first step was to find previous research on Mitla in the fields of Archeology and Geosciences; (b) subsequently, a 50 cm-definition terrain model was mapped with a drone; (c)

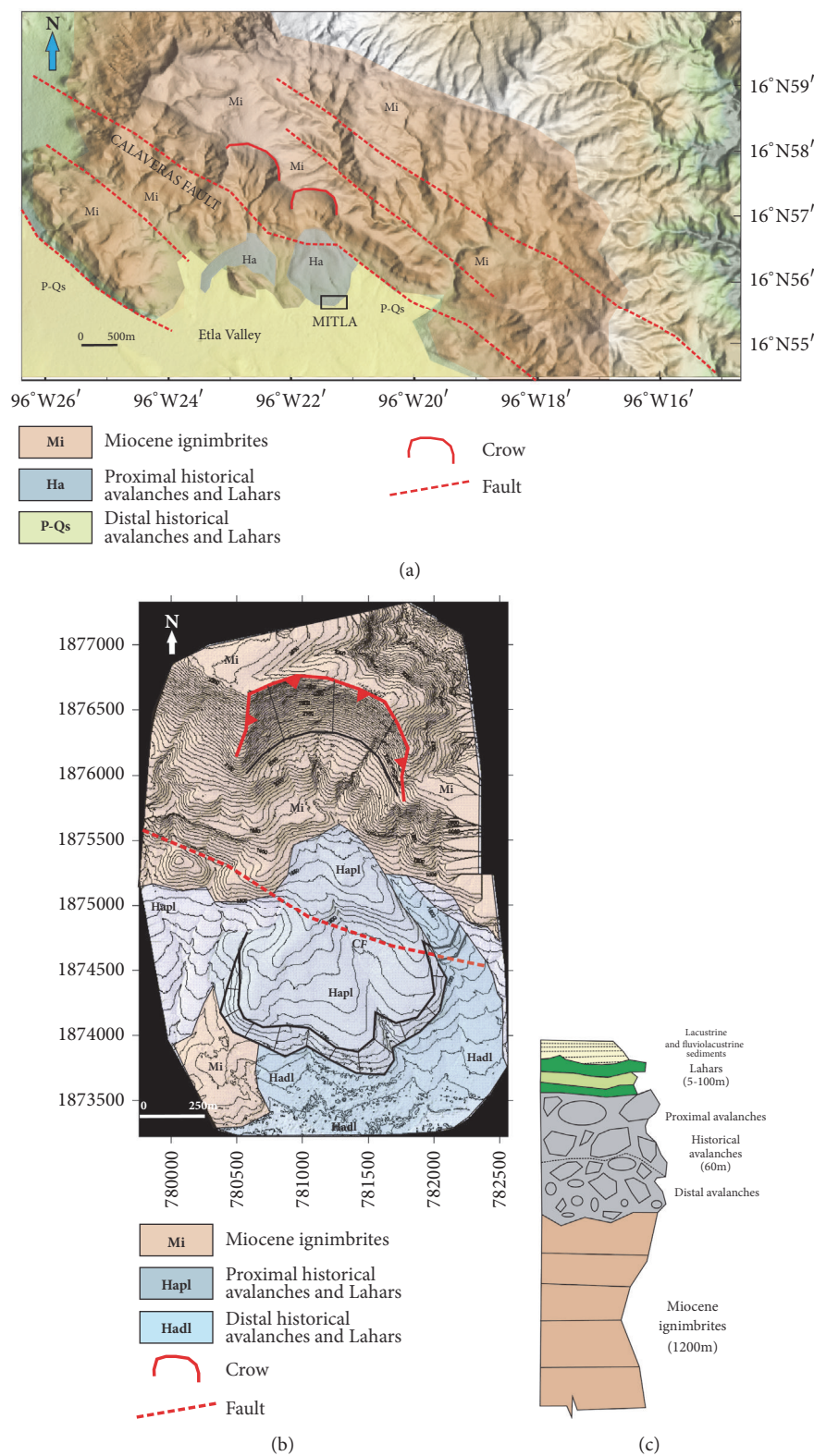


FIGURE 3: (a) Regional geology of the valley of Etla. (b) Geology of the Mitla Avalanche. (c) Synthesis of the lithological column of Mitla.

geology and all the data regarding geophysical, morphostructural; (d) stratigraphical characterization, structural geology in the Sierra Calaveras and (e) the geomechanical study of the landslide were based upon this model.

Various columns were extracted from the landslide to study its geology. Once the lithology was understood, the area was mapped in detail.

Several methodologies were applied regarding geophysics, such as ground-penetrating radar (Mala) and electrical and seismic tomography. The first method was not adequate due to insufficient penetration and scarce lithological contrast. The seismic and electrical tomographies, however, yielded valuable results.

Reconnaissance methods, which mainly include remote-sensing and aerial techniques, geological and geomorphological mapping, and geophysical and geotechnical techniques, had to be adapted to the characteristics of the landslide. According to McCann and Foster [16], a geotechnical appraisal of the landslide's stability has to consider the three following issues: (1) the definition of the 3D geometry of the landslide with particular emphasis on failure surfaces, (2) the definition of the hydrogeological regime, and (3) the detection and characterization of the movement.

The method for seismicity was to obtain velocity profiles using horizontal-to-vertical spectral ratios (H/V ratios) of microtremors [17, 18] named Nakamura method, and inversion with the Spatial Auto-correlation Method [19] and with the H/V [20] based on ambient noise measurements carried out with 3 long-period Trillium Compact 120s sensors with frequency responses of 120s to 100 Hz, and their respective RefTek 130S three channel and 24 bits-resolution third generation recorders. Regarding microtremors, it was taken into account that the energy sources are multidirectional [18]; thus, the direction of maximum movement is unknown. Moreover, the use of this kind of technique does not cause environmental impact and yields precise results.

Microtremors, also called ambient vibration noise, seismic microtremors, or background seismic noise, are random vibrations generated by natural or artificial sources. The aim of the Nakamura method and the SPAC technique was to determine velocity profiles in the northern region of the archeological zone of Mitla in order to determine the depth of the base of the landslide.

The H/V technique was developed by [18] and is used for obtaining direct estimates of site-specific response during an earthquake (e.g., [21, 22]), with relating geological and geophysical properties of Wells together with seismic records analysis on the various geological site conditions. It was hypothesized that the vertical component of the ambient noise at the ground surface keeps the characteristics of basement ground, is relatively influenced by Rayleigh wave on the sediments, and can therefore be used to remove both the source and the Rayleigh wave effects from the horizontal components. It is effective in identifying the fundamental resonance frequency of a sedimentary layer, where the depth H of a soft soil layer with resonance frequency F and shear wave velocity V_s is given by $H = V_s/(4 \cdot F)$.

The H/V spectral ratio of microtremors measured anywhere confirmed its ability to estimate the predominant

frequency and the amplification factor. The result of the estimation is stable for the measured time and season (Nakamura, 1989).

The seismic noise records were visually inspected to select signals that are complete and that had a good signal-to-noise ratio. Two software packages were used for data processing: SAC (Seismic Analysis Code) and Geopsy (Geophysical Signal Database for Noise Array Processing) (SESAME WP05) [23]. The results of these programs were compared because they have a different smoothing function in obtaining H/V [24].

H/V spectral ratios were calculated for the three components of each record. This was done automatically when estimating the H/V ratio with the Geopsy software. For the calculation of H/V for each selected window, a smoothing function was applied with a bandwidth coefficient of $b = 40$ and a 5% cosine taper-window. This type of smoothing function employs a different number of points at low and high frequency; its use is strongly recommended for frequency analysis [25].

Using the SAC (Seismic Analysis Code) software, spectral ratios were determined in 81.92 seconds windows and a smoothing with a Von Hann window [26]. The results of both programs did not show significant differences.

The method known as SPAC (spatial autocorrelation method) was first introduced in 1957 by [27]. The SPAC method considers the dispersive characteristics of surface waves in a stratified medium [28]. When only the vertical component of seismic noise record is used, we can easily assume that the signal has a high content of Rayleigh waves.

In this method, it is proposed that from simultaneous microtremor measurements in some geometric arrangements of seismic stations, it is possible to obtain the dispersion curve by calculating the coefficient of spatial autocorrelation [29].

We represent harmonic wave circular microtremor frequency ω by $u(0, 0, \omega, t)$ and $u(r, \theta, \omega, t)$, which are observed in the center $C(0,0)$ of the array and point $X(r, \theta)$ on the circle of radius r . Then spatial autocorrelation function is defined as

$$\varphi(r, \theta, \omega) = \overline{u(0, 0, \omega, t) u(r, \theta, \omega, t)} \quad (1)$$

where $u(t)$ is the average value in the time domain. The spatial autocorrelation coefficient for one angular frequency ω , $p(\omega, r)$, or simply autocorrelation coefficient is defined as the power spectrum of one station within a spatial arrangement (middle circle):

$$\rho(f, r) = J_0\left(\frac{2\pi fr}{c(f)}\right) \quad (2)$$

Therefore, the spatial autocorrelation coefficient at a frequency f is related to the phase velocity $c(f)$ through the Bessel function of first kind and zero order J_0 . The phase velocity calculated from the argument of the Bessel function generated (2). For the SPAC technique, we used Geopsy software [23]. Prior to making rings, correlation graphs were generated, and the dispersion curve was then adjusted.

Seismic noise measurements were taken during two days on the archeological site of Mitla. For each day, a triangular

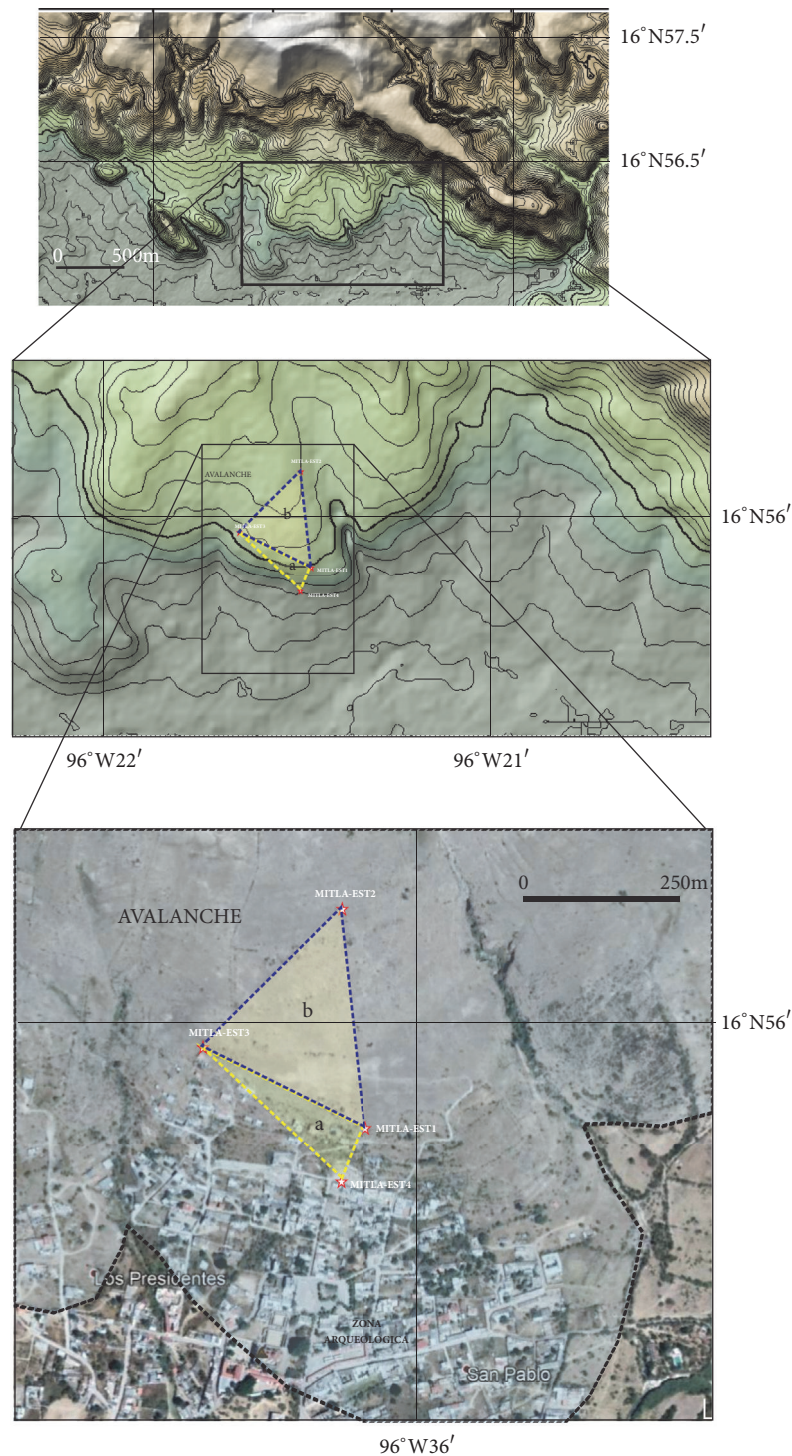


FIGURE 4: (a) Seismic array # 1 and (b) seismic array # 2.

array with three seismic stations and with seismic records with durations of 10 hours (array 1) and 6 hours (array 2) was built (Figure 4).

5. Geoelectrical Tomography

Geoelectrical imaging is geophysical technique that was developed on the basis of physical methods that are helpful to

reveal the presence or absence of buried bodies and structures that cannot be seen with the naked eye, but that can be detected because of their distinctive physical properties of being resistive to their surroundings (e.g., [30–32]).

The aim of geoelectrical mappings is to determine the distribution of resistivity in the subsoil through measurements carried out on the surface. The true resistivity of the subsoil can be estimated from these measurements. In this

sense, the resistivity of the earth is related to geological parameters according to its mineral content, fluid saturation, and rock porosity. Geoelectrical studies have been used for some decades now for hydrological and mining research and for geotechnical research. However, more recently, these methods have become more sophisticated in mapping the subsoils, and they have increasingly been used to locate structures and characterize the subsoil.

The aim of this study is to obtain a 2D model of true resistivities from the pseudosection of apparent resistivities obtained from the field. This is why an inversion program is necessary.

On the other hand, samples of the landslide sediments were submitted to granulometric analysis and evaluation of their petrophysical properties. Unfortunately, neither organic soils, nor pieces of carbon were found to date the landslide.

6. Results

6.1. Geology of the Mitla Area. The stratigraphical column of the Mitla zone is composed of a basement of Precambrian rocks from the Zapoteco terrane covered by Mesozoic carbonated units veiled by pyroclastic flows that constitute Sierra La Calavera. On these sequences and on the hanging wall, huge Pleistocene lacustrine basins developed as part of the large valleys of the study zone, which are actually the hanging wall of the normal NNW-SSE fault carved by other faults following the same direction and which could be responsible for the Mitla Landslide (Figure 3).

The main structures are oriented NNW-SSE and clearly present the geometry of normal faults with strike-slip sinistral component. This fault, which we henceforth call Calaveras fault, is part of the large structures that are the boundaries of the tectonic terranes, especially those that limit the Zapoteco and Cuicateco terranes (Figures 2 and 3).

The ignimbrite sequence of rhyolitic composition is formed of at least two large packages; the inferior package corresponds to the hanging wall of the normal Calavera or Mitla fault outcropping at La Fortaleza and Mitla (Figure 3). The second is the package of Sierra La Calavera and is made of at least 4 thick ignimbrite packages, some of which are welded and others crumblier, but all with Q, PL, and mica crystals; some levels are tightly welded at different points of the column. These were dated between 14.4 ± 0.4 My and 15.48 ± 0.2 My, Miocene [15].

Above the ignimbrites of the hanging wall of the La Calavera fault is a thick landslide deposit formed of different levels but nonetheless of monolithologic composition, i.e., formed only of block and rhyolitic rocks matrix. The blocks range from gravel to blocks of more than 5 m in diameter, some of which are angular and others semirounded. More data regarding this landslide will be given hereunder.

On top of the landslide and the ignimbrites are lahar deposits, varying from blocks and matrix to hyperconcentrated lahars.

Fluviolacustrine deposits were observed in río Mitla formed by conglomerates, sands and clays, all of which heavily faulted. Large Pleistocene vertebrates were reportedly discovered in these deposits [15].

6.2. Geometry of the Collapses and Description of the Deposits. In a detailed elevation model, two large landslide flows can be seen opening towards the south in the Sierra La Calavera, which is formed by tabular deposits of ignimbrites tilted towards the north. Because of its provenance, the most visible of the flows is the Mitla Landslide. This wide scarp and deposit bundle is clearly observable and delimited. The main scarp has a maximum diameter of 1350 m and a slope relief of 390 m. The landslide ran over more than 2500 m from the basis of the main scarp to the toe. The second main scarp, located NNO of Mitla, is less regular, both in its main scarp and in its body (Figure 5). Both main scarps are located within the footwall of the normal fault that caused the Mitla depression.

6.3. Geomechanics and Granulometry. An average per size was obtained, of samples from the avalanche front, from the granulometric data using the sizes of the wire mesh cloth of the sieves used to observe the behavior of one granulometry (Figure 6). As in the case of individual strata, the line does not break, which reveals a fair distribution of the material and very little space among particles.

6.3.1. Φ Value. With an elevation model presenting curve details every 50 cm, we obtained the value of the H/L relation for a length (L) of 1.633 km, and a drop height of 0.640 km, yielding $\Phi=0.39$, which means its value is characteristic of dry landslides, i.e., of 0.5.

6.4. Slope Mobility. Reference [33] introduced an indicator regarding the mobility of slopes called *excessive travel distance*. This parameter (Le) expresses the horizontal distance traveled in excess by the event, superior to what could be expected if the movement was that of a nonlubricated event of rigid mass, which would move across a tilted plane with a normal coefficient of friction of $\tan(32^\circ)$.

$$Le = L - \left(\frac{H}{0.62} \right) \quad (3)$$

$$Le = 1033 \quad (4)$$

As can be observed, the distance covered in excess indicates the movement of the body in the specific conditions mentioned above, and comparing it with the true distance of the slope we can observe that the difference is small, indicating scarcity of water. In cases wherein, water is presented as triggering factor; the difference can be four times higher.

6.5. Geophysics. In order to know the geometry of the landslide, three 2D tomography lines were acquired with $a=4$ m (Figure 8). The vertical resolution obtained was of 2 m and the horizontal resolution of 4 m. Lines 1 and 2 were 108 m long with NE-SW orientation. Line 3 was 156 m long and oriented SE-NW (Figure 7).

Data obtained so far reveal a landslide body of low resistivities (11-17) in blue and in the southern part of the profiles, between 4 and 5 meters from the ground, there is a body of average resistivity (22) colored green and yellow, interpreted as part of the ignimbrite basement or possible remains of pyramids constructed with ignimbrites.

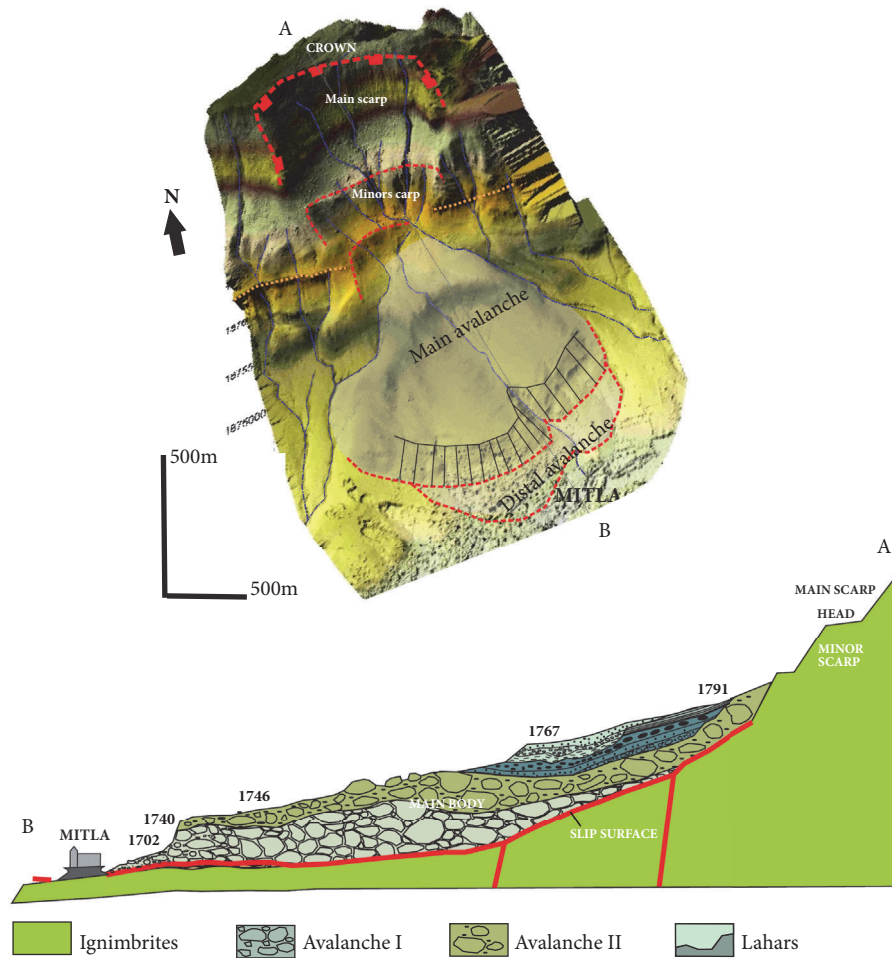


FIGURE 5: Map of the landslide and profile showing the different deposits. (A) The 3D terrain model which is exaggerated in the vertical 2 times. (B) is a schematic field section with heights above sea level (m a.s.l.).

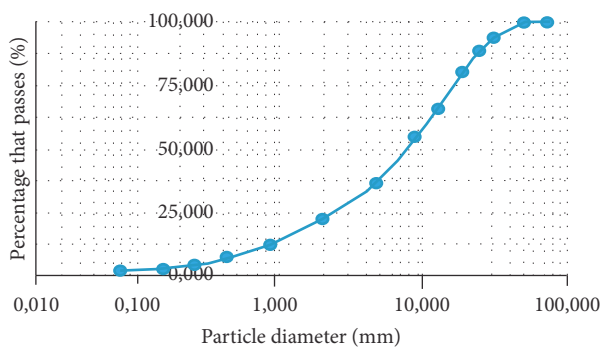


FIGURE 6: Average of granulometries of the 5 strata of the landslide in each of the sieves used for the analysis.

6.6. Seismic Noise Records. On the assumption that the derived dispersion function represents the first mode of the Rayleigh waves, we derived a best-fitting velocity model that is consistent with the estimated velocity values. Figures 8 and 9 show the Rayleigh waves dispersion function for each seismic array.

6.7. Inversion of the H/V Spectral Ratio. Figure 10 presents the H/V spectral ratio for stations 1 and 3 for seismic array # 1. Here, the H/V rotate tool was used to obtain the H/V in the horizontal plane, i.e., as azimuth function, from any type of 3D vibration signals (ambient vibrations, earthquakes, etc.). The black curve represents H/V geometrically averaged over all individual colored H/V curves. The two dashed lines represent the H/V standard deviation. The grey area represents the average peak frequency and its standard deviation. The frequency value is at the limit between the dark grey and light grey areas. The parameters were frequency sampling from 1 Hz to 15 Hz, global time range from T0 to the end of the time series and time windows to 81.92 s.

The inversion of the spectral ratios allows us to obtain a velocity profile for each measurement site. In Table 2 we show the fundamental frequencies for each seismological station and the classification of the type of soil associated with the site based on the NEHRP (National Earthquake Hazards Reduction Program) classification [34].

It was determined that the depth of the base of the landslide is of 50 meters below array 1 (region south of the

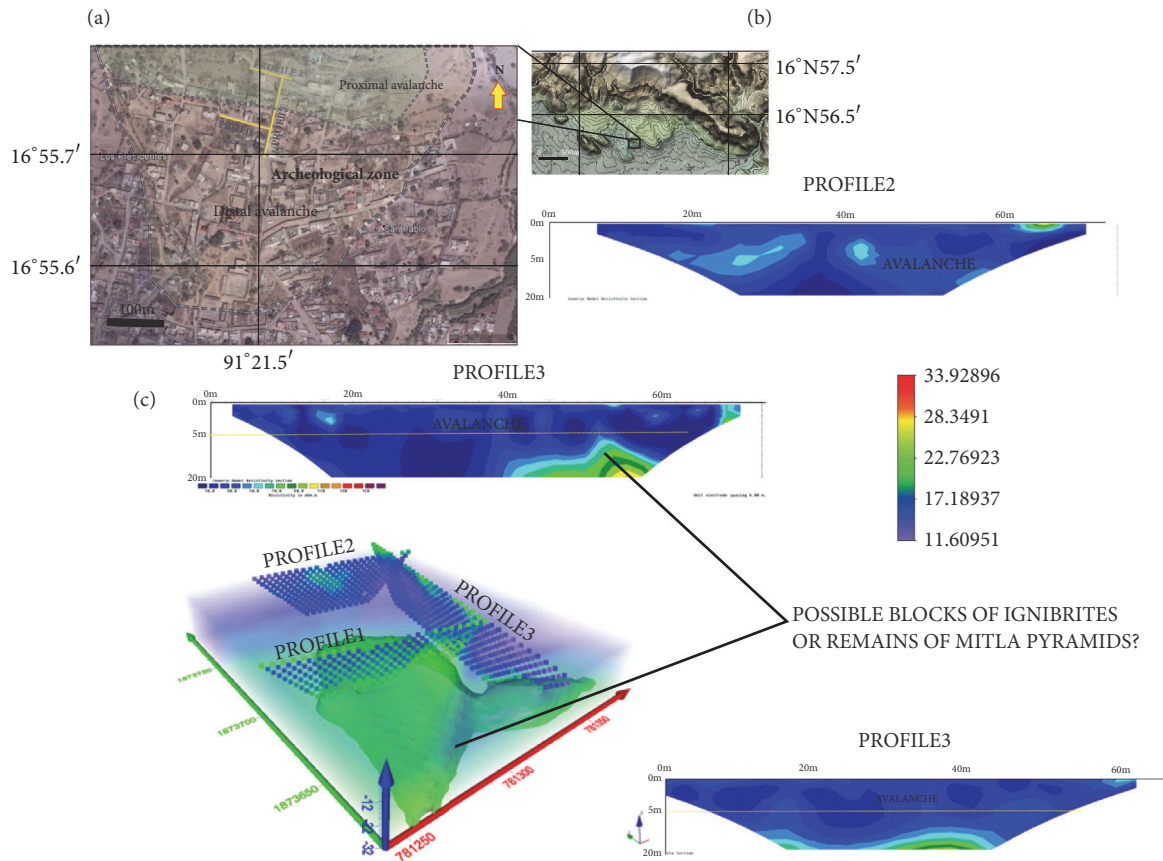


FIGURE 7: Results yielded by electrical tomography. Notable presence of an intermediate resistivity body (12) related to possible pyramid remains (green). The blue could correspond to landslide deposits. Where sections are located, there is the distribution of a 1 to 2,20m thick distal landslide. (a) Location of the three geophysical profiles. (b) Location of the geophysical survey area on the avalanche front. (c) Geophysical profiles and 3D model.

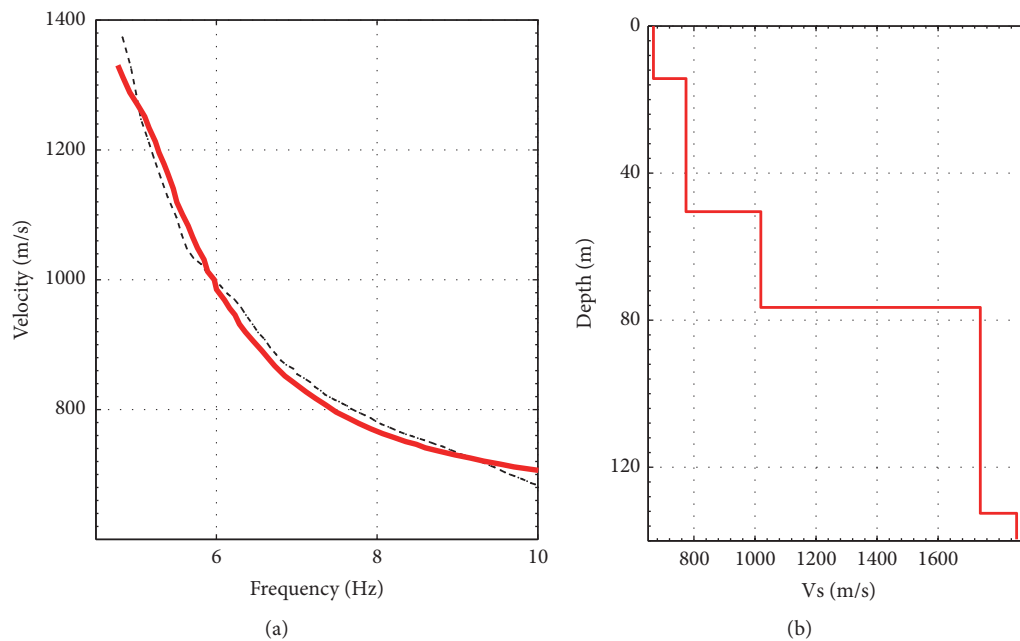


FIGURE 8: Seismic array #1: (a) Rayleigh waves dispersion function. The red line corresponds to the first mode Rayleigh waves dispersion curve as best fit for the experimental values. (b) S-wave velocity model derived in this study.

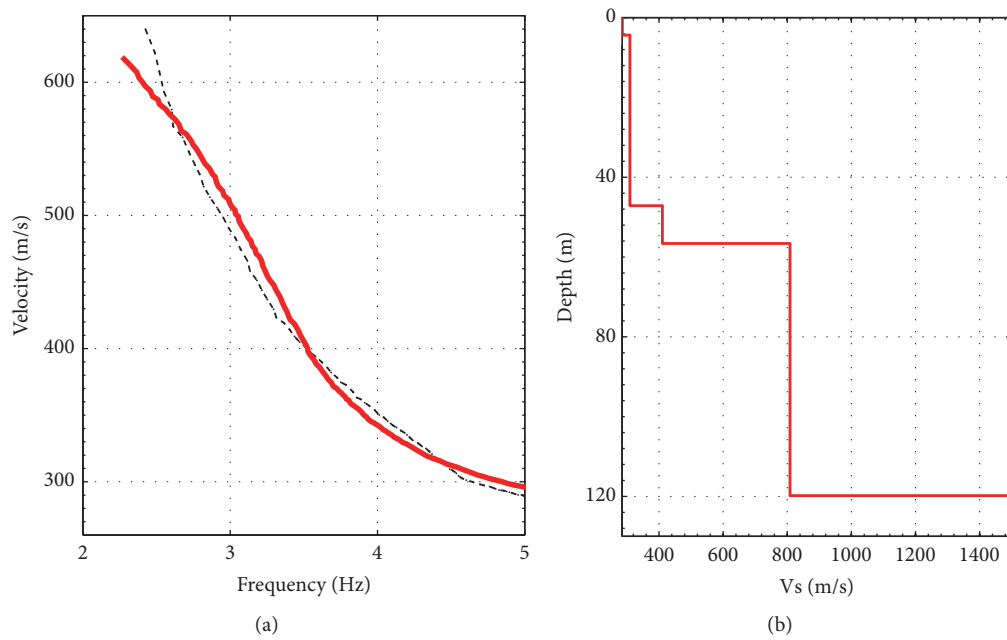


FIGURE 9: Seismic array #2: (a) Rayleigh waves dispersion function. The red line corresponds to the first mode Rayleigh waves dispersion curve as best fit for the experimental values. (b) S-wave velocity model derived in this study.

TABLE 2: Dominant periods and classification of the type of soil for the seismic stations within the different arrays (<http://www.nehrp.gov/>).

FREQUENCY	DOMINANT PERIOD	NEHRP CLASSIFICATION
<i>STATION 1. Array #1 and array #2</i>		
3.17 Hz	0.315 s	Solid Ground
<i>STATION 3. Array #1 and array #2</i>		
3.35 Hz	0.298 s	Solid Ground
<i>STATION 4. Array #1</i>		
12.74 Hz	0.078 s	Rock
<i>STATION 2. Array #2</i>		
1.2 Hz	0.833 s	Soft Ground

archeological site of Mitla) and 70 meters below array 2 (north of the archeological zone).

Supporting these results, the northernmost site can be classified as ground softer than the southernmost site of the triangular arrangements. This can be correlated with the change in the landslide of Mitla.

7. Discussion

The Mitla avalanche opens a great discussion in the field of Geoarchaeology. The geological investigations give evidence that this event occurred in historical time that is during the Postclassic and before the arrival of the Spaniards. The important city of Mitla was found in decline during the arrival of the Spaniards.

The geophysical exploration data show important aspects, as the electrical tomography studies propose the existence of an important anomalous structure under the avalanche that could be part of the remains of the prehispanic Mitla. The elements that compose it were found between 5 and less of 20 m deep. On the other hand, with the earthquakes data

and environmental noise, an avalanche thickness of 60 m was estimated, which allowed a correct calculation of the area and volume of the material removed (area of 2.79 km² and volume of 0.1674 km³). In this same field of the relation between the volume or area removed by the collapse and the magnitude of the earthquake, two published works have been analyzed; one was by [35] and the other by [36]. Both make a great contribution to obtain the relationship between the destabilized areas and the Ms or Mw. However, in all these works they analyzed zones of Central America where the climate and the soils make up very different scenarios from Mitla. Consequently, it is likely that the magnitude proposed in our work does not correspond exactly to the real one, because the avalanche was in dry condition during the collapse, the geometries of the strata bedrock were not favorable to the destabilization, and the local climatic conditions have not allowed a great soils development. Anyway, here there is the morphological evidence that the Calaveras fault is part of an active fault system, as shown from the drainage networks that give the NNW-SSE structures a normal left-lateral component (Figure 2(c)). Despite these

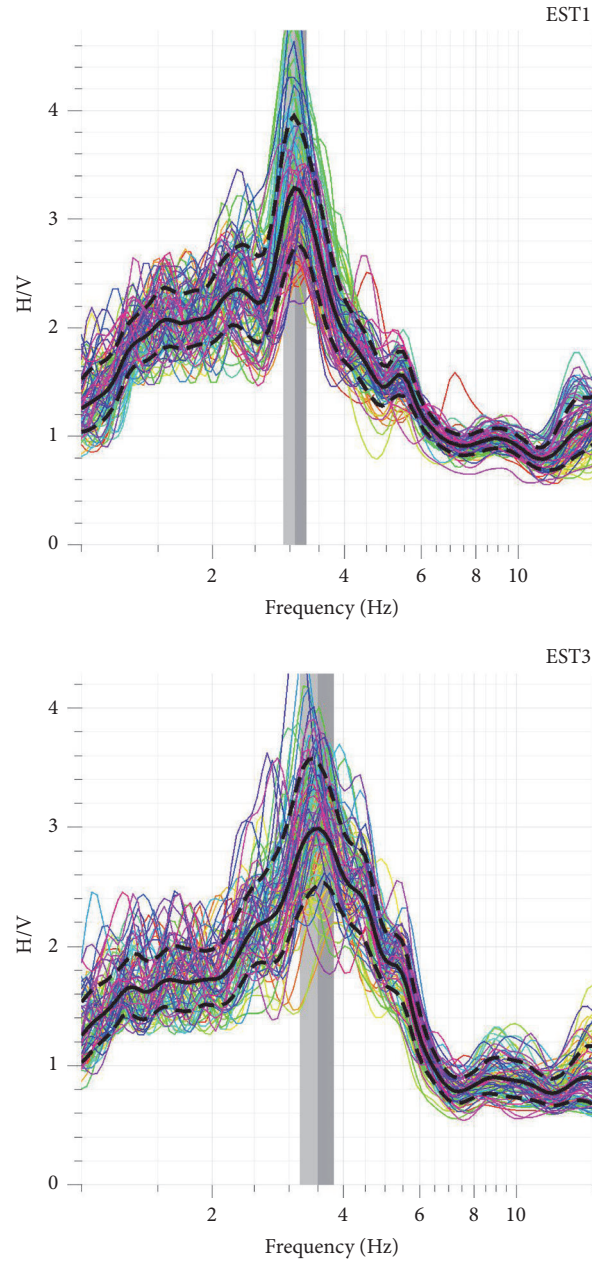


FIGURE 10: Examples of the H/V spectral ratio for two seismic sites.

differences, we have considered keeping Keefer's equation. In this paper we have only estimated the material volume of the Mitla avalanche. However, in later works we will make an estimate of the two avalanches that could have been generated by the same earthquake (Garduño-Monroy et al., in press)

Starting from a maximum volume of 0.1674 km^3 for the landslide, the earthquake that caused the ground shaking up to the slope collapse could have had a maximum magnitude of 7.3 according to the relationship of [35, 36].

If we consider the length of the Calaveras fault (with a minimum length of 10 km and maximum of up to 40 km, Figure 3), it would be potential to generate an earthquake

of magnitude in the range of 6.2 to 6.9 Mw, based on the relations proposed by [37] or [38], respectively.

So then, two possible sources were feasible in the generation of this avalanche. The presence of the geodynamic framework of Oaxaca with the occurrence of earthquakes between 7 and 8 Mw could suggest that a comparable event could have generated the studied avalanche. On the other hand, if we consider also the morphological evidence of the Calaveras fault, an earthquake between 6 and 7 Mw could have easily generated an avalanche of this type if the fault was active in the period of the landslide event. Both scenarios are plausible, but now the most important thing is to see the possibility of starting new geoarchaeological explorations and

consider that these segments of the Oaxaca fault system are active.

8. Conclusions

This research indicates that the Mitla Landslide is a collapsed body formed of ignimbrite blocks and matrix from the Sierra La Calavera. According to its morphology, the geotechnical characteristics, and the geophysical data interpretation, the landslide was provoked by an earthquake of a magnitude in the range from 6.2 to 7.3 Mw. The observations on the field suggest that the earthquake could have been caused by the La Calavera fault, which is a normal fault with small left component and is part of the Oaxaca fault system-oriented NNW-SSE to N-S. But we also do not rule out that this avalanche was instead generated by the frequent seismic activity of the Cocos plate. These geological facts (from regional to local tectonics), and the age of the landslide, could introduce a new scenario regarding seismic hazard in Oaxaca, because beside the intense seismic activity caused by the Cocos plate, more shallow earthquakes could also occur. On the other hand, the fact that the Mitla fault (Calaveras) is currently active indicates that many of the fault segments are favorably oriented to the current stress field.

There is no precise age established for the landslide occurrence; however, the event presumably damaged the pyramids of Mitla, and a large part of the pyramids are probably located under the avalanche deposit as evidenced by the outcomes of this preliminary investigation. Considering that if the population reached 10,000 individuals, the extension must have been larger than what can be implied by the current remains.

From the point of view of geophysical exploration, the method of electrical tomography and the study of earthquakes and environmental noise were good and promising tools in the Geoarchaeology field of research, even if the procedure can be better calibrated in synergy with other survey techniques. It was not the case of the use of Georadar that it failed to provide great information in the high-detail characterization of the local subsoil and materials discrimination in depth as necessary for this type of research. For future work it is recommended to make a thinner network with electrical tomography in parallel with seismic profiles.

Data Availability

All the geological and geophysical data have been generated by the authors of this work.

Conflicts of Interest

The authors declare that they have no conflicts of interest.

Acknowledgments

Funding to support this work came from the SEP-CONACYT-CB-5222009-01-134151 project entitled "Tectonic, Paleoseismologic and Archeoseismologic study in Holocene to recent lakes of the Trans-Mexican Volcanic

Belt and the Jalisco block". We wish to thank all who were involved in the Cemie-Geo P-17 project for contributing to the results of this study during the course on Geophysics Methods. We are also grateful to the local government and the community of San Pablo Villa de Mitla for all the help provided. All the information relating to historical earthquakes in the Oaxaca state was provided by the SSN, whose personnel carried out also the seismic stations arrangement, maintenance, and data acquisition.

References

- [1] A. M. Michetti, E. Esposito, L. Guerrieri et al., "Environmental seismic intensity scale-ESI 2007" *Memorie Descrittive Della Carta Geologica D'Italia*, vol. 74, no. 41, 2007.
- [2] A. N. Mahgoub, N. Reyes-Guzmán, H. Böhnelt, C. Siebe, G. Pereira, and A. Dorison, "Paleomagnetic constraints on the ages of the holocene malpaís de zacapu lava flow eruptions, michoacán (México): implications for archeology and volcanic hazards," *The Holocene*, vol. 28, no. 2, pp. 229–245, 2018.
- [3] M. León Portilla, *La Visión De Los Vencidos, Relaciones Indígenas De La Conquista*, UNAM, 1959.
- [4] V. H. Garduño-Monroy, J. L. Macías, A. Oliveros, and V. M. Hernández-Madriz, "Progress in seismic and archeoseismic studies in the zone of mitla, oaxaca," in *Proceedings of the 3rd INQUA-IGCP-567 International Workshop on Active Tectonics, Paleoseismology and Archaeoseismology*, Morelia, México, 2012.
- [5] F. R. Zúñiga, G. Suárez, Á. Figueroa-Soto, and A. Mendoza, "A first-order seismotectonic regionalization of Mexico for seismic hazard and risk estimation," *Journal of Seismology*, vol. 21, no. 6, pp. 1295–1322, 2017.
- [6] D. Melgar, A. Ruiz-Angulo, E. S. García et al., "Deep embrittlement and complete rupture of the lithosphere during the M w 8.2 Tehuantepec earthquake," *Nature Geoscience*, vol. 1, 2018.
- [7] C. M. Valdes, W. D. Mooney, S. K. Singh et al., "Crustal structure of oaxaca, mexico, from seismic refraction measurements," *Bulletin of the Seismological Society of America*, vol. 76, no. 2, pp. 547–563, 1986.
- [8] M. Spranger, *GEOLIMEX: Eine erste Geotraverse durch Süd-mexiko; Auswertung des refraktions seismischen Profils [Ph.D. thesis]*, Christian-Albrechts University, Kiel, Germany, 1994.
- [9] H. Jödicke, A. Jording, L. Ferrari, J. Arzate, K. Mezger, and L. Rüpk, "Fluid release from the subducted Cocos plate and partial melting of the crust deduced from magnetotelluric studies in southern mexico: implications for the generation of volcanism and subduction dynamics," *Journal of Geophysical Research: Solid Earth*, vol. 111, no. 8, Article ID B08102, pp. 1–22, 2006.
- [10] A. Jording, L. Ferrari, J. Arzate, and H. Jödicke, "Crustal variations and terrane boundaries in Southern Mexicoas imaged by magnetotelluric transfer functions," *Tectonophysics*, vol. 327, no. 1–2, pp. 1–13, 2000.
- [11] F. Corbo, *Estudio de la subducción y su relación con la presencia de fluidos a partir de sondeos magnetotéluricos en el Bloque de Jalisco y Oaxaca [Ph.D. thesis]*, Centro de Geociencias, Universidad Nacional Autónoma de México, México City, México, 2013.
- [12] J. O. Campos-Enriquez, F. Corbo-Camargo, J. Arzate-Flores et al., "The buried southern continuation of the Oaxaca-Juarez terrane boundary and Oaxaca Fault, southern mexico:

- magnetotelluric constraints,” *Journal of South American Earth Sciences*, vol. 43, pp. 62–73, 2013.
- [13] J. A. Arzate-Flores, R. Molina-Garza, F. Corbo-Camargo, and V. Márquez-Ramírez, “Low angle contact between the Oaxaca and Juárez terranes deduced from magnetotelluric data,” in *Geodynamics of the Latin American Pacific Margin*, vol. 173, pp. 3357–3371, Birkhäuser, Cham, Switzerland, 2016.
 - [14] N. León, *Lyobaa o Mictlan*, Delegación Mexicana, México, 1901.
 - [15] I. Ferrusquía-Villafranca, J. A. Denison, R. E. Wilson, F. W. McDowell, and J. Solorio-Munguía, “Tres edades radiométricas oligocénicas y miocénicas de rocas volcánicas de las regiones de la mixteca alta y valle de Oaxaca, estado de Oaxaca,” *Boletín de la Asociación Mexicana de Geólogos Petroleros*, vol. 26, pp. 249–262, 1974.
 - [16] D. M. McCann and A. Foster, “Reconnaissance geophysical methods in landslide investigation,” *Engineering Geology*, vol. 29, pp. 59–78, 1990.
 - [17] M. Nogoshi and T. Igarashi, “On the propagation characteristics of microtremors,” *Seismological Society of Japan*, vol. 23, pp. 264–280, 1970.
 - [18] Y. Nakamura, “Method for dynamic characteristics estimation of subsurface using microtremor on the ground surface,” *Quarterly Report of RTRI (Railway Technical Research Institute) (Japan)*, vol. 30, no. 1, pp. 25–33, 1989.
 - [19] H. Okada, *The Microtremor Survey Method*, Society of Exploration Geophysics, Tulsa, Okla, USA, 2003.
 - [20] H. Arai and K. Tokimatsu, “S-wave velocity profiling by inversion of microtremor H/V spectrum,” *Bulletin of the Seismological Society of America*, vol. 94, no. 1, pp. 53–63, 2004.
 - [21] P. Y. Bard, “Microtremor measurements: a tool for site effect estimation,” in *Proceedings of the Second International Symposium on the Effects of Surface Geology on Seismic Motion*, vol. 3, pp. 1251–1279, AA Balkema, 1998.
 - [22] A. Clemente-Chavez, F. R. Zúñiga, J. Lermo et al., “On the behavior of site effects in central Mexico (the Mexican volcanic belt - MVB), based on records of shallow earthquakes that occurred in the zone between 1998 and 2011,” *Natural Hazards and Earth System Sciences*, vol. 14, no. 6, pp. 1391–1406, 2014.
 - [23] SESAME WP05, “Site effects assessment using ambient excitations. Optimum deployment strategy for array measurements,” European Commission - Research General Directorate EVG1 CT 2000-00026 SESAME, SESAME European research project WP05- Deliverable D07.05, Geopsy was developed by Laboratoire de Géophysique Interne et Tectonophysique (LGIT) Grenoble, France and University of Potsdam, Germany, 2002.
 - [24] M. Wathelet, *Array recordings of ambient vibrations: surface wave inversion [Ph.D. thesis]*, Liege University, 2005.
 - [25] K. Konno and T. Ohmachi, “Ground-motion characteristics estimated from spectral ratio between horizontal and vertical components of microtremor,” *Bulletin of the Seismological Society of America*, vol. 88, no. 1, pp. 228–241, 1998.
 - [26] O. Kulháněk, *Introduction to digital filtering in Geophysics*, Elsevier Scientific Publishing Company, The Netherlands, 1976.
 - [27] K. Aki, “Space and time spectra of stationary stochastic waves, with special reference to microtremors,” in *Bulletin of the Earthquake Research Institute*, vol. 35, pp. 415–456, Tokyo University, 1957.
 - [28] H. Flores-Estrella and J. Aguirre-González, “SPAC: an alternative method to estimate earthquake site effects in Mexico city,” *Geofísica Internacional*, vol. 42, no. 2, pp. 227–236, 2003.
 - [29] J. Aguirre González, M. Rodríguez González, and R. Vázquez Rosas, *Memorias del XXIII Congreso Nacional de Mecánica de Suelos, Tuxtla Gutiérrez, Chiapas*, 2006.
 - [30] R. D. Barker, “Electrical imaging and its application in engineering investigations,” in *Modern Geophysics in Engineering Geology*, D. M. McCann, M. Eddleston, P. J. Fenning, and G. M. Reeves, Eds., vol. 12, pp. 37–43, Geological Society, 1997.
 - [31] D. Griffiths and J. Turnbull, “A multi-electrode array for resistivity surveying,” *First Break*, vol. 3, no. 7, pp. 16–20, 1985.
 - [32] P. Stummer, H. Maurer, H. Horstmeyer, and A. G. Green, “Optimization of dc resistivity data acquisition: Real-time experimental design and a new multielectrode system,” *IEEE Transactions on Geoscience and Remote Sensing*, vol. 40, no. 12, pp. 2727–2735, 2002.
 - [33] K. Hsu, “On sturzstroms—catastrophic debris streams generated by rockfalls,” *Geological Society of America Bulletin*, vol. 86, no. 1, pp. 129–140, 1975.
 - [34] BSSC Program on Improved Seismic Safety Provisions, *NEHRP Recommended Provisions for Seismic Regulations for New Buildings and Other Structures*, FEMA, 1998.
 - [35] D. K. Keefer, “Landslides caused by earthquakes,” *Geological Society of America Bulletin*, vol. 95, no. 4, pp. 406–421, 1984.
 - [36] C. E. Rodríguez, J. J. Bommer, and R. J. Chandler, “Earthquake-induced landslides: 1980-1997,” *Soil Dynamics and Earthquake Engineering*, vol. 18, no. 5, pp. 325–346, 1999.
 - [37] S. G. Wesnousky, “Displacement and geometrical characteristics of earthquake surface ruptures: Issues and implications for seismic-hazard analysis and the process of earthquake rupture,” *Bulletin of the Seismological Society of America*, vol. 98, no. 4, pp. 1609–1632, 2008.
 - [38] D. L. Wells and K. J. Coppersmith, “New empirical relationships among magnitude, rupture length, rupture width, rupture area, and surface displacement,” *Bulletin - Seismological Society of America*, vol. 84, no. 4, pp. 974–1002, 1994.

Research Article

HVSR Analysis of Rockslide Seismic Signals to Assess the Subsoil Conditions and the Site Seismic Response

Alessia Lotti,¹ Veronica Pazzi ,¹ Gilberto Saccorotti,² Andrea Fiaschi,³
Luca Matassoni,³ and Giovanni Gigli¹

¹Department of Earth Sciences, University of Firenze, Via G. La Pira 4, 50121 Firenze, Italy

²National Institute of Geophysics and Volcanology, Via della Faggiola 32, Pisa, Italy

³Fondazione Parsec, Via di Galceti 74, Prato, Italy

Correspondence should be addressed to Veronica Pazzi; veronica.pazzi@unifi.it

Received 30 May 2018; Revised 14 September 2018; Accepted 1 October 2018; Published 1 November 2018

Academic Editor: Filippos Vallianatos

Copyright © 2018 Alessia Lotti et al. This is an open access article distributed under the Creative Commons Attribution License, which permits unrestricted use, distribution, and reproduction in any medium, provided the original work is properly cited.

Many Italian rock slopes are characterized by unstable rock masses that cause constant rock falls and rockslides. To effectively mitigate their catastrophic consequence thorough studies are required. Four velocimeters have been placed in the Torgiovannetto quarry area for an extensive seismic noise investigation. The study area (with an approximate surface of 200×100 m) is located near the town of Assisi (Italy) and is threatened by a rockslide. In this work, we present the results of the preliminary horizontal to vertical spectral ratio analysis of the acquired passive seismic data aimed at understanding the pattern of the seismic noise variation in case of stress state and/or weathering conditions (fluid content and microfracturing). The Torgiovannetto unstable slope has been monitored since 2003 by Alta Scuola of Perugia and the Department of Earth Sciences of the University of Firenze, after the observation of a first movement by the State Forestry Corps. The available data allowed an extensive comparison between seismic signals, displacement, and meteorological information. The measured displacements are well correlated with the precipitation trend, but unfortunately no resemblance with the seismic data was observed. However, a significant correlation between temperature data and the horizontal to vertical spectral ratio trend of the seismic noise could be identified. This can be related to the indirect effect of temperature on rock mass conditions and further extensive studies (also in the time frequency domain) are required to better comprehend this dependency. Finally, the continuous on-line data reveal interesting applications to provide near-real time warning systems for emerging potentially disastrous rockslides.

1. Introduction

For many years, researchers have turned their attention to the massive problem of landslides in Italy. The topic is high on the agenda because roughly 70% of all the landslides in the European continent are concentrated in Italy [1]. As a consequence of steep slopes, high seismic activity, and soil and bedrock properties, many hillsides of the Italian valleys are characterized by unstable rock masses causing constant rock falls and rockslides of various sizes and types [2]. A thorough understanding of failure types, mechanisms, and possible causes of landslides is required to effectively mitigate their catastrophic consequences. Moreover, currently early warning systems (EWS) can be implemented in order to

prevent loss of life and to reduce the economic and material impact of landslide events [3, 4]. Nevertheless, frequently enough, it is not easy to find a technique able to provide an immediate alert [5]. Therefore, slope failure of rock masses represents an interesting case study for verifying the feasibility of using passive seismic monitoring in EWS. By means of the observation of the changes which occurred in the acquired signal, in fact, it could be possible to detect variations in the elastic parameters of the rock body related to changes in pore-fluid pressure, consolidation, and microfracturing that could forecast failure [6].

In the last years, besides the traditional geotechnical and structural monitoring (e.g., topographic total stations, extensometers, and inclinometers, [7]), new techniques have

been used to characterize and monitor landslides: aerial photos and LiDAR [8, 9], GPS monitoring [10–12], InSAR and GB-InSAR technique [3, 13–15], laser scanner [16, 17], infrared thermography [18–20], and optic fiber strain sensors [21]. Shallow geophysical methods represent a valid complement to the aforementioned techniques [6, 22–27].

To verify the performance of a small-scale seismic network as part of an EWS, a pilot scale experiment was arranged to monitor an unstable rock mass. The test site is the Torgiovanetto quarry located in Umbria Region, one of the Italian Regions that is more prone to landslide. In general, quarries can be characterized as remarkably vulnerable areas, since their natural geomorphology is altered by excavating activities [28]. The data were collected during a 7-month-period monitoring. In this paper we present the results of the preliminary analysis carried out on the acquired data by means of the horizontal to vertical spectral ratio analysis (HVSr or H/V). These analyses were aimed at understanding the pattern of seismic noise variation in case of stress state and/or weathering conditions (fluid content and microfracturing) as the first step to set up a reliable EWS. The studied quarry rockslide was also extensively monitored since 2003 with traditional methods. Therefore, the multiparameter analysis was useful to understand the mechanisms that control the rockslide dynamics and to evaluate possible connection between rainfall/temperature/displacement and rockslide seismic activity. Thus, a comparison between the seismic data and both temperature and precipitation data is discussed, in order to highlight a correlation between them.

2. The Study Area

The Torgiovanetto test site is located in a micritic limestone former quarry (dismissed since the late '90s), 2 km NE from Assisi (Umbria Region in Central Italy) in the northward facing slope of Mount Subasio (red square in Figure 1). Landslides in Umbria occupy about 14% of the entire land cover (8456 km²) and affect many urban areas.

Mount Subasio (1109 m a.s.l.) is part of the Umbria-Marche Apennines, a complex fold and arcuate thrust belt that occupies the outer zones of the Northern Apennines of Italy. The belt developed during the Neogene as a result of the Ligurian Ocean closure, followed by the continental collision between the European Corsica-Sardinia Margin and the African Adria Promontory [29]. A northeast-directed compressional tectonic phase started during the middle Miocene and is still active near the Adriatic coast [30]. During the upper Pliocene an extensional phase started with a principal stress oriented about NE-SW that resulted in the dissection of the Umbria-Marche Apennines and the opening of a NW-SE-trending set of continental basins. Mount Subasio area consists in a SSE-NNW trending anticline [31, 32] with layers dipping almost vertically in the NE side of the mountain with several NW-SE striking normal faults on the eastern and western flanks. The local geological formations, belonging to the Umbro-Marchigiana Sequence (from Calcare Massiccio to Marnoso Arenacea), represent the progressive sinking of a marine environment.

The study area consists mainly of micritic limestone belonging to the Maiolica Formation (Upper Jurassic-Lower Cretaceous) that widely outcrops in the area. The thickness of the Formation is about 100 m and is composed by white or light grey well-stratified micritic limestone layers, whose thickness ranges between 10 cm and 1 m, and thin clay interlayers may sporadically occur. The site is also partially covered by very heterometric debris (from pebble- to cobble-sized angular clasts, with scattered boulders, in a silty or coarse grained sandy matrix), some of which are of anthropogenic nature. The dip direction varies between 350° and 5°, while the dip of layers from 25° to 35°, which means that, in general, the layers' dip is in the same direction of the slope but with a gentler angle.

First deformations within the quarry site were observed in May 2003 by the State Forestry Corps, in the form of tension cracks in the vegetated area above and within the quarry front. From then, several monitoring campaigns were carried out by means of different techniques (topographic total station, inclinometers, extensometers, ground-based interferometric radar, laser scanner, and infrared thermal camera [7]). It is assured that the main predisposing factor of instability was the quarrying activity that heavily altered the original front. Actually the quarry is structured in four main terraces, that the dense vegetation prevents distinguish well them (refer to [4] for the quarry view from north to south), with an overall height of about 140 m (Figure 2). Nevertheless, earthquakes-induced landslides cannot be neglected among the instability factors. In fact, the link between earthquake and landslide is well documented in the literature, especially in the cases of high-magnitude seismic event [33–36]. For example, the seismic sequence that affected the area southeast of the quarry (Colfiorito basin) in the 1997-98 reached the Assisi area in a macroseismic intensity (MCS) $I_0 = 8-9$ [37]. Therefore, the seismicity of the area surrounding the quarry is another important instability factor.

The main rockslide [38] in the Torgiovanetto quarry has a rough trapezoidal shape and covers about 200 m x 100 m in surface and 550 m a.s.l. and 680 m a.s.l. in altitude. The geometry and other soil parameters (such as densities and body wave velocities) are well known thanks to the geotechnical and geophysical investigations carried out on the site by Alta Scuola of Perugia and by the University of Firenze [4, 7]. Among these investigations, a passive seismic network in continuous recording was installed on this rockslide from December 2012 to July 2013. The "traditional" monitoring network was composed by 13 wire extensometers, 1 accelerometer, 1 meteorological station (composed of 1 thermometer and 1 rain gauge), and 3 inclinometers (Figure 2). The monitoring network, progressively enhanced and improved throughout the years, was completed with hydrological data [39], modelling computation analysis [7, 40], and the seismological stations. Nowadays, the active volume of Torgiovanetto rockslide is estimated to be about 182,000 m³. The upper boundary is defined by a big open subvertical fracture (Figure 2), a tension crack with an EW strike, which in some places displays a width up to 2 m and depth of about 20 meters [40].

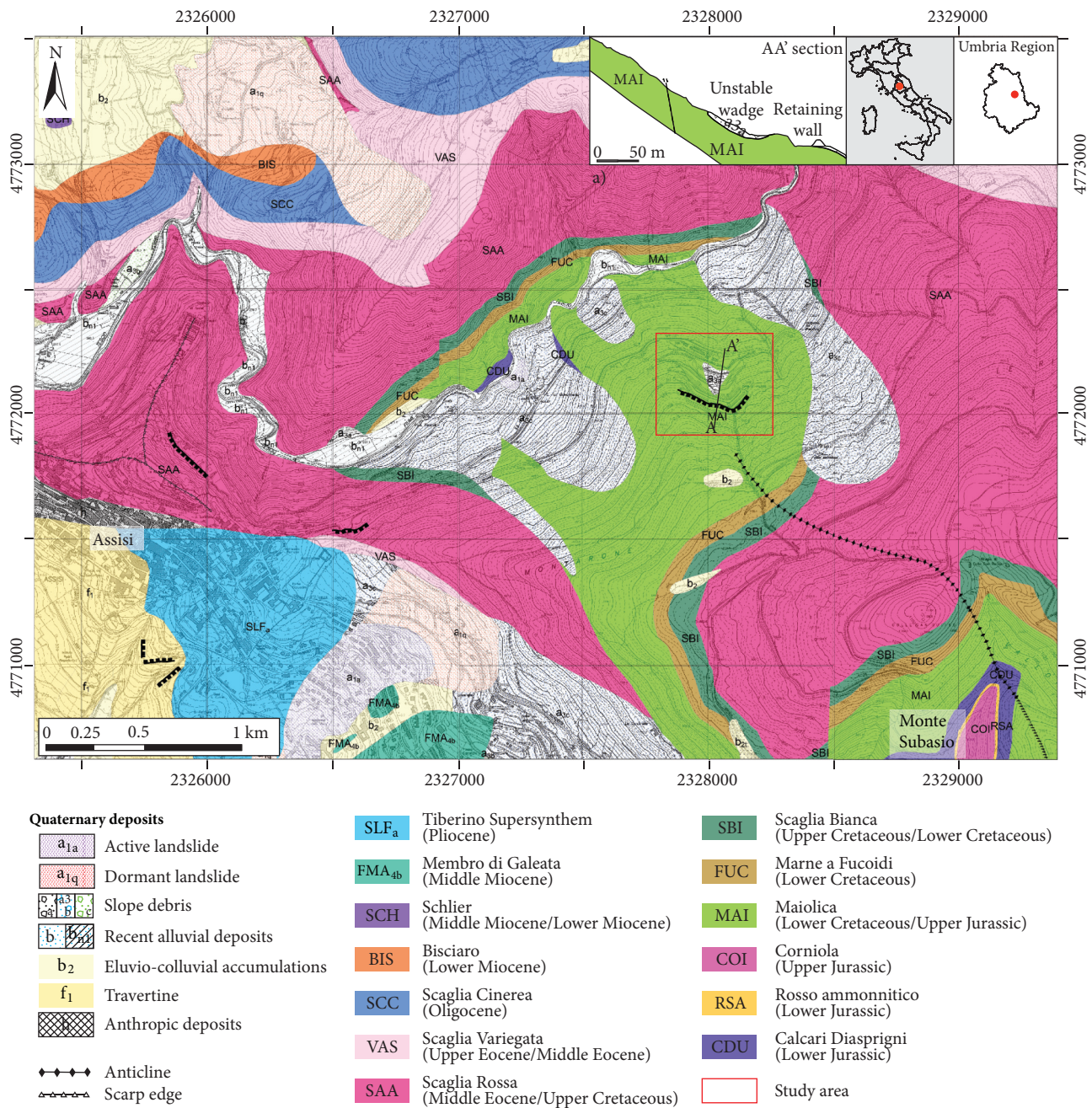


FIGURE 1: Geological map of the study area. (a) Geological cross-section of the investigated slope (modified from Balducci et al., 2011).

3. Methods

The HVSR technique was introduced for the first time by [41, 42]. It is based on the ratio between the horizontal and vertical components of ground motion and it requires a 3-component sensor to acquire data. According to [43] microtremor energy consists mainly of SH waves, while, according to other authors, as discussed in [44], H/V peaks are related to Rayleigh waves. One of the striking features of the HVSR ratio is its stability in time, documented in many papers [27, 45, 46]. The HVSR curve allows gaining additional

information about the underlying velocity profile at the site, especially when a strong different shear wave velocity exists between the shallow layer and the bedrock [47, 48]. The site effect amplification, in fact, could be caused by several geological conditions and one of them is the presence of a soft soil layer overlying a rigid half space. Nowadays, the HVSR is widely used both for environmental [49, 50] and for structural [51–53] problems. For a more detailed discussion about the seismic noise method please refer to the wide literature [27, 43, 54–56]. The main application of HVSR technique on landslide concerns the possibility to reconstruct

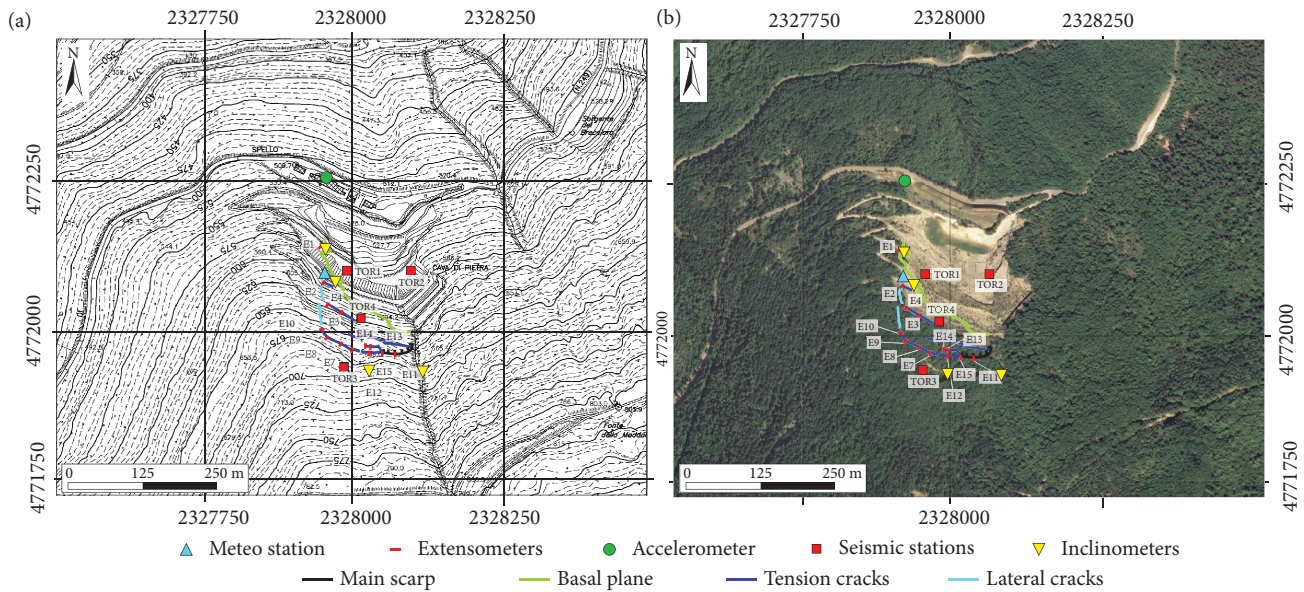


FIGURE 2: (a) Regional Topographic Map and (b) satellite view of the “traditional” monitoring network and the passive seismic array installed to monitor the Torgiovannetto quarry. Red squares represent the seismic stations, the light blue triangle represents the meteorological station, red lines represent the extensometers, and yellow triangles represent the inclinometers. The main scarp (black line), the basal plane (green line), and the tension and lateral cracks (dark blue and light blue, respectively) were detected by [4].

the geometry of the sliding mass and to detect the depth of the shear surface [27, 57–59] with a good approximation. This point is beyond the scope of this paper that, instead, aimed at the evaluation of the dynamic behaviour of the rock mass affected by the presence of fractures linked to the sliding wedge, searching for changes in its internal characteristics detectable by the HVSR shape [6, 23] that could be used in early-warning procedure.

At the Torgiovannetto quarry, seismic measurements were performed using a small-scale network composed by four seismic stations (TOR1, TOR2, TOR3, and TOR4; locations are shown in Figure 2). Due to the geomorphological characteristics of the site and the lack of access to the eastern part of the slope, the installation was really challenging. Station TOR4 was located on the sliding mass while the other three stations (TOR1, TOR2, and TOR3) were located at the edge of the quarry arranged in pairs with diametrically opposite position with respect to the centre of the landslide. This configuration (a reverse Y with respect to the sliding orientation) allowed us to retrieve punctual information both inside and outside the landslide. Each station with a SARA 24bit A/D converter (SL06) coupled with a SS45 tri-axial velocimeter sensor with a natural frequency of 4.5 Hz and transduction factor of 78 V/m/s. Instruments response is flat down to 2 Hz, with an upper-corner frequency of 100 Hz. All of them were equipped with Global Positioning System (GPS) receivers for time synchronization. The sensors were placed on a concrete base with supporting plinth, isolated from the exterior in order to attain protection from severe weather conditions. Battery supply and digitizer, connected to the sensors through a connector cable, were housed in a separate case. Data were recorded in continuous mode at

200 Hz sampling frequency, as the best compromise between signal resolution and data storage. Data acquisition was continuous for 210 days from December 7, 2012, to July 3, 2013, except for some short intervals due to the batteries change. Data format of the seismic records retrieved from the converters SL06 is miniSEED (‘Data-only’ volume; <http://ds.iris.edu/ds/nodes/dmc/data/formats/miniseed/>). Nevertheless, this format was mainly designed for the exchange of geophysical data and not for analysis. Therefore, first of all, recorded data were converted into a more suitable format for elaborations like SAC (Seismological Analysis Code; <https://ds.iris.edu/files/sac-manual/manual/file-format.html>). For each station, every 6 hours, three separate files were generated (Figure 3), which correspond to the east-west (SHE), north-south (SHN), and vertical or up-down (SHZ) components of ground velocity. The amplitude (y-axis) was expressed in counts, while the x-axis in time (hours).

Data analysis was performed by means of Geopsy software (www.geopsy.org; cf. [53] as an example of application). For all the 3 components of ground motion the acquired data were detrended, mean-removed, and filtered. Then, each trace was divided into windows of 120 s length, and each window was tapered with a Tukey window and padded with zeros. The amplitude spectrum was evaluated via the Fast Fourier Transform (FFT); individual spectra were finally smoothed using a boxcar of 0.1 Hz width. The H/V ratio was calculated for each window, and the final HVSR function was given by the average of the HVSRs over 6 h intervals. In this work the horizontal (H) spectra have been computed by averaging E-W and N-S components using a quadratic mean, which shows a lower bias with respect to the simple arithmetic mean [52]. Finally, a special filtering process was

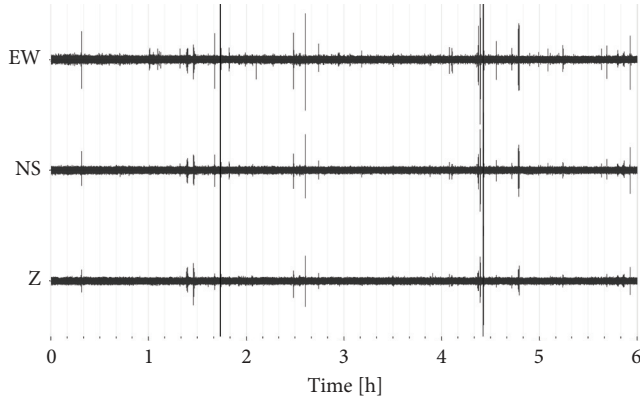


FIGURE 3: Example of a 6 h trace recorded during the monitoring period at TOR1 showing vibrations in three components (EW, NS, and vertical Z.)

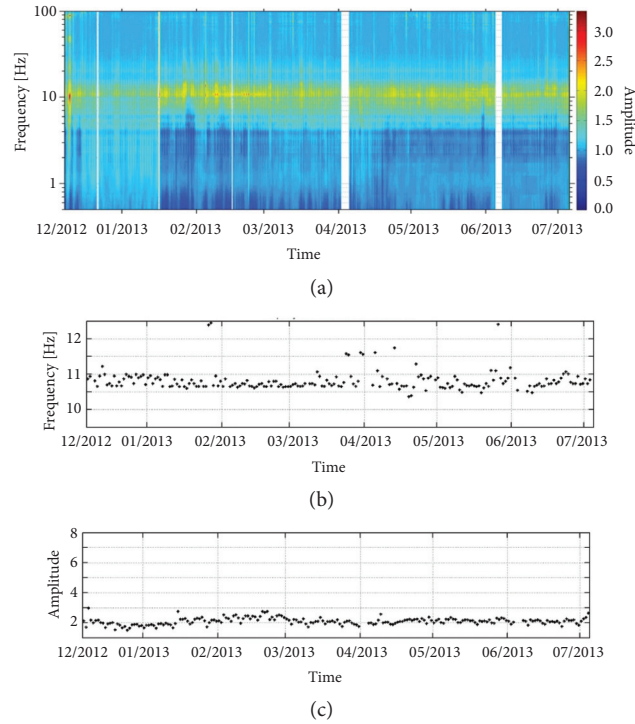


FIGURE 4: (a) The TOR1 HVSR amplitude, (b) the peak frequency distribution, and (c) the peak amplitude distribution over the whole monitoring period.

not applied since it did not significantly affect nonstationary noises as happened in other studies [60–62].

4. Results

The resonance frequency peaks, determined using the H/V method described above, were analysed for stations TOR1, TOR3, and TOR4 throughout the whole monitored period. The HVSR analysis of station TOR2 is not presented here because of the typical flat shape of the outcropping seismic bedrock [55]. The TOR1 HVSR (Figure 4) exhibits the highest

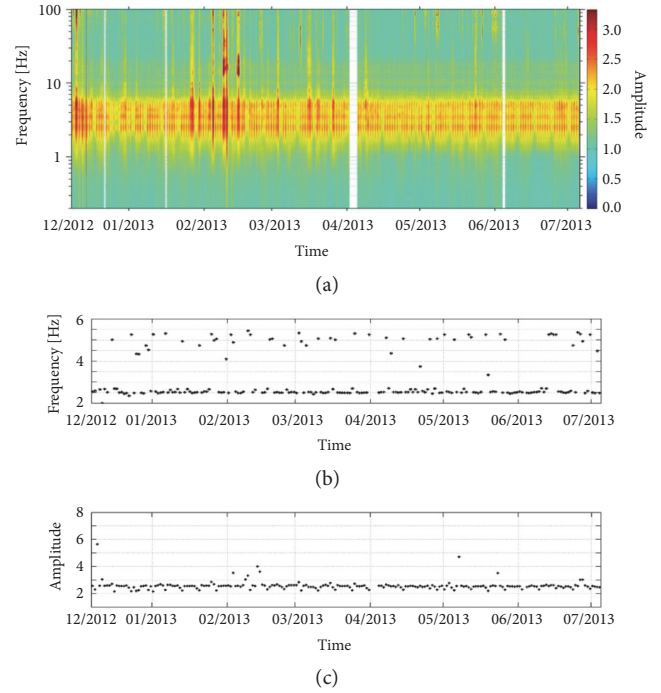


FIGURE 5: (a) The TOR3 HVSR amplitude, (b) the peak frequency distribution, and (c) the peak amplitude distribution over the whole monitoring period.

amplitudes over the frequency band of 4.5 Hz to 13 Hz with a stable peak around 10.5 Hz whose amplitude is generally slightly above 2. Throughout the observation period, both, peak amplitude and frequency, did not exhibit any particular trend, with the exception of a slight increase in amplitude within the period of January to mid-March, 2013. The TOR3 HVSR (Figure 5) is characterized by more closely spaced peaks of amplitude higher than 2, coalescent in the spectral band spanning from 2.5 to 6 Hz. Two main peaks are present: one, more frequent at 2.5 Hz and the other at 5 Hz. This behaviour suggesting that the medium properties are likely subjected to slight, periodic variations potentially related to temporary fluctuation in water content that influences the propagation velocity.

At TOR4 (Figure 6) the HVSR exhibits two main peaks at frequencies of roughly 2.7 Hz and 5.5 Hz. The amplitude of these peaks varies according to a characteristic and systematic daily, and therefore weekly, behaviour, in which the largest amplitudes of noise are higher. This could be associated with (a) an artefact related to the internal electronic noise of the instrument, whose effects become relevant when the ground vibrations have very low amplitude, such as night time or during the weekend, or (b) the variations of the noise wavefield, as a consequence of the activation of different sources related to anthropogenic activities. Beginning in April, 2013, the amplitudes of these peaks start increasing from the values of 3, and by the end of the monitoring period they attain values around 5, that is, about 65% greater than those observed during the early phases of the experiment. Such amplitude increase is likely to reflect a corresponding

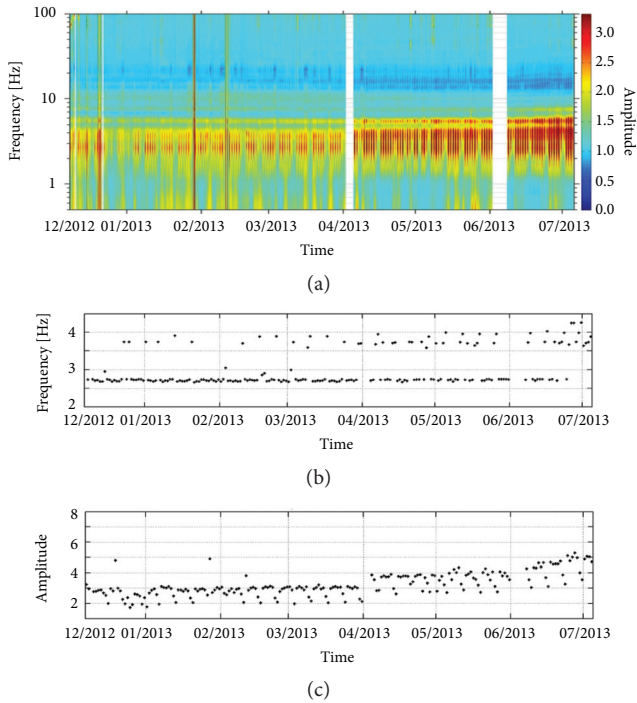


FIGURE 6: Near here: (a) The TOR4 HVSR amplitude, (b) the peak frequency distribution, and (c) the peak amplitude distribution over the whole monitoring period.

increase of the impedance contrast between the unstable mass and the underlying solid bedrock. However, the peak frequency remains stable in time, indicating that both thickness and velocity of the shallowest layer remain substantially unchanged. Thus, an increment in the velocity and/or density of the underlying layer must be invoked in order to explain the inferred impedance variations. Potential phenomena provoking this possible velocity increase will be discussed in the following.

Also, the HVSR directivity throughout the 7 months of recording was analysed. As an example, contour maps in Figures 7(a) and 7(b) compare the medium directionality of data acquired in December 2012 and July 2013, respectively. For the two different intervals, the directivity at stations TOR1, TOR2, and TOR3 stayed substantially unchanged. On the other hand, the TOR4 polarization direction between the two periods change slightly (Figure 8), even though for the later interval directivity is clearer as a consequence of the amplitude increase of the horizontal components, as also manifested by the growing number of the HVSR peaks (Figure 6). This suggests that the observed temporal variations in the HVSR plots are not due to changes in the distribution of active sources; if this would be the case, consequently the polarization direction should most likely have changed.

5. Discussion

Assuming that the HVSR is strictly related to the dynamic properties of the medium and that it is supposed to be stable

if no change occurred in the velocity and/or density of the ground [63], results from HVSR analyses can be summarized as follows: (i) there are clear configurations of quasicontant or slowly varying contiguous frequencies whose H/V peak values depend on the considered station; (ii) the stations located on the sliding mass (TOR4) and at its head (TOR3), on potentially loose section, show an amplitude peak which is sharper and larger than those observed at the stations settled downstream. At TOR4, the amplitude variations of the HVSR cannot be unequivocally interpreted. However, the overall stationarity of the polarization properties suggests that those changes most likely reflect a variation in the acoustic properties of the medium rather than a change in the distribution of noise sources.

As mentioned in the Introduction section the quarry rockslide was extensively monitored since 2003 with traditional methods. Among these, as shown in Figure 2, there were 13 extensometers. All the extensometer data (E1-E15 in Figure 2) were individually normalized and compared with the measured cumulative rainfall in order to highlight a possible linear correlation between two different time series. The *corr* function in MATLAB was employed to both evaluate the linear (or rank) correlation (ρ) and perform a hypothesis test. The hypothesis was of no correlation against the alternative that there is a nonzero correlation (P_{val}) assuming by the authors that the correlation between two data is significant if P_{val} is sufficiently small (< 0.05). Table 1 shows the values obtained for each comparison.

The results of the correlation analysis clearly show that the deformational fields in the upper section of the quarry (E7, E8, E9, E10, E13, E14, located on the main cracks whose widths enlarge up to 2 m from East to West) and in the western part of the quarry (E2, located on the lateral crack) are strictly related to the seasonal rainfall, since the P_{val} values are very small (exponent lower than -100). This behaviour could be explained taking into account that, at sites where opening of the fractures is significant, pore water pressures in the fractures/cracks can critically influence the stability of rock. Unfortunately, because of a problem in the instrumentation, no data are available on the water level in the cracks. Moreover, from a qualitatively point of view, looking at Figure 9, it is possible to assess that periods characterized by the main soil movements (highlighted by the vertical sections of the extensometer curves) follow periods with higher rainfall (highlighted by the vertical sections of the cumulated rain curve). In particular, this behaviour is clear at the half of January, and at the end of February and May. The rainfall also seems to have a weaker but still significant influence on the deformations measured by E11, E3, E4, and E15 (Figure 9) while an inverse correlation exists with the data recorded by E1 (located in correspondence of the basal plane). Finally, there is no evidence of correlation for E12 data neither with the rain trend nor with the temperature variation. Unfortunately, there are no superficial evidences that could justify this behaviour, apart from the fact that E12 is located in correspondence of a junction between two main fractures (Figure 2). Perhaps its behaviour is caused by this junction (i.e., the highest movements are recorded by the

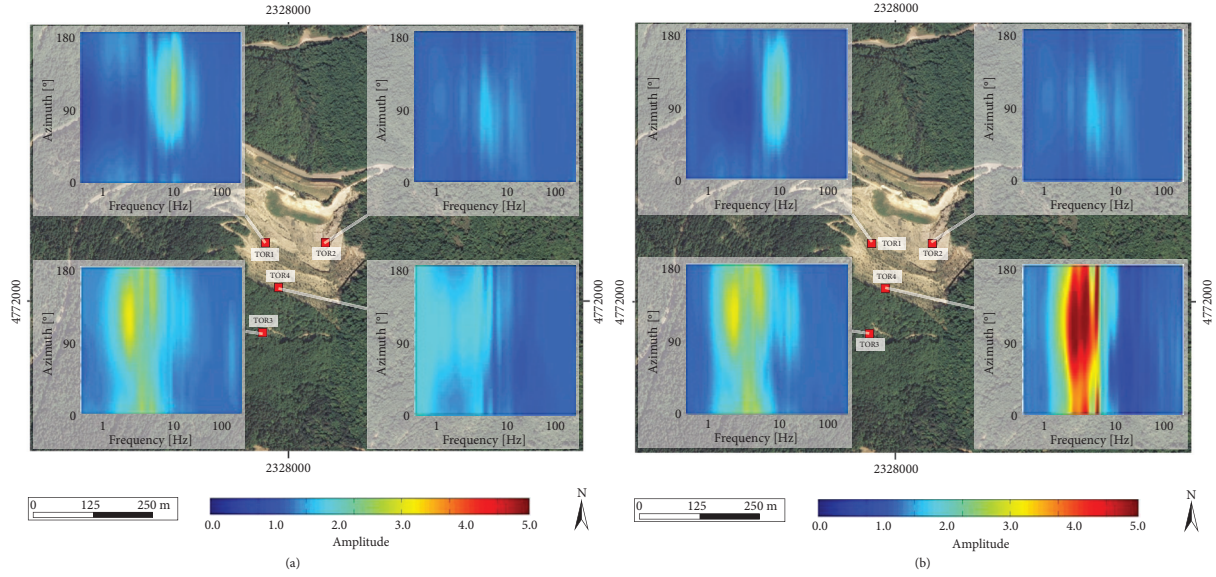


FIGURE 7: The HVSR directivity in (a) December 2012 and (b) July 2013.

TABLE 1: Correlation test between cumulative rainfall and extensometer data (Cum.RAIN – Ei, where i=1, 2...15), and temperature and E12 extensometer data (Temp – E12).

Correlation test	Rho	Pval	Correlation test	Rho	Pval
Cum.RAIN – E1	-0.8674	9.1381×10^{-64}	Cum.RAIN – E10	0.9724	5.5739×10^{-131}
Cum.RAIN – E2	0.9822	4.0970×10^{-150}	Cum.RAIN – E11	0.8782	2.9209×10^{-67}
Cum.RAIN – E3	0.8326	6.7328×10^{-51}	Cum.RAIN – E12	0.1336	5.5500×10^{-2}
Cum.RAIN – E4	0.8296	1.6040×10^{-53}	Cum.RAIN – E13	0.9860	1.1666×10^{-67}
Cum.RAIN – E7	0.9746	1.7970×10^{-134}	Cum.RAIN – E14	0.9845	2.7311×10^{-156}
Cum.RAIN – E8	0.9826	3.7711×10^{-151}	Cum.RAIN – E15	0.9633	1.5301×10^{-118}
Cum.RAIN – E9	0.9833	7.4087×10^{-153}	Temp – E12	0.1564	3.1200×10^{-2}

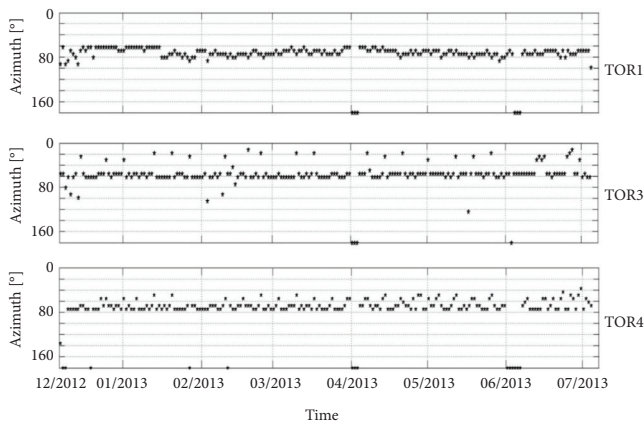


FIGURE 8: The peak azimuth distribution at TOR1, TOR3, and TOR4 over the whole monitoring period.

extensometer around), or otherwise it could be possible that some errors in the data registration occurred.

A good match (Rho: 0.7147; Pval 9.3923×10^{-30}) is obtained by comparing the TOR4 HVSR amplification value and

temperature variation (Figure 10). This could be caused by the water content variation in the medium (water content alternatively empties and fills the rock pores) and consequently the relative V_R variation, related to changes in the HVSR amplification value. The saturation of pores with water, in fact, tends to increase the velocity of P-waves (which propagate more efficiently through water than air), also increasing the Poisson ratio. This has a strong influence on the Rayleigh waves and, in particular, on the ellipticity of the particle motion with a consequent increase of the ratio between the horizontal component H and the vertical one V of ground motion [64–66].

To justify the strong resemblance that emerges by comparing the temperature trend and that of the H/V recorded at TOR4, a direct dependency of this latter parameter on the meteorological conditions could be supposed. This behaviour is suggested in [67] that ascribes a fundamental role to barometric conditions variation concerning the composition of the noise wavefield. In [68] this behaviour is related to microseismic frequencies (lower than 1 Hz) and is related to oceanic storm waves. Reference [69] observes similar phenomena at very high latitudes: in that case the variations could be explained by cycles of freezing and thawing

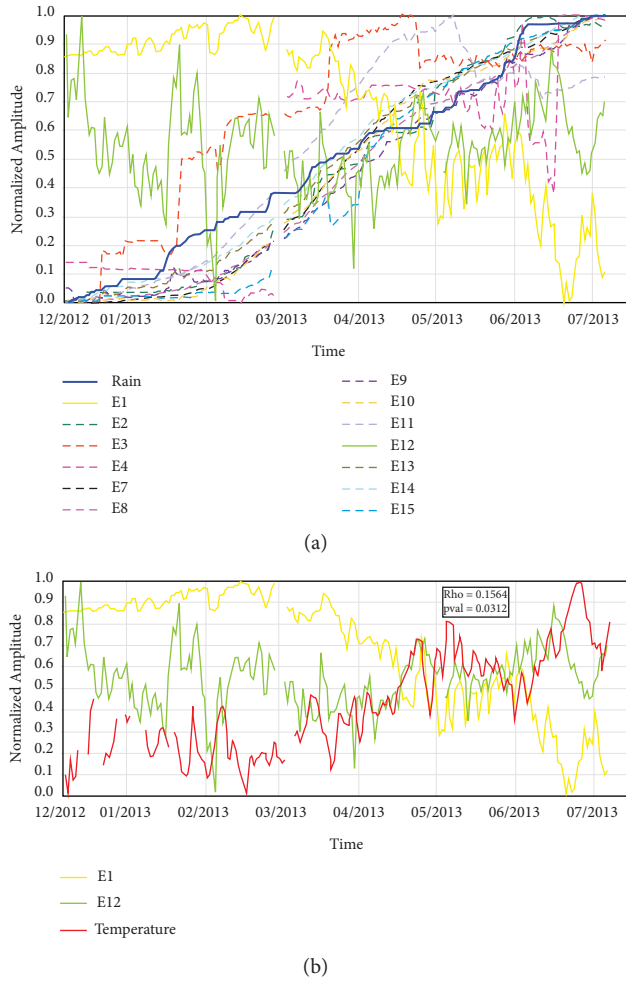


FIGURE 9: (a) The extensometer and rain trends and (b) two selected extensometer and temperature trends. The E2, E7, E8, E9, E10, E13, E14 trends show a clear correlation with the precipitation; the E3, E4, E11, E15 trends show a weaker correlation with the rain; the E1 trend shows an inverse correlation with the rain; the E12 trend does not show correlation either with rain or with temperature.

that crumble the rock surface and change their acoustic properties. Moreover, [70] points out how the HVSR amplitude could be affected by the local meteorological conditions (e.g., the wind). If this would be the case, an extended dataset (> 1 yr) would be necessary in order to clarify whether the observed variations at TOR4 are part of cyclical phenomenon occurring over longer periods as a consequence of seasonal changes. Unfortunately, at the Torgiovanetto quarry it was not possible to extend the experiment over longer time intervals because of the hard acquisition conditions. Nevertheless, the hypothesis that the HVSR amplitude value is directly related to meteorological factors can be excluded in Torgiovanetto area. All the stations, in fact, given their small spacing, should have shown the same amplitude increase. At the contrary, TOR1 shows a minimum in January 2013 and relatively constant values in the other months; TOR3 shows pronounced maxima on December 2012 and February 2013; TOR4 shows an increasing trend from January to July 2013.

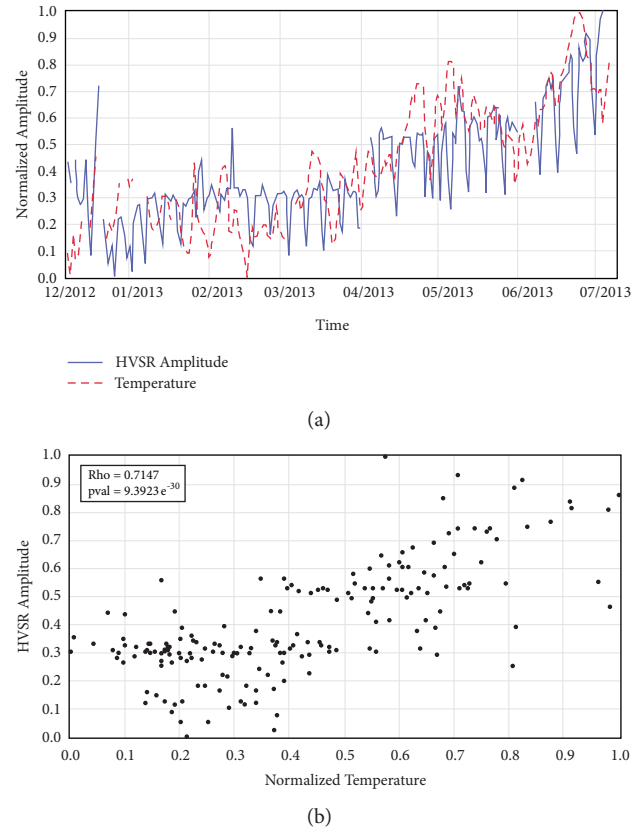


FIGURE 10: (a) HVSR peak amplitude at TOR4 and temperature. (b) Correlation between the HVSR TOR4 peak amplitude and the normalized temperature.

These H/V frequency variations could be associated with a different depth of fracturing (i.e., at site TOR1 fractures are shallower/near to the surface while at sites TOR3 and TOR4 they could be observed at depth) since the penetration of the surface waves is related to the frequency, but there are no experimental data on the depth of the fractures. Moreover, the surface geology at site TOR1 is characterized by stiffer or thicker geological unit, as indicated by the H/V frequency at 4.5 Hz. The surface geology at site TOR3 is characterized by softer/or thinner geological unit, as indicated by the H/V frequency at 2.5 Hz.

Probably the temperature variation does not directly affect the H/V amplitude but is responsible of other mechanisms like: (i) increasing of the fracturing degree of the medium acting directly on the dilatancy of the rocks (an increase in the medium fracturing may result, directly or, more often, indirectly, in density or velocity of propagation variations); (ii) influencing the water content of the superficial layer leading to an increase of the wave velocity of this portion of the slope. This hypothesis is supported by the variation in the impedance contrast which occurred with the approach of the hot season (early April, 2013) and therefore higher temperature (i.e., the water in the superficial layers is more prone to evaporate with the higher temperature).

Unfortunately, at the present state the lack of evidence of surface displacements corresponding to the observed variations in the HVSR amplitude trend foreclosed any possibility of threshold identification that could be used as an EWS. It could be interesting to evaluate this technique as a surveillance method when it can be calibrated on monitoring intervals characterized by a high rate of surface activity or over longer period in order to explain the cyclical variation of that parameter.

6. Conclusion

Implementing an EWS is a challenging issue in landslide monitoring. To verify the usefulness of seismic noise analysis as part of an EWS, a pilot scale experiment was arranged to monitor an unstable rock mass. A 7-month period of passive seismic data was analysed by means of the H/V method. Possible connection between rainfall/temperature/displacement and rockslide seismic activity was evaluated, and the hypothesis that the HV amplitude value is directly related to meteorological factors can be excluded. On the contrary, the H/V observed variations with time are interesting, in that they potentially reveal changes of subsoil site conditions and have also implications for the assessment of site response to seismic shaking. The presented analysis was just the first step to employ H/V variations in an EWS. Many efforts, in fact, have to be employed both to understand how the observed variations are correlated with slope stability conditions and to set up a reliable EWS. For the first point (a) a longer time acquisition period and (b) a comparison with many other parameters to model and interpret in a quantitative way are needed. There are many factors (like cracks, joints, rock diagenesis, and saturation), in fact, that could cause velocity or density variations and therefore influence the ellipticity and/or polarization of the surface waves. For the second point, there are some open questions like, (a) what is the main information that the EWS will receive, (b) how this information will be processed, (c) what are the preferred time responses, and (d) how the potential variations and/or errors from (a) and (b) will affect the false alarm/no alarm ratios of the EWS. Nonetheless, the rapid technological advances increasing the speed in acquisition, transmission, and processing of data suggest that it is clearly worthy to proceed in the field of seismic monitoring of unstable slopes.

Data Availability

The data used to support the findings of this study are available from the corresponding author upon request.

Conflicts of Interest

The authors declare that they have no conflicts of interest.

Acknowledgments

The Department of Earth Sciences (Unifi-DST) supported this research as part of its program to improve rockslide

early warning system (PRIN 2009 – Advanced monitoring techniques for the development of early warning procedures on large rockslides - prot. 20084FAHR7.001). We gratefully acknowledge Sara Electronic Instrument for providing the devices installed at the four seismic stations. We thank Massimiliano Nocentini and Luca Lombardi (Unifi-DST) for the huge efforts deployed to install, maintain, and make available the microseismic data and Francesco Ponziani (Centro Funzionale Regione Umbria) for providing meteorological data and very helpful comments and suggestions for the manuscript. Thanks are also due to Prof. Nicola Casagli (Unifi-DST) whose initial review was very helpful. The authors are also grateful to the anonymous reviewers for providing very helpful comments to improve the manuscript.

References

- [1] M. Van Den Eeckhaut and J. Hervás, "State of the art of national landslide databases in Europe and their potential for assessing landslide susceptibility, hazard and risk," *Geomorphology*, vol. 139-140, pp. 545–558, 2012.
- [2] P. M. Atkinson and R. Massari, "Generalised linear modelling of susceptibility to landsliding in the Central Apennines, Italy," *Computers & Geosciences*, vol. 24, pp. 373–385, 1998.
- [3] W. Frodella, T. Salvatici, V. Pazzi, S. Morelli, and R. Fanti, "Gb-InSAR monitoring of slope deformations in a mountainous area affected by debris flow events," *Natural Hazards and Earth System Sciences*, vol. 17, no. 10, pp. 1779–1793, 2017.
- [4] E. Intrieri, G. Gigli, F. Mugnai, R. Fanti, and N. Casagli, "Design and implementation of a landslide early warning system," *Engineering Geology*, vol. 147-148, pp. 124–136, 2012.
- [5] L. Zan, G. Latini, E. Piscina, G. Polloni, and P. Baldelli, "Landslides early warning monitoring system," in *Proceedings of the 2002 IEEE International Geoscience and Remote Sensing Symposium (IGARSS 2002)*, pp. 188–190, Canada, June 2002.
- [6] D. Arosio, L. Longoni, M. Papini, M. Boccolari, and L. Zanzi, "Analysis of microseismic signals collected on an unstable rock face in the Italian Prealps," *Geophysical Journal International*, vol. 213, no. 1, pp. 475–488, 2018.
- [7] G. Gigli, E. Intrieri, L. Lombardi et al., "Event scenario analysis for the design of rockslide countermeasures," *Journal of Mountain Science*, vol. 11, no. 6, pp. 1521–1530, 2014.
- [8] J. McKean, E. Bird, J. Pettinga, J. Campbell, and J. Roering, "Using LiDAR to objectively map bedrock landslides and infer their mechanics and material properties," in *Proceedings of the Denver Annual Meeting*, vol. 36, p. 332, Geological Society of America Abstract with Programs.
- [9] J. McKean and J. Roering, "Objective landslide detection and surface morphology mapping using high-resolution airborne laser altimetry," *Geomorphology*, vol. 57, no. 3-4, pp. 331–351, 2004.
- [10] J. A. Gili, J. Corominas, and J. Rius, "Using Global Positioning System techniques in landslide monitoring," *Engineering Geology*, vol. 55, no. 3, pp. 167–192, 2000.
- [11] J.-P. Malet, O. Maquaire, and E. Calais, "The use of global positioning system techniques for the continuous monitoring of landslides: Application to the Super-Sauze earthflow (Alpes-de-Haute-Provence, France)," *Geomorphology*, vol. 43, no. 1-2, pp. 33–54, 2002.
- [12] C. Squarzon, C. Delacourt, and P. Allemand, "Differential single-frequency GPS monitoring of the La Valette landslide

- (French Alps)," *Engineering Geology*, vol. 79, no. 3-4, pp. 215–229, 2005.
- [13] G. Antonello, N. Casagli, P. Farina et al., "Ground-based SAR interferometry for monitoring mass movements," *Landslides*, vol. 1, no. 1, pp. 21–28, 2004.
 - [14] N. Casagli, F. Catani, C. Del Ventisette, and G. Luzi, "Monitoring, prediction, and early warning using ground-based radar interferometry," *Landslides*, vol. 7, no. 3, pp. 291–301, 2010.
 - [15] F. Fidolini, V. Pazzi, W. Frodella, S. Morelli, and R. Fanti, "Geomorphological characterization, monitoring and modeling of the Monte Rotolon complex landslide (Recoaro Terme, Italy)," *Engineering Geology for Society and Territory - Volume 2: Landslide Processes*, pp. 1311–1315, 2015.
 - [16] N. Casagli, G. Gigli, E. Intrieri, L. Lombardi, M. Nocentini, and W. Frodella, "Applicazione di nuove tecnologie di indagine e monitoraggio per fenomeni di instabilità in ammassi rocciosi," in *Nuovi Metodi di Indagine, Monitoraggio e Modellazione degli Ammassi Rocciosi*, G. Barla, M. Barla, A. M. Ferrero, and T. Rotonda, Eds., pp. 137–158, Celid, Torino, 2012.
 - [17] G. Gigli and N. Casagli, "Extraction of rock mass structural data from high resolution laser scanning products," in *Landslide Science and Practice - Volume 3: Spatial Analysis and Modelling*, C. Margottini, P. Canuti, and K. Sassa, Eds., pp. 89–94, Springer, Berlin Heidelberg, 2013.
 - [18] I. Baron, D. Beckovsky, and M. Lumir, "Infrared thermography sensing for mapping open fractures in deep-seated rockslides and unstable cliffs," in *EGU General Assembly*, pp. 7–12, Vienna, Austria, 2013.
 - [19] W. Frodella, S. Morelli, and V. Pazzi, "Infrared thermographic surveys for landslide mapping and characterization: The Rotolon Dsgsd (Northern Italy) case study," *Italian Journal of Engineering Geology and Environment*, vol. 2017, no. 1, pp. 77–84, 2017.
 - [20] W. Frodella, F. Fidolini, S. Morelli, and V. Pazzi, "Application of infrared thermography for landslide mapping: The rotolon DSGDS case study," *Rendiconti Online Società Geologica Italiana*, vol. 35, pp. 144–147, 2015.
 - [21] J. R. Moore, V. Gischig, E. Button, and S. Loew, "Rockslide deformation monitoring with fiber optic strain sensors," *Natural Hazards and Earth System Sciences*, vol. 10, no. 2, pp. 191–201, 2010.
 - [22] D. Amitrano, M. Arattano, M. Chiarle et al., "Microseismic activity analysis for the study of the rupture mechanisms in unstable rock masses," *Natural Hazards and Earth System Sciences*, vol. 10, no. 4, pp. 831–841, 2010.
 - [23] D. Arosio, L. Longoni, M. Papini, M. Scaioni, L. Zanzi, and M. Alba, "Towards rockfall forecasting through observing deformations and listening to microseismic emissions," *Natural Hazards and Earth System Sciences*, vol. 9, no. 4, pp. 1119–1131, 2009.
 - [24] L. H. Blikra, "The Åknes rockslide: Monitoring, threshold values and early warning," in *Proceedings of 10th International Symposium on Landslides and Engineered Slopes*, vol. 30 July 4, pp. 1089–1094, Xian, P.R. China, 2008.
 - [25] A. Helmstetter and S. Garambois, "Seismic monitoring of Séchillienne rockslide (French Alps): Analysis of seismic signals and their correlation with rainfalls," *Journal of Geophysical Research: Atmospheres*, vol. 115, no. F3, 2010.
 - [26] A. Lotti, G. Saccorotti, A. Fiaschi et al., "Seismic monitoring of rockslide: the Torgiovanetto quarry (Central Apennines, Italy)," in *Proceedings of the Engineering Geology for Society and Territory*, G. Lollino, Ed., vol. 2, pp. 1537–1540, Italy, 2014.
 - [27] V. Pazzi, L. Tanteri, G. Bicocchi, M. D'Ambrosio, A. Caselli, and R. Fanti, "H/V measurements as an effective tool for the reliable detection of landslide slip surfaces: Case studies of Castagnola (La Spezia, Italy) and Roccalbegna (Grosseto, Italy)," *Physics and Chemistry of the Earth, Parts A/B/C*, vol. 98, pp. 136–153, 2017.
 - [28] A. Graziani, M. Marsella, T. Rotonda, P. Tommasi, and C. Soccodato, "Study of a rock slide in a limestone formation with clay interbeds," in *Proceedings of the International Conference on Rock Joints and Jointed Rock Masses*, Tucson, Arizona, USA 7th–8th, 2009.
 - [29] M. Boccaletti, P. Elter, and G. Guazzone, "Plate tectonic models for the development of the western alps and northern apennines," *Nature Physical Science*, vol. 234, no. 49, pp. 108–111, 1971.
 - [30] M. Barchi, A. DeFeyter, B. Magnani, G. Minelli, G. Piali, and B. Sotera, "The structural style of the Umbria-Marche fold and thrust belt," *Memorie della Società Geologica Italiana*, vol. 52, pp. 557–578, 1998.
 - [31] G. Lavecchia, G. Minelli, and G. Piali, "The Umbria-Marche arcuate fold belt (Italy)," *Tectonophysics*, vol. 146, no. 1-4, pp. 125–137, 1988.
 - [32] E. Tavarnelli, "Structural evolution of a foreland fold-and-thrust belt: The Umbria-Marche Apennines, Italy," *Journal of Structural Geology*, vol. 19, no. 3-4, pp. 523–534, 1997.
 - [33] R. C. Wilson and D. K. Keefer, *Dynamic Analysis of a Slope Failure from the 6 August 1979 Coyote Lake, California, Earthquake*, vol. 73, Bulletin of the Seismological Society of America, 1983.
 - [34] D. K. Keefer, "Landslides caused by earthquakes," *Geological Society of America Bulletin*, vol. 95, no. 4, pp. 406–421, 1984.
 - [35] R. W. Jibson and D. K. Keefer, "Analysis of the seismic origin of landslides: examples from the New Madrid seismic zone," *Geological Society of America Bulletin*, vol. 105, no. 4, pp. 521–536, 1993.
 - [36] B. Khazai and N. Sitar, "Evaluation of factors controlling earthquake-induced landslides caused by Chi-Chi earthquake and comparison with the Northridge and Loma Prieta events," *Engineering Geology*, vol. 71, no. 1-2, pp. 79–95, 2004.
 - [37] M. Locati, R. Camassi, and M. Stucchi, "DBMI11, the 2011 version of the Italian Macroseismic Database. Milano, Bologna," <http://emidius.mi.ingv.it/DBMI11>, 2011.
 - [38] D. M. Cruden and D. J. Varnes, "Landslides Types and Processes," in *Landslides: Investigation and Mitigation. Transportation Research Board Special Report 247*, A. K. Turner and R. L. Schuster, Eds., pp. 36–75, National Academy Press, 1996.
 - [39] F. Ponziani, N. Berni, C. Pandolfo, M. Stelluti, and L. Brocca, "An integrated approach for the real-time monitoring of a high risk landslide by a regional civil protection office," in *Proceedings of the EGU Leonardo Topical Conference Series on the hydrological cycle*, pp. 10–12, Luxembourg, 2010.
 - [40] M. Balducci, R. Regni, S. Buttiglia et al., "Design and built of a ground reinforced embankment for the protection of a provincial road (Assisi, Italy) against rockslide," in *Proceedings of the XXIV Conv. Naz. Geotecnica*, AGI, 22th–24th, 2011.
 - [41] M. Nogoshi and T. Igarashi, "On the propagation characteristics estimations of subsurface using microtremors on the ground surface," *Journal of the Seismological Society of Japan*, vol. 23, pp. 264–280, 1970.
 - [42] M. Nogoshi and T. Igarashi, "On the amplitude characteristics of microtremor (part 2)," *Journal of the Seismological Society of Japan. 2nd ser*, vol. 24, no. 1, pp. 26–40, 1971.

- [43] Y. Nakamura, "Method for dynamic characteristics estimation of subsurface using microtremor on the ground surface," *Quarterly Report of RTRI (Railway Technical Research Institute) (Japan)*, vol. 30, no. 1, pp. 25–33, 1989.
- [44] Y. Nakamura, "Clear identification of fundamental idea of Nakamura's technique and its applications," *I2WCEE*, 2000.
- [45] M. Bour, D. Fouissac, P. Dominique, and C. Martin, "On the use of microtremor recordings in seismic microzonation," *Soil Dynamics and Earthquake Engineering*, vol. 17, no. 7-8, pp. 465–474, 1998.
- [46] P. Volant, F. Cotton, and J. C. Gariel, "Estimation of site response using the H/V method. Applicability and limits of this technique on Garner Valley Downhole Array dataset (California)," in *Proceedings of 11th European Conference Earthquake*, p. 13, 1998.
- [47] P. G. Malischewsky and F. Scherbaum, "Love's formula and H/V-ratio (ellipticity) of Rayleigh waves," *Wave Motion. An International Journal Reporting Research on Wave Phenomena*, vol. 40, no. 1, pp. 57–67, 2004.
- [48] V. Pazzi, M. Di Filippo, M. Di Nezza et al., "Integrated geophysical survey in a sinkhole-prone area: Microgravity, electrical resistivity tomographies, and seismic noise measurements to delimit its extension," *Engineering Geology*, vol. 243, pp. 282–293, 2018.
- [49] M. Del Soldato, V. Pazzi, S. Segoni, P. De Vita, V. Tofani, and S. Moretti, "Spatial modeling of pyroclastic cover deposit thickness (depth to bedrock) in peri-volcanic areas of Campania (southern Italy)," *Earth Surface Processes and Landforms*, 2018.
- [50] A. Lotti, A. M. Lazzeri, S. Beja, and V. Pazzi, "Could ambient vibrations be related to cerithidea decollate migration?" *International Journal of Geosciences*, vol. 08, no. 03, pp. 286–295, 2017.
- [51] V. Pazzi, S. Morelli, F. Fidolini, E. Krymi, N. Casagli, and R. Fanti, "Testing cost-effective methodologies for flood and seismic vulnerability assessment in communities of developing countries (Dajç, northern Albania)," *Geomatics, Natural Hazards and Risk*, vol. 7, no. 3, pp. 971–999, 2016.
- [52] V. Pazzi, S. Morelli, F. Pratesi et al., "Assessing the safety of schools affected by geo-hydrologic hazards: The geohazard safety classification (GSC)," *International Journal of Disaster Risk Reduction*, vol. 15, pp. 80–93, 2016.
- [53] V. Pazzi, A. Lotti, P. Chiara, L. Lombardi, M. Nocentini, and N. Casagli, "Monitoring of the vibration induced on the Arno masonry embankment wall by the conservation works after the May 25, 2016 riverbank landslide," *Geoenvironmental Disasters*, vol. 4, no. 1, 2017.
- [54] D. Albarello and E. Lunedei, "Combining horizontal ambient vibration components for H/V spectral ratio estimates," *Geophysical Journal International*, vol. 194, no. 2, pp. 936–951, 2013.
- [55] S. Castellaro, "The complementarity of H/V and dispersion curves," *Geophysics*, vol. 81, no. 6, pp. T323–T338, 2016.
- [56] V. Pazzi, M. Ceccatelli, T. Gracchi, E. B. Masi, and R. Fanti, "Assessing subsoil void hazards along a road system using H/V measurements, ERTs, and IPTs to support local decision makers," *Near surface Geophysics*, vol. 16, pp. 282–297, 2018.
- [57] H. B. Havenith, D. Jongmans, E. Faccioli, K. Abdrakhmatov, and P. Bard, "Site effect analysis around the seismically induced Ananevo rockslide, Kyrgyzstan," *Bulletin of the Seismological Society of America*, vol. 92, no. 8, pp. 3190–3209, 2002.
- [58] O. Méric, S. Garambois, J.-P. Malet, H. Cadet, P. Guéguen, and D. Jongmans, "Seismic noise-based methods for soft-rock landslide characterization," *Bulletin de la Société Géographique de France*, vol. 178, no. 2, pp. 137–148, 2007.
- [59] S. Gaffet, Y. Guglielmi, F. Cappa, C. Pambrun, T. Monfret, and D. Amitrano, "Use of the simultaneous seismic, GPS and meteorological monitoring for the characterization of a large unstable mountain slope in the southern French Alps," *Geophysical Journal International*, vol. 182, no. 3, pp. 1395–1410, 2010.
- [60] M. Horike, B. Zhao, and H. Kawase, "Comparison of site response characteristics inferred from microtremors and earthquake shear waves," *Bulletin of the Seismological Society of America*, vol. 91, no. 6, pp. 1526–1536, 2001.
- [61] S. Parolai and J. J. Galiana-Merino, "Effects of transient seismic noise on estimates of H/V spectral ratio," *Bulletin of the Seismological Society of America*, vol. 96, pp. 228–236, 2006, <https://doi.org/10.1785/0120050084>.
- [62] F. Vallianatos and G. Hloupis, "HVSr technique improvement using redundant wavelet transform," in *Increasing Seismic Safety by Combining Engineering Technologies and Seismological Data*, NATO Science for Peace and Security Series C: Environmental Security, pp. 117–137, Springer Netherlands, Dordrecht, 2009.
- [63] M. Mucciarelli, M. R. Gallipoli, and M. Arcieri, "The stability of the horizontal-to-vertical spectral ratio of triggered noise and earthquake recordings," *Bulletin of the Seismological Society of America*, vol. 93, no. 3, pp. 1407–1413, 2003.
- [64] T. T. Tuan, F. Scherbaum, and P. G. Malischewsky, "On the relationship of peaks and troughs of the ellipticity (H/V) of Rayleigh waves and the transmission response of single layer over half-space models," *Geophysical Journal International*, vol. 184, no. 2, pp. 793–800, 2011.
- [65] V. Del Gaudio, S. Muscillo, and J. Wasowski, "What we can learn about slope response to earthquakes from ambient noise analysis: An overview," *Engineering Geology*, vol. 182, pp. 182–200, 2014.
- [66] J. Burjánek, J. R. Moore, F. X. Yugsi Molina, and D. Fäh, "Instrumental evidence of normal mode rock slope vibration," *Geophysical Journal International*, vol. 188, no. 2, pp. 559–569, 2012.
- [67] D. Albarello, "Possible effects of regional meteoroclimatic conditions on HVSr," in *Proceedings of the ATO SfP 980857 – II- Intermediate Meeting*, pp. 25–27, 2006.
- [68] T. Tanimoto, S. Ishimaru, and C. Alvizuri, "Seasonality in particle motion of microseisms," *Geophysical Journal International*, vol. 166, no. 1, pp. 253–266, 2006.
- [69] R. F. Lee, R. E. Abbott, H. A. Knox, and A. Pancha, "Seasonal changes in H/V spectral ratio at high-latitude seismic stations," in *Proceedings of the American Geophysical Union - AGU, Fall Meeting*, 2014.
- [70] M. Mucciarelli, M. R. Gallipoli, D. Di Giacomo, F. Di Nota, and E. Nino, "The influence of wind on measurements of seismic noise," *Geophysical Journal International*, vol. 161, no. 2, pp. 303–308, 2005.

Research Article

Integrated Geophysical-Geological 3D Model of the Right-Bank Slope Downstream from the Rogun Dam Construction Site, Tajikistan

Hans-Balder Havenith ¹, Isakbek Torgoev,² and Anatoli Ischuk³

¹Department of Geology, Liege University, Liege, Belgium

²Institute of Geomechanics and Mining, Academy of Sciences, Bishkek, Kyrgyzstan

³Institute of Geology, Earthquake Engineering and Seismology, Academy of Sciences, Dushanbe, Tajikistan

Correspondence should be addressed to Hans-Balder Havenith; hb.havenith@uliege.be

Received 30 March 2018; Revised 18 July 2018; Accepted 2 August 2018; Published 27 August 2018

Academic Editor: Veronica Pazzi

Copyright © 2018 Hans-Balder Havenith et al. This is an open access article distributed under the Creative Commons Attribution License, which permits unrestricted use, distribution, and reproduction in any medium, provided the original work is properly cited.

In summer of 2015 we had completed a geophysical survey complemented by borehole drilling near the right-bank slope of the Rogun Dam construction site, Tajikistan. These data were first processed and then compiled within a 3D geomodel. The present paper describes the geophysical results and the 3D geomodel generated for an ancient mass movement located immediately downstream from the construction site. The geophysical survey included electrical and seismic profiles and ambient vibration measurements as well as earthquake recordings. The electrical and seismic data were processed as tomographic sections, the ambient vibrations as horizontal-to-vertical spectral H/V ratios, and the earthquake data mainly in terms of standard spectral ratios. By estimating the average shear wave velocities of the subsurface, we computed the local soft layer thickness from the resonance frequencies revealed by the H/V ratios. Three seismic stations had been installed for ten days along a profile crossing the intermediate plateau. Standard spectral ratios inferred from ten processed earthquake measurements confirmed the presence of a thick soft material layer on the plateau made of weathered rocks, colluvium, and terrace deposits, which produce a medium-level amplification at about 2 Hz. The 3D geomodel was first built on the basis of new topographic data, satellite imagery, and a geological map with two sections. Then, the various electrical resistivity and seismic refraction tomographies were inserted in the geomodel. The soft layer thickness information and borehole data were represented in terms of logs in the model. The site is crossed by the Ionakhsh Fault that could be modeled on the basis of the geological inputs and of a lateral resistivity gradient found on one electrical profile along the steep lower slope. The integrated interpretation of all results reveals that probably only a relatively small part of the ancient giant mass movement is really exposed to slope instability phenomena.

1. Introduction

The Rogun dam construction site is located in central Tajikistan within the Vakhsh River valley at about 100 km in the Northeast of Tajikistan's capital Dushanbe and 40 km upstream from the Nurek reservoir. The project of the construction of the dam and the associated hydropower plant (HPP) had already started when Tajikistan still belonged to the Soviet Union. It was part of a much wider project of hydropower plant construction that was completed by the Soviet Union in Central Asian countries, including also other dams and HPPs constructed along Vakhsh River in Tajikistan

as well as the large hydropower cascade along Naryn River in Kyrgyzstan (Figure 1). There, the last construction of the (relatively small) Kambarata 2 dam had been completed in 2012; at present, it is the only 'blast-fill' dam within the two hydropower cascades (a full description of the blast event, construction works, and geophysical investigations on the dam is provided by Havenith et al. [1]).

The Rogun dam construction project was relaunched in the beginning of this century (2005) under the present-day's (2018) government. As for many other types of dams, the site for this one had been selected in a very narrow part of the Vakhsh River valley (to reduce the amount of material needed

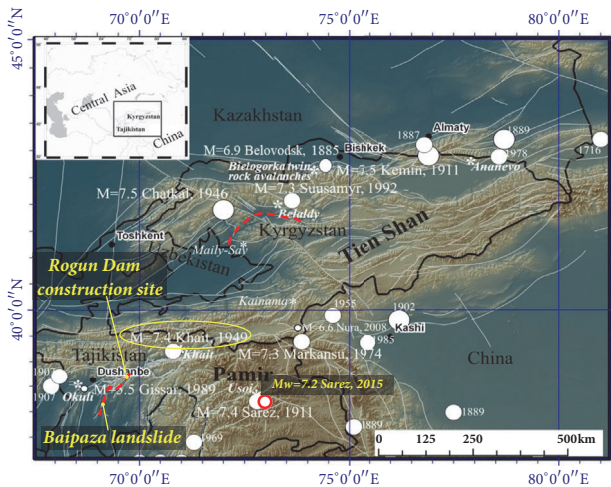


FIGURE 1: Map of Tien Shan and Pamir Mountains in Central Asia with location of major faults and earthquakes (white circles show all recorded $M \geq 6.9$ earthquakes with the year of occurrence; the magnitude is indicated for analysed events) and related major mass movements (stars). Highlighted by red dashed lines are the Naryn HPP cascade in Kyrgyzstan and the one of Vakhsh River in Tajikistan; the locations of the Rogun dam construction site and of the Baipaza landslide, as well as the epicentral areas of the 1949 Khait earthquake and the 2015 Sarez earthquake (red circle) are indicated (modified from Havenith and Bourdeau, 2010).

for construction). The associated Rogun HPP will be part of the cascade of already existing HPPs, including those of Nurek, Baipaza, Sangtuda 1+2, and the "Golovnaya" (head, or final). The Rogun dam, just as Nurek dam, is designed as a rockfill dam with a clay core. At the end of the 70s, Nurek dam had been the tallest dam in the world (with a height of 300 m); right now Nurek is the second tallest one after Jinping-I dam in China. After completion, the Rogun dam would be the future tallest dam on Earth (design height of 335 m).

The present paper is focused on a geophysical survey that had been completed in summer 2015 on a large slope downstream and a smaller one upstream from the Rogun dam construction site. This survey included electrical and seismic profiles as well as ambient noise measurements and earthquake recordings supported by differential GPS positioning (methods are detailed under Section 3). Results from related data processing were then combined in a 3D geomodel of the site. A very similar type of site characterization has been completed with the same methods by Ulysse et al. [2] for a hill site in Port-au-Prince, for which topographic amplification effects had to be assessed.

The objectives of this survey are related to the general hazard situation of the Rogun HPP that is now under construction. The obviously most important regional type of hazard to which the selected site is exposed (just as the other HPP sites downstream) is the one related to earthquakes: the site is located at 100 km in the southwest of the epicentral zone of the catastrophic 1949 Khait earthquake, and at 300-350 km in the West of the 1911 Sarez earthquake (see summary of events in Havenith and Bourdeau [3]). It should be noted that

only a few months after our survey in 2015, the Sarez region was hit by another $M > 7$ earthquake.

At local scale, the site is affected by multiple types of mass movement-related hazards; such hazards are perfectly exemplified by those that had been induced by the two largest aforementioned events, in 1911 and 1949: rock avalanching and river damming. The $M=7.4$ Khait earthquake triggered several large mass movements, including the Khait rock avalanche that had partly covered the town of Khait [4, 5], while the Sarez earthquake triggered a giant rockslide that formed the presently tallest (intact) natural dam on Earth, the Usody dam [6].

The interest in the slope site downstream from the construction area is also related to the risk of formation of a landslide dam near the exit of the spillway of the Rogun dam. This risk is exemplified by an event that occurred in 2002 near the Baipaza dam and hydropower plant (HPP) that also belong to the Tajik HPP cascade. At that time, a massive failure affected the already existing and identified Baipaza landslide at 4.5 km downstream from the Baipaza HPP (see also Havenith et al. [7]). The first displacement of this landslide had been observed in 1968 when it partially blocked Vakhsh River, even before design and construction of the Baipaza HPP. In 1969, the volume of the Baipaza landslide was assessed to be 20-25 million m^3 . In May, 1992, the Baipaza landslide moved again as a result of heavy rains, and the Vakhsh River was dammed. After the March 3, 2002, deep-focal $Mw=7.4$ Hindu Kush earthquake (with an epicentre located in Afghanistan at a distance 250 km from the Baipaza site, and with an intensity of shaking of 6 degrees on EMS-98 scale), this landslide started to move and partially blocked again the Vakhsh River (Figure 2). As a result, a lake formed upstream from the dam and partly inundated the Baipaza HPP, which could not operate at a normal level for one month. The use of high explosives was required to clear the river bed after this landslide. Note that the view of Baipaza rockslide of 2007 in Figure 2 still shows the presence of the cascade across the dam that had been breached in 2002. Now, the cascade cannot be seen anymore due to river erosion.

As introduced above, the larger downstream zone (Site 1) of the Rogun dam construction site was studied to assess the probability of occurrence of a massive failure event similar to the one observed downstream from Baipaza HPP in 2002; the smaller upstream Site 2 that can be seen on some maps (Figures 6 and 7) was investigated due to the possibility of a potentially tsunamigenic impact of an existing mass movement on the lake. Investigations on both sites are described below (see also Torgoev et al. [8]), with focus on the larger Site 1.

2. The Seismic Hazard and Geological Context of the Dam Site

As seismic hazard maps can provide a more general overview on the seismotectonic activity of a region and its effects on the surface than singular events, and, over a certain period of time, it is important to situate the Rogun site in its regional seismic hazard context. Relatively recent seismic hazard maps for the target region have been produced by Abdrakhmatov

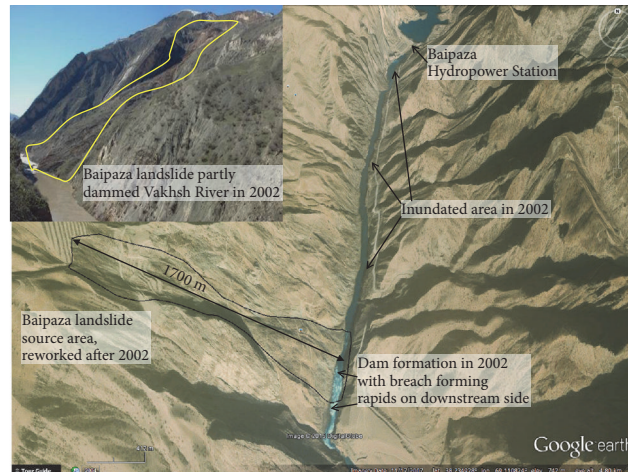


FIGURE 2: Google Earth® view (to N) of the Baipaza rockslide and upstream Baipaza HPP. This image of 2007 still shows the cascade that Vakhsh River formed after crossing the dam that had been formed and actively reopened in 2002.

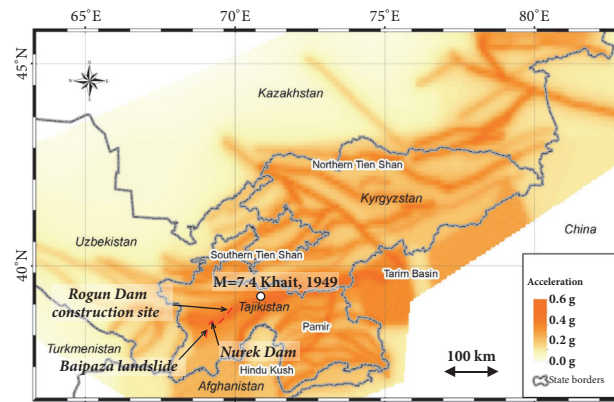


FIGURE 3: Seismic hazard map of the Southeastern part of Central Asia, entirely including the countries of Kyrgyzstan and Tajikistan (modified from Ischuk et al., 2018). Indicated are the locations of the Khait earthquake epicentral region, the Rogun and Nurek sites, and the Baipaza landslide just downstream from the Baipaza HPP.

et al. [11] and Bindi et al. [12], the first one covering only the northernmost part of Tajikistan while the second fully covers Tajikistan. The most recent seismic hazard map has been computed by Ischuk et al. [13]. Actually, Ischuk et al. [13] produced several maps for this part of Central Asia (calculated for a 475-year return period), one considering a 75% contribution by regional (or zonal) and 25% by fault-related seismic ground motion hazards, one considering a 25% regional and 75% fault-related contribution, and the seismic hazard map shown (Figure 3) for a 50% zonal and 50% fault-related contribution. This map shows that the entire Vakhsh hydropower cascade is exposed to a minimum seismic hazard of about 0.3 g. As the Rogun site is located in the northern part of the cascade, it is closer to the active fault zones of the southern Tien Shan, which induce a seismic hazard of even more than 0.4 g (with 10% exceedance probability in 50 years). Comparable high values are displayed on the two other maps (not shown here, the first with stronger regional seismicity and the second with a stronger fault contribution) and were also obtained by the

two other assessments, noting that Bindi et al. [12] expressed their results in terms of Intensities: 7 for the southern part of the Vakhsh HPP cascade and 9 for the northern part.

It should be noted that such large dam structures due to the deep lakes formed upstream are often not only exposed to the effects of natural seismicity, but also to those due to reservoir-triggered seismicity during and just after reservoir filling (generally during the first years after filling—but this could also last longer in the case of Rogun as filling will take a long time and as the lake will be particularly large and deep). For instance, extensive induced seismicity had been observed after the filling of the Nurek reservoir in the 70s [14].

Here, we will not discuss in detail the possible effects of the reservoir-triggered seismicity related to the future filling of the Rogun reservoir. Large-scale effects are generally not expected as a consequence of the reservoir-triggered seismicity, due to the limited magnitudes of related earthquakes ($M < 5$ for the Nurek case); note that exceptional magnitudes of up to 6 had been observed after filling of

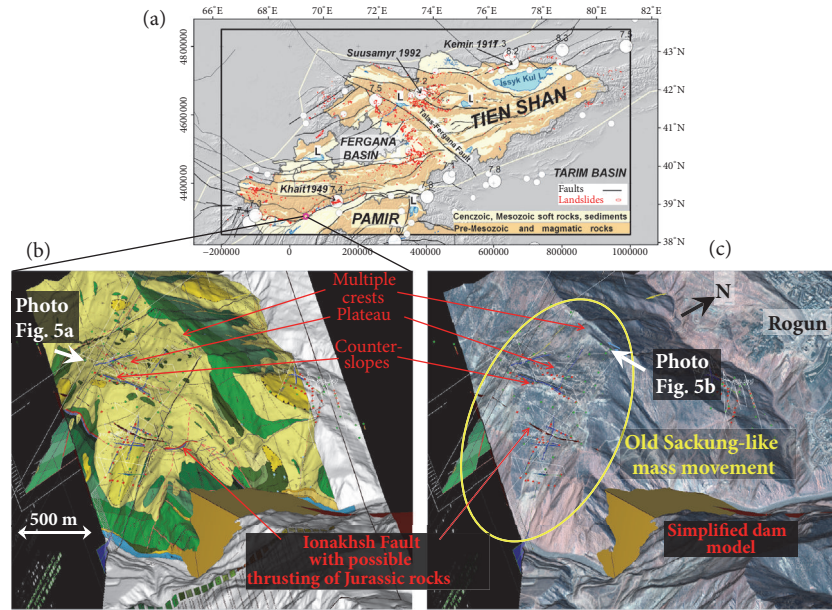


FIGURE 4: Simplified geological map of the Tien Shan (from Havenith et al. [9]). Views of 3D model of site with geological map ((b): green: Cretaceous sandstone bedrock; yellow: quaternary surface deposits, terraces, and colluvium) and a Pleiades image (of September 2015, (c)) projected on the surface, showing also the location of the dam and of the Ionakhsh Fault and elements of the ancient Sackung-like massive slope failure.

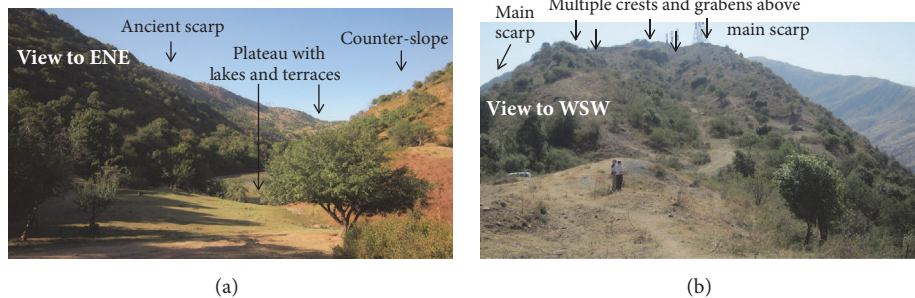


FIGURE 5: Field photographs showing elements of the large ancient Sackung-like mass movement. (see orientation and location of views in Figure 4: (a) view in western part to ENE; (b) view in eastern part to WSW).

the Koyna dam (see paper by Chopra and Chakrabarti [15]). Nevertheless, seismic ground motions can be locally very intense as the hypocentres of those medium-size earthquakes are generally located close to the surface (at depths that can be less than 5 km); if located near the dam structure, shallow $M > 4$ events could cause fractures within the dam (e.g., according to Chopra and Chakrabarti, 1973, the Koyna $M = 6.5$ earthquake had caused damage on the concrete Koyna dam) and neighbouring slopes.

Massive failures along the neighbouring slopes could, however, only occur if a natural $M \geq 7$ earthquake (similar to the aforementioned Khait earthquake) hits the Rogun region. Anyway, the investigations described below were designed to provide inputs for estimates of possible slope failures of multiple origins, induced by purely static (mainly on groundwater pressure depending) factors or by small (or higher frequency) or stronger (lower frequency) seismic ground motions.

The general geological context of the Rogun site is related to its position near the southern border of the Tien Shan. Immediately to the north of the site, the pre-Mesozoic rocks of the Tien Shan are outcropping, while the site itself is located in Mesozoic rocks (see general geological map of the Tien Shan in Figure 4(a)). Most of the right-bank slopes are made of Cretaceous sandstones (green layers in Figure 4(b)) widely covered by colluvium and along the central plateau (see location in Figure 4(c)) also by terrace deposits. Along this plateau also two lakes can be found (one is shown in the photograph in Figure 5(a)). In the central part of the lower slope also upthrust Jurassic clayey rocks can be found. They are markers of the presence of the Ionakhsh Fault that crosses the site from ENE to WSW.

The origin of the intermediate plateau on the right-bank slope downstream from the dam construction site can be explained by an ancient Sackung-like movement of that slope. Another interpretation would be that the

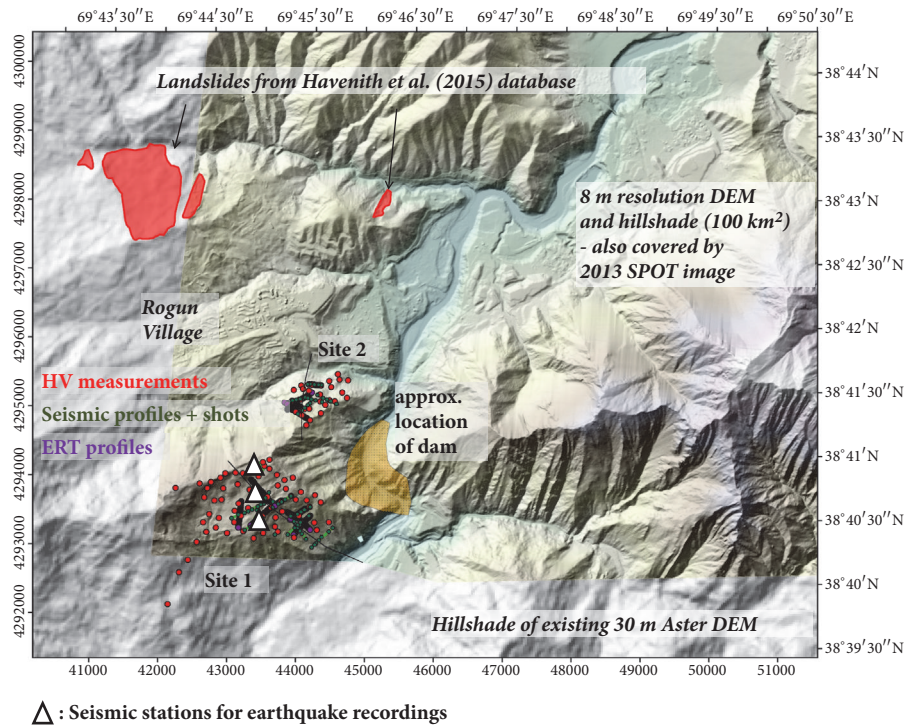


FIGURE 6: Overview of investigated sites with types of measurements indicated. Measurement locations plotted on a hill-shade map, with locations of landslides (reddish) extracted from the geographic-geological database (by Havenith et al. [10]) with overlay of a new 8 m resolution DEM. See detailed site survey views in Figure 8.

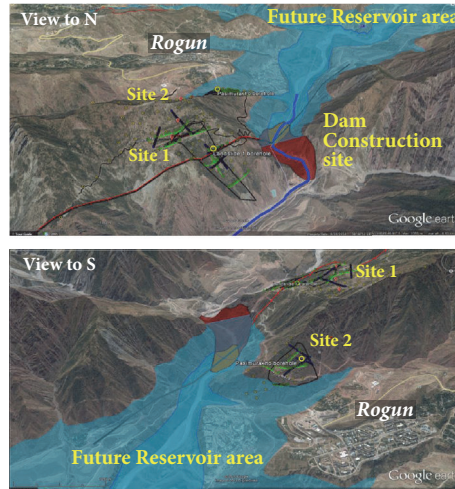


FIGURE 7: Overview of the two investigated sites (Google Earth® views, see detail on types of surveys in Figure 8). Also shown: approximate outlines of the future Rogun dam structure and of the two main reservoir levels (darker and light blue filling of reservoir outlines) after an intermediate and the final construction.

plateau is just the remnant of a river terrace—especially as terrace material is found on this plateau. The interpretation of the whole slope as a major Sackung therefore requires additional elements—the most important one is the presence of multiple crests and graben structures on top of the upper slope (above the plateau, see photograph in Figure 5(b)) that can be considered as the main scarp of the Sackung.

3. The 2015 Rogun Geophysical Field Survey

An overview of the Rogun dam site (in 2015, before the start of dam construction in 2016) and the neighbouring investigated areas is shown in Figures 6 and 7. The first presents an overview map; the second includes Google Earth® imagery views of the investigated sites, with an approximate representation of the future dam structures (that are now being built and would be completed in two stages) and respective lake

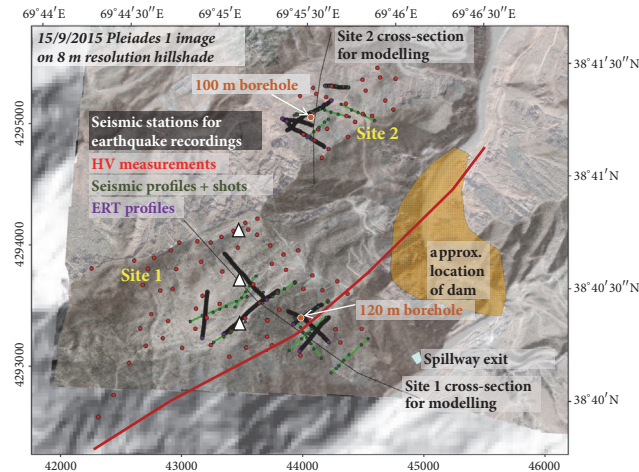


FIGURE 8: Pleiades 2015 satellite image of the surveyed areas outlining types of geophysical measurements and observations: Sites 1 and 2. Black bold lines are electrical resistivity tomography profiles (ERT), green lines are seismic refraction tomography profiles (SRT), red dots are H/V ambient noise measurement points, and triangles are the locations of seismic stations. See also location of the spillway exit (marked by light polygon in lower right corner) and of the boreholes and cross-section that had been used for seismic ground motion simulations and slope stability calculations (not shown in this paper).

levels. A more detailed overview map of the investigated sites with indication of the survey types is shown in Figure 8.

In 2015, our teams had been asked by local officials to study specifically those two sites as both of them present geomorphic features of ancient mass movements: as introduced above, Site 1 presents a terrace-like plateau above the middle part of the slope that could be related to a very old ($\gg 1000$ y) massive Sackung; Site 2 has characteristics of an old rockslide with clearly destroyed rock structures. The main “risk” question concerns the reactivation potential of those two ancient massive failures; in this regard, we have to consider that for Site 2 the stability conditions would drastically change with reservoir filling as the toe of the rockslide would be inundated (after complete filling), while for Site 1 the situation will not really change after reservoir filling. The external factor that could contribute to instability on both sites is a major earthquake event near the dam site. Such an earthquake could be either natural as we are located in a seismically active area or induced by the reservoir filling. In both cases, the presence of weak structures such as a fault zone and of groundwater reduces slope stability in general while ground motion amplification effects specifically contribute to the seismic slope failure triggering potential. Therefore, our investigations targeted the detection of both weak zones and wet zones as well as the determination of seismic ground response characteristics. This was achieved through the combination of electrical and seismic methods, combined with seismological measurements.

In total, on both sites up- and downstream from the future dam, we completed a dozen electrical resistivity tomography (ERT) and about the same amount of seismic refraction tomography (SRT) profiles, as well as 92 single station ambient noise (H/V) measurements. In addition to the geophysical measurements, we carried out earthquake recordings during 10 days (only on Site 1); in addition, geotechnical tests were completed on samples collected from two new boreholes (one

120 m deep borehole on Site 1 and one 100 m deep borehole on Site 2).

After processing of all geophysical data, the survey results (including also the borehole data) have been inserted in a 3D geological-geophysical model that was completed with the GOCAD software [16], which will be described in the next section. To support modeling, a new 8 m resolution digital elevation model had been constructed (produced upon order by Apollo Mapping) and new orthorectified high-resolution remote imagery (recent Pleiades and Spot images) had been acquired.

The electrical resistivity survey included 12 ERT profiles (using a GeoTom system with four cables and 100 electrodes) with a total length of 4150 meters and installation of 1035 electrodes (7 profiles on Site 1 and 5 profiles on Site 2, see Figure 8, with some profiles being along the same line to get longer profiles). All electrodes (with a spacing of 4 m between electrodes on all profiles) had been located with a differential GPS (DGPS) with a precision of about 20 cm. For the measurements, we used for all profiles the Wenner array configuration. In the laboratory, data were then processed with the 2D inversion algorithm of Loke and Barker [17] implemented in the RES2DINV software. Four processed ERT profiles on Site 1 are presented in Figure 9.

Examples of ERTs shown in Figure 9 show that the electrical resistivity values are highly variable over Site 1. Along the uppermost profile (ERT near upper scarp, Figure 9(a)) and along the intermediate crest (ERT in Figure 9(b)), relatively high resistivities (>500 ohm.m) were measured all along the investigated profiles. Much lower resistivity values (<100 ohm.m) have been measured along profiles completed on the intermediate plateau (ERT in Figure 9(d)) and along the lower steep slope (ERT in Figure 9(c)). Those lower values are probably indicative both of the presence of soft rocks and/or deposits and of groundwater in the subsoil. Along the plateau it is more likely that these wet soft materials are made

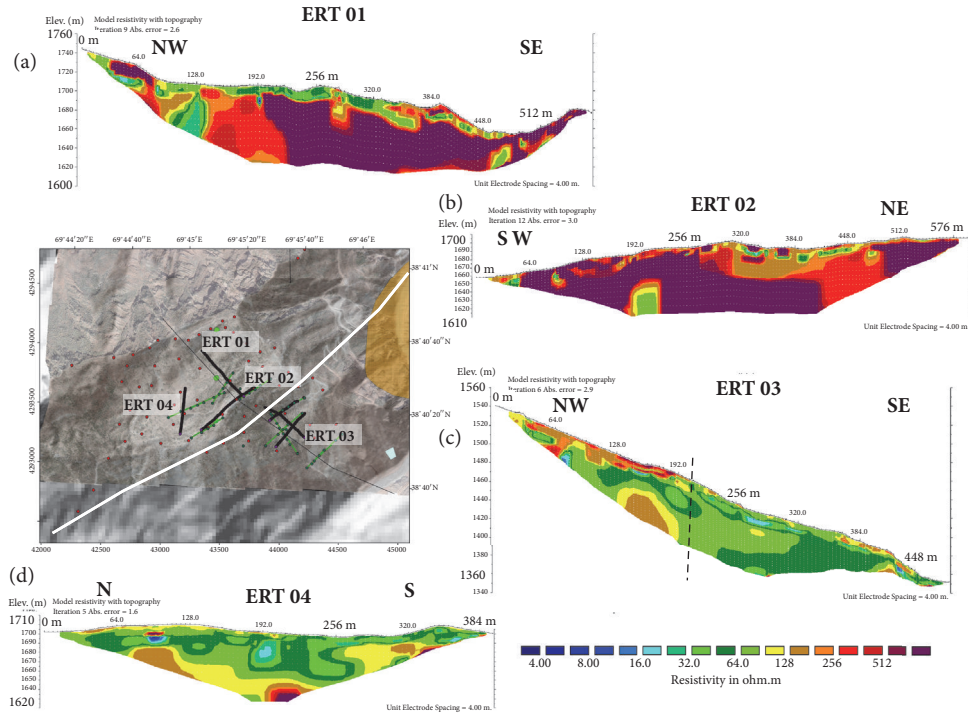


FIGURE 9: Examples of ERT profiles on Site 1 (see resistivity scale in lower right corner, in ohm.m): (a) 576 long ERT in upper part of slope; (b) 576 m long ERT along intermediate slope break; (c) main slope Section 448 m long ERT; (d) near lake-site 384 m long ERT. See in (c) also the dashed line that represents the possible marker of the Ionakhsh Fault crossing the site (shown by white line on the map).

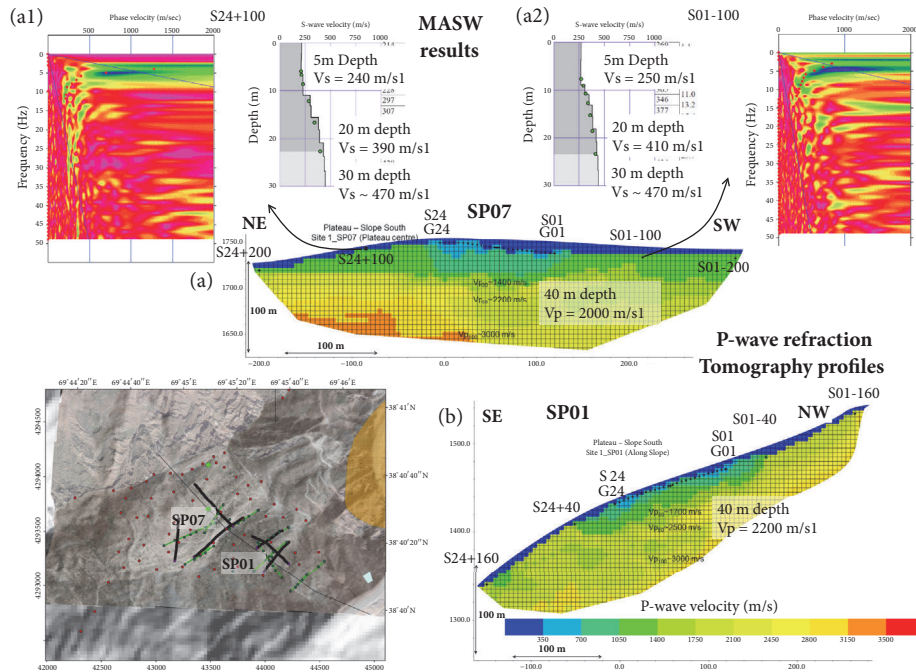


FIGURE 10: Examples of P-wave SRT profiles and MASW results on Site 1: (a) SRT for seismic profile SP07 parallel to the valley orientation, with shots S01 (at 0 m, near first geophone G01) and S24 (at 115 m, near last geophone G24), with 100 m offsets to both sides (S01-100, S24+100) and 200 m offsets (S01-200, S24+200); (a1) and (a2) show MASW results (V_s -logs and surface wave dispersion diagrams) obtained for SP07 for the two 100 m offset shots. (b) SRT for seismic profile SP01 along the main steep slope, with shots S01 (at 0 m, near first geophone G01) and S24 (at 115 m, near last geophone G24), with 40 m offsets to both sides (S01-40, S24+40) and 160 m offsets (S01-160, S24+160). The P-wave velocity scale is shown in lower right corner.

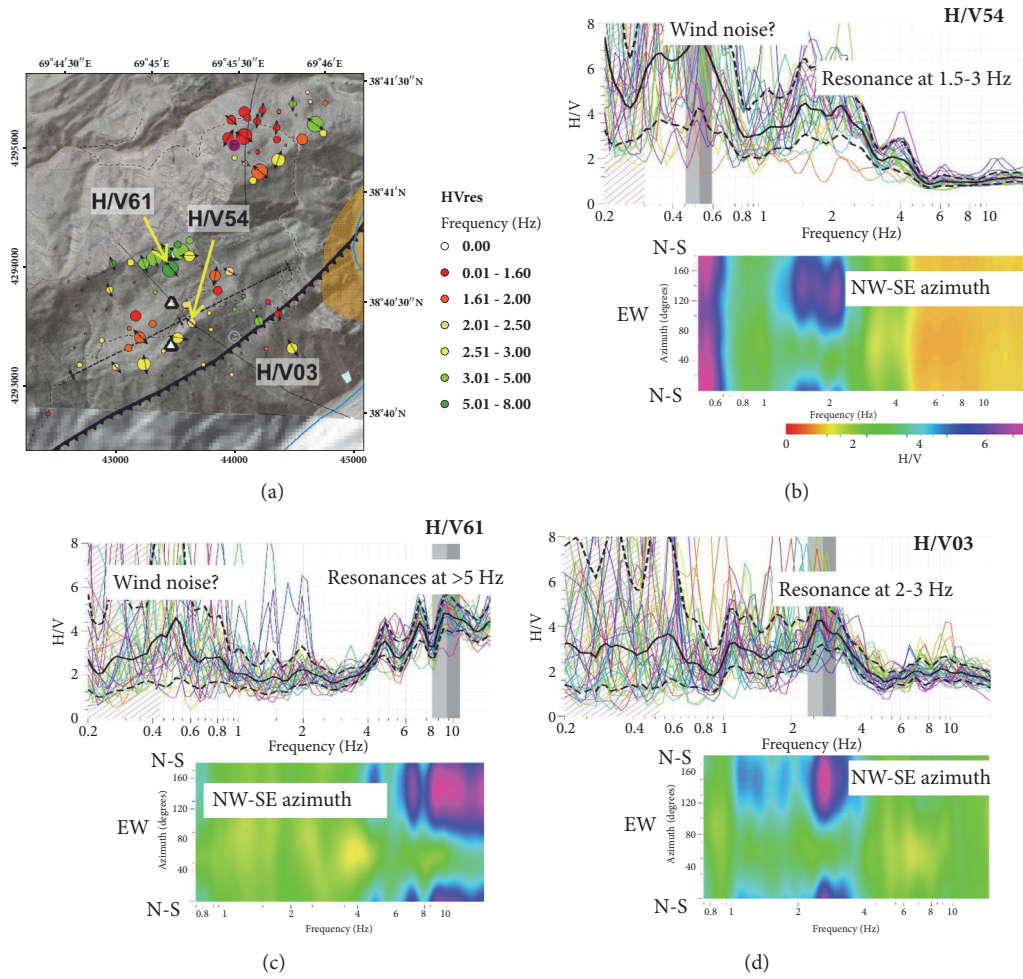


FIGURE 11: (a) Overview map of 92 ambient vibrations measurements (for both studied sites); circles are colored according to the fundamental resonance frequency (see scale in the middle) and with a size proportional to the peak amplitude; see also the double arrows indicating the main vibration orientation (polarization). See also the black Ionakhsh Fault outline crossing the lower slope from NE to SW. (b-d) Three examples of H/V results of processed ambient vibrations, in terms of simple H/V spectral ratios and of H/V azimuth spectra (with polarization information).

of colluvium and/or terrace deposits, while along the slope the material is probably made of wet fractured rocks. We can also see the slight lateral change of resistivities in the middle part of the ERT profile “03” in Figure 9(c), which could point to the presence of a subvertical fault, possibly the Ionakhsh Fault crossing the target region in this area. This lateral change roughly corresponds to the location of the Ionakhsh Fault that is shown on the geological section in Figure 12(c).

The seismic refraction survey included 13 SRT profiles (with Daqlink seismograph and 24 4.5 Hz geophones) with a total length of 4210 meters (8 profiles on Site 1 and 5 profiles on Site 2; see Figure 8). In total, 40 hammer shots and 25 small (250-500 g dynamite) explosions (with min. 40 m offset) were used to trigger seismic waves. Along each profile at least 10 DGPS measurements had been completed to measure the profile position, and all shot points were located by means of DGPS measurements. In the laboratory, the seismic data (recorded over 2.5s, with a time interval of 0.5 ms) were processed with the Sardine software (by

Demanet [18]) in terms of P-wave SRT profiles on Site 1; two examples of SRTs are presented for two long seismic profiles (with several distant explosive shots) in Figure 10. For the seismic profile SP07 (Figure 10(a)) also a multichannel analysis of surface waves (MASW) had been performed (with the SeisImager software, from ABEM company) to determine S-wave velocity (V_s) logs in the middle part of the slope of Site 1 (see V_s -logs and digitized surface wave dispersion diagrams in Figures 10(a1) and 10(a2), respectively, for explosive shots triggered at 100 m from the end and the beginning of the 115 m long profile).

Both SRT profiles in Figure 10 show that in some places relatively low P-wave velocities (V_p) have been measured near the surface, often less than 1000 m/s. These results are also confirmed by low V_s (<500 m/s) measured near the surface, as proved by a few MASW analyses, such as those shown in Figures 10(a1) and 10(a2). Higher V_p -values (>1500 m/s) near the surface were only observed near the upper steep slope below the main crest. At a depth of more than 30 m

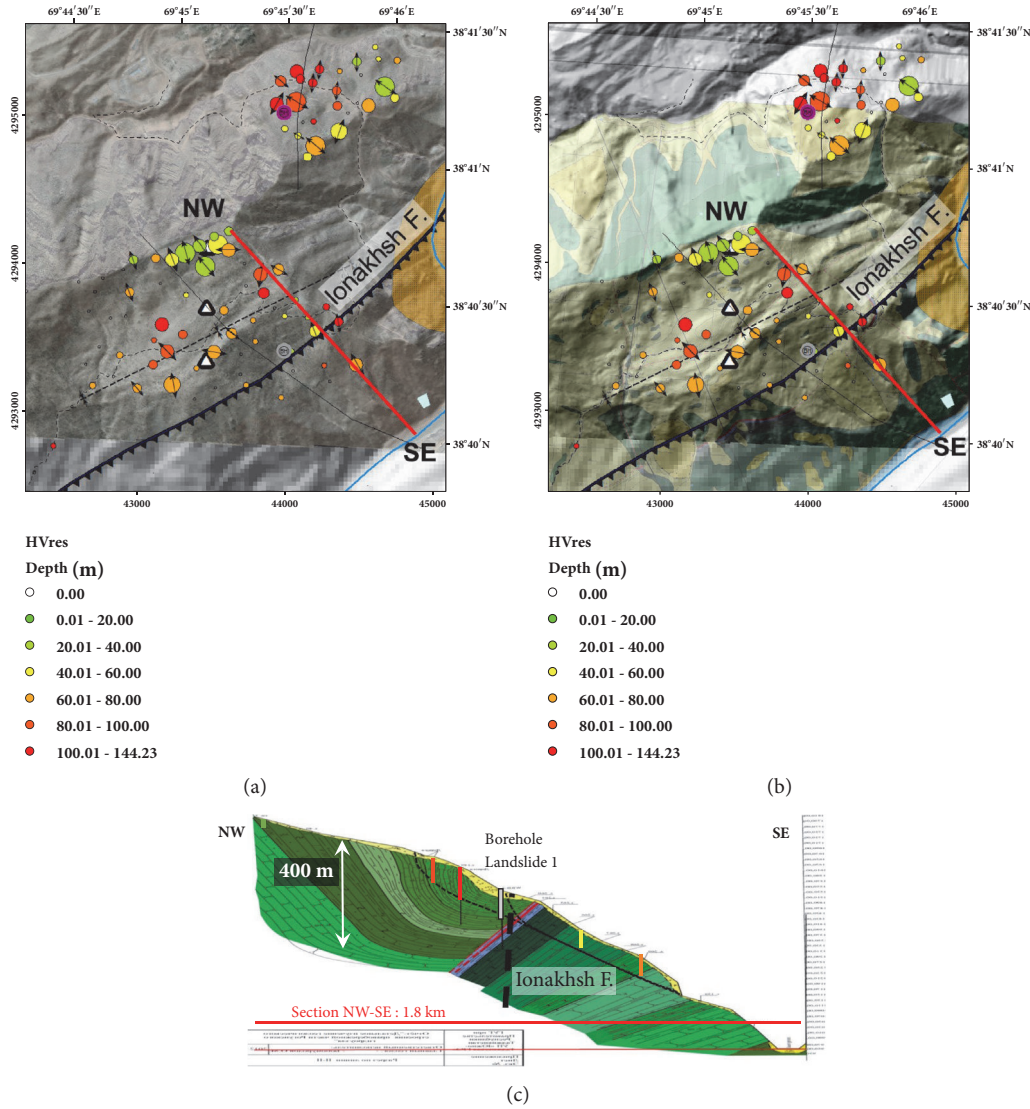


FIGURE 12: (a, b) Overview maps ((a) with Pleiades image; (b) with geological map) of 92 ambient vibrations measurements (for both studied sites); circles are colored according to the depth of the soft rock layer basis inferred from the H/V results and with a size proportional to the peak amplitude; see also double arrows indicating the main vibration orientation (polarization). (c) Geological cross-section (along red line in the maps in (a, b), Southern Tajik Geological Prospecting Expedition, 2012) with location of depth-logs (colored; see for scale the 100 m deep red log) of the soft rock layer basis, location of the Ionakhsh Fault (colored, as from geological map; the dashed black line as inferred from our results), and the borehole (light grey) on Site 1.

only in a few places V_p -values of more than 3000 m/s have been measured. Those results are not typical for a rock slope and point to a general weakening of the rocks over large depths, probably due to intense fracturing. The lowest V_p -values had been measured along the intermediate plateau and along the lower steep slope (see the SRT profiles shown in Figure 10) which are also marked by the lowest electrical resistivities. Thus, for these zones, the presence of deep-seated weak materials has been confirmed by both (electrical and seismic) types of investigations.

By combining all SRT and the two MASW results, we estimated mean V_p - and V_s -values for the first relevant (for slope stability analysis) 60 m, of, respectively, 1500 and 750 m/s (for a Poisson ratio of 0.33) for Site

1 (the values are lower for Site 2, i.e., $V_{p60}=1000$ m, $V_{s60}=500$ m).

92 ambient noise H/V measurements (using a sampling frequency of 200 Hz, completed with a Lennartz L5s seismometer connected to a CitySharkII station) included 62 points on Site 1 and 30 points on Site 2. All H/V points were located with a normal GPS with a precision of about 5 to 7 m. Ambient vibrations data were processed with the Geopsy software (by Wathelet [19]). An overview map of all measurements and three examples of H/V results are shown in Figure 11. The overview map (Figure 11(a)) shows already processed H/V results as circles colored according to the fundamental resonance frequency and with a size proportional to the measured peak amplitude. The three

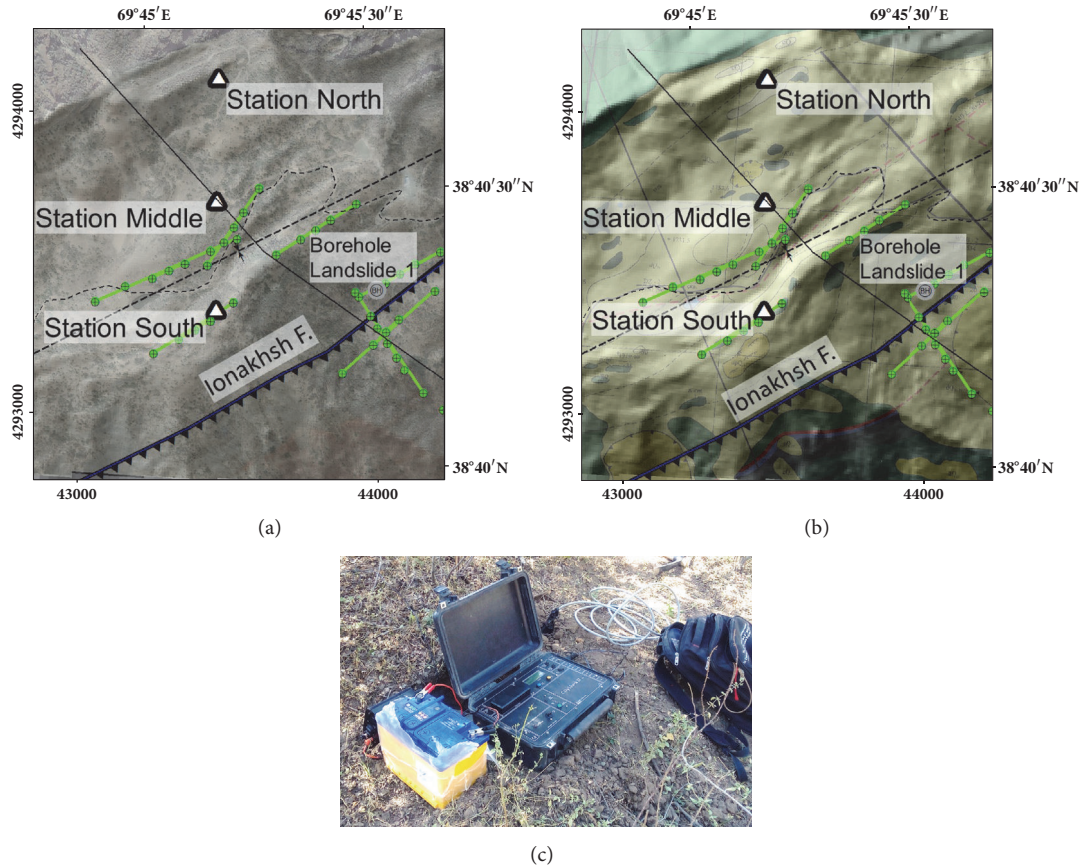


FIGURE 13: (a, b) Overview maps ((a) with Pleiades image; (b) with geological map) of seismological station locations and of seismic profiles (green lines and shot points) on Site 1. (c) CitySharkII station and battery.

examples of H/V results shown in Figures 11(b), 11(c), and 11(d) are presented in terms of both simple H/V spectral ratios and H/V azimuth spectra (with polarization information).

Those examples show that in the upper slope mainly higher resonance frequencies had been measured (>5 Hz, see also green circles in overview map in Figure 11(a), indicating high frequency resonances), marking the presence of a relatively thin (<30 m) cover of potentially weaker materials on top of a medium shallow hard rock, while on the intermediate plateau and also along the steep lower slope some areas are characterized by clear, relatively low frequency, resonance peaks (<4 Hz; see also numerous large red, yellow, and orange circles in those areas in the overview map in Figure 11(a)). Figures 11(b) and 11(c) also show polarization diagrams which clearly indicated a dominant NW-SE oriented shaking of the ambient vibrations, which is likely due to the general NW-SE orientation of the entire slope. In the overview maps in Figure 11(a) and also in Figure 12, this polarization of the horizontal shaking is marked by the azimuth of the double arrows.

From the H/V resonance frequency values, f_0 , we made average soft material thickness, h , estimations, using the equations $h = V_s/4/f_0$. Related results are shown in Figure 12.

For Site 1 we estimate that the thicker soft materials on the intermediate plateau and in some parts of the steep

lower slope mark the general weakness of the rocks in these areas. The map of depths of hard rock indicated by circles is reproduced in Figure 12, together with the same circles plotted on the geological map of the area. Along the red line in Figures 12(a) and 12(b), a geological cross-section (shown in Figure 12(c)) has been established by the Southern Tajik Geological Prospecting Expedition [20]. On this cross-section, we plotted soft layer thickness logs inferred from the H/V resonance frequencies. By interpolating the bottoms of these logs, the body of soft material most exposed to instability phenomena (indicated by a fine dashed line) can be outlined. By comparing H/V results with the geological data, we can also see that the deepest logs are located in the center of a syncline structure within the bedrock. In the middle of this syncline a thick deposit of colluvium/terrace material is marked by the yellow layer in Figure 12(c). Additionally, the 2012 geological survey identified a fault zone in the SE of the Syncline center; this fault zone has also been detected in at least one of our ERT profiles (the one shown in Figure 9(c)); according to our estimates, this fault zone should be subvertical while the geological survey assumed a NW-oriented dip. However, more detailed investigations would be necessary to confirm the precise location of the fault, its dip, and the presence of a certain amount (still uncertain) of Jurassic clayey rocks along the fault.

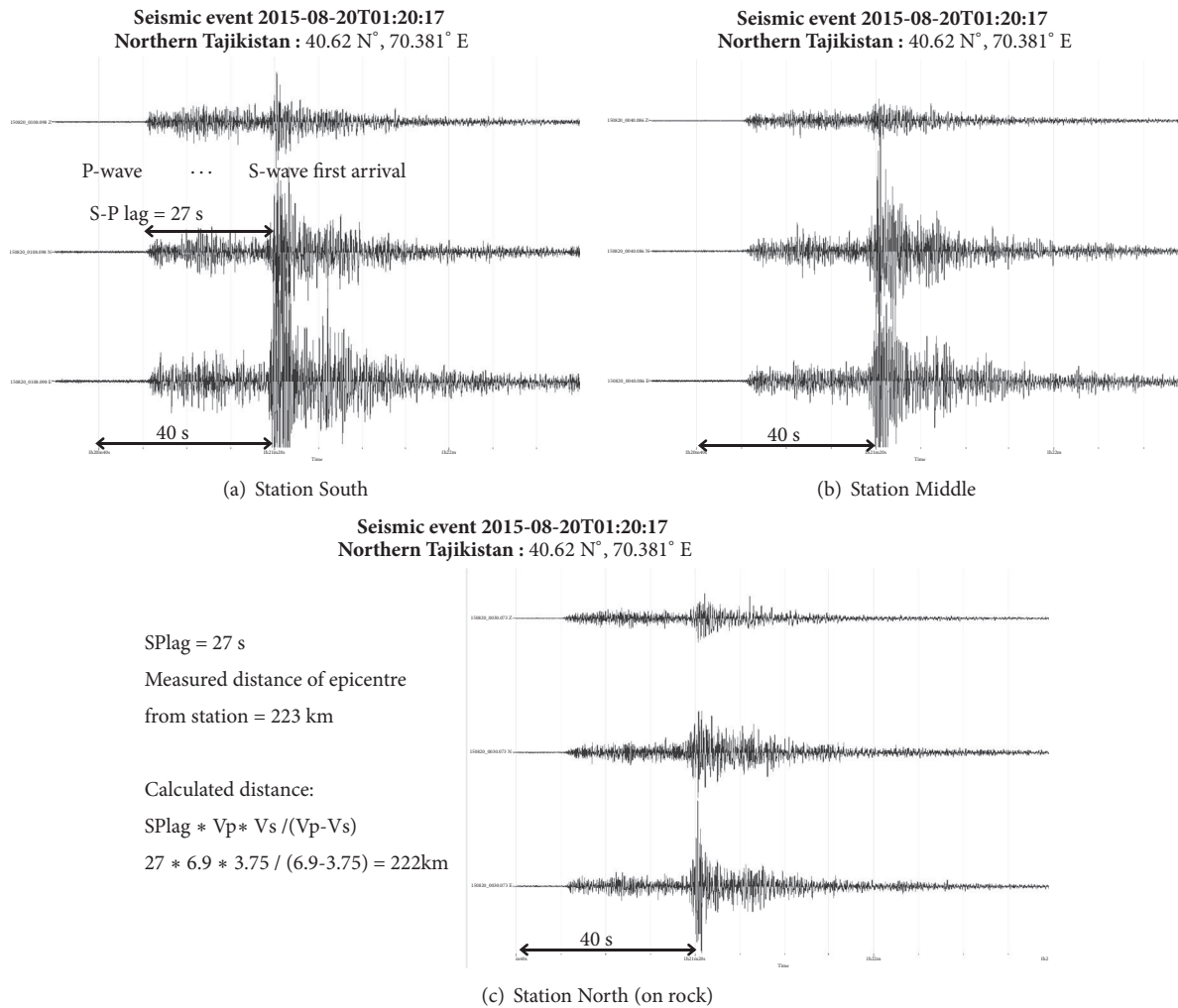


FIGURE 14: Example of seismic event (August 20, 2015, 01:20:17 UTC) in Northern Tajikistan recorded on all three stations: (a) near slope break in the south; (b) on flat area behind the lake; (c) near crest, on hard rock in the north. Amplitudes are scaled.

Seismological recordings have been completed during 10 days with three mobile seismic stations (3 CitySharkII stations, two connected to a Lennartz L1Hz seismometer and one connected to an L5s seismometer; see location in Figure 13) in the area of the intermediate plateau, near the central part of the Syncline structure. During this period of seismic observations, a total of 20 earthquakes had been recorded within a distance of 450 km from the site, including 15 seismic events, which had been measured simultaneously by all three seismic stations; according to the Tajik catalogue, 4 events had a magnitude of 4 or larger. The data recorded on/near the plateau (Stations Middle and South in the maps of Figure 13) had been processed in terms of standard spectral ratios (SSR) computed with the Geopsy software with respect to the measurements on a hard rock site above the slump area (Station North in the maps in Figure 13, with the highest location where a CitysharkII station with an L1Hz had been installed).

From the common 15 identified earthquake recordings we finally selected 10 events that produced the strongest

amplitudes on our sites. Figure 14 presents an example of an event of 20/08/2015 at 0120 am UTC that was recorded by all three stations. This figure also explains the calculation of epicentral distance on the basis of S-P time lag (time difference between P-wave and S-wave arrival) and estimated average values of V_p and V_s for the Earth crust ($V_p = 6.9$ km/s and $V_s = 3.75$ km/s for all events with epicentral distance smaller than 300 km and $V_p = 7$ km/s and $V_s = 4$ km/s for more distant events), estimations being based on calibration with the 4 known event locations (included in the Tajik catalogue). The comparison between those recordings shows that the Southern and Middle Stations are affected by larger shaking amplitudes (here unit-less, but scaled to the same maximum) than the Northern Station that is actually located on (shallow) bedrock.

The spectral analysis applied to the event of 20 August 2015 at 0120 am is documented in Figure 15. This figure shows that the H/V ratios and spectral amplitudes are clearly the smallest at Station North located near outcropping bedrock, which may thus be used as reference station

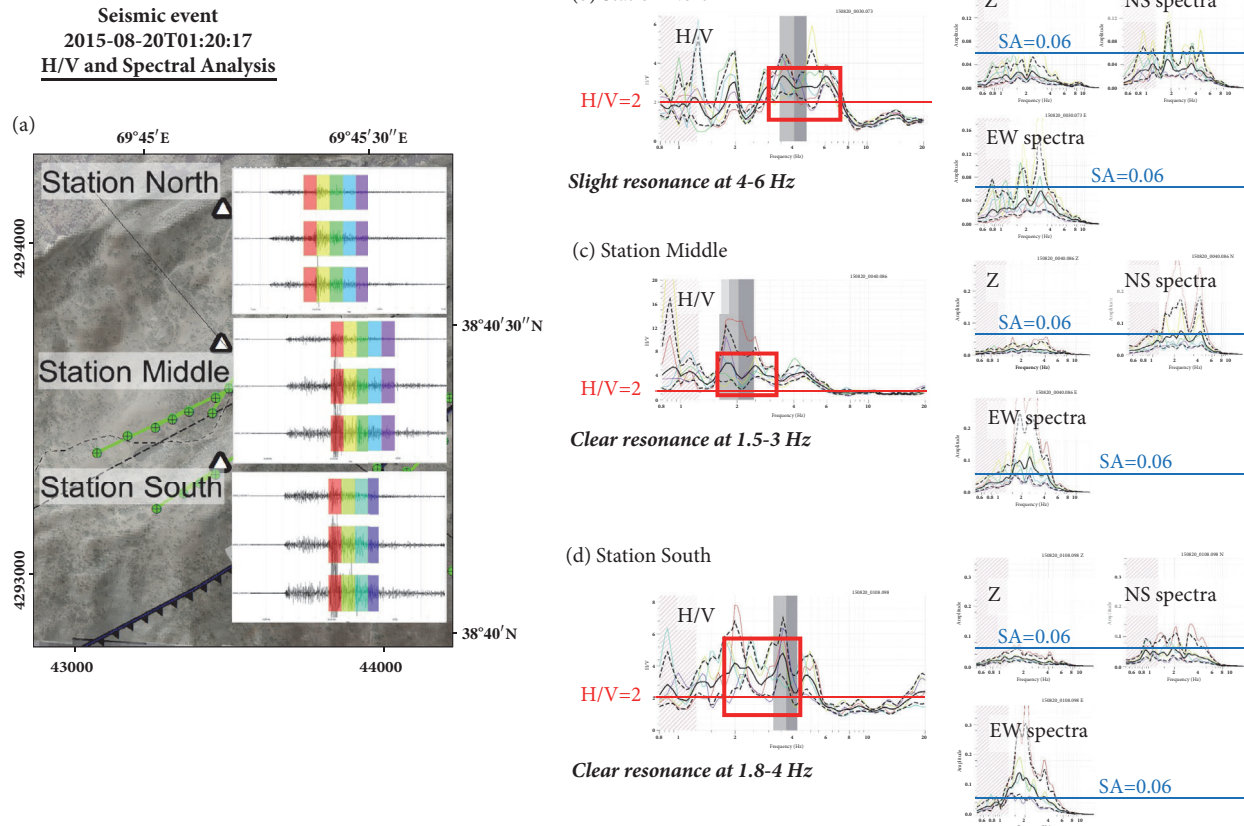


FIGURE 15: August 20, 2015, event analysed with Geopsy software: (a) map with plots of seismograms and 5 selected S-wave windows for spectral analysis; H/V spectral ratios (left) and amplitude spectra (right) calculated for 5 S-wave windows, for Station North (b), Station Middle (c), and Station South (d). See indicated H/V level = 2 and Spectral Amplitude, SA = 0.06.

for site amplification analyses applied to the two other stations.

For each of the 10 analysed events, average EW-NS spectral ratios were computed for Station Middle and Station South with respect to the reference Station North. The procedure is schematically described in Figure 16.

Then, the average of all ten ratios has been computed to determine the site amplification at Station Middle and Station South, as shown in Figure 17. The final average ratios for both Stations Middle and South reveal that the main site amplification (of about 2-3) appears at around 1.5-2.5 Hz (as already shown by the H/V ratios in Figure 11). The strongest amplification is observed for Station Middle (~3) that can only be explained by the presence of deep weak rocks, possibly covered by loose deposits.

Two boreholes had been drilled in autumn 2015, a 120 m deep borehole on Site 1 and a 100 m deep borehole on Site 2. Every 10 m rock samples were taken from the borehole. In total 14 rock samples were used for geotechnical tests completed in two geotechnical laboratories (one belonging to the Rogun HPP construction company and one belonging to the Institute of Geomechanics and Mining of the National Academy of Sciences of the Kyrgyz Republic).

On the basis of the developed 3D geomodels and geotechnical data, slope stability calculations and seismic ground

motion simulations had been completed with the UDEC (Itasca) software. However, those simulations are not the target of the present publication; therefore, below, we will only present some views of the 3D geomodel that has been used as a basis to establish the 2D numerical models.

4. Integrated Geophysical 3D Models and Rock Fall Simulations

All data processed have been inserted in a 3D geological-geophysical model completed with the GOCAD software. The core of the 3D Geomodel is the digital elevation surface model extracted from the 2D GIS software in point format and reinterpolated in GOCAD (as 3D surface). Raster mapping data such as geological maps and satellite images were then projected on this 3D surface (see upper parts of Figures 18 and 19). All geophysical profiles and geological sections (by Southern Tajik Geological Prospecting Expedition, 2012) were imported as vertical Raster profiles disposed in the right position; in addition, all H/V soft layer thickness logs have been inserted as vertical borehole logs (see lower parts of the Figures 18 and 19). In addition, we represented a section of the Ionakhsh Fault in the model (brown surface in the lower parts in Figures 18 and 19); the 3D views show that this fault would cross the middle-upper part of the Southern

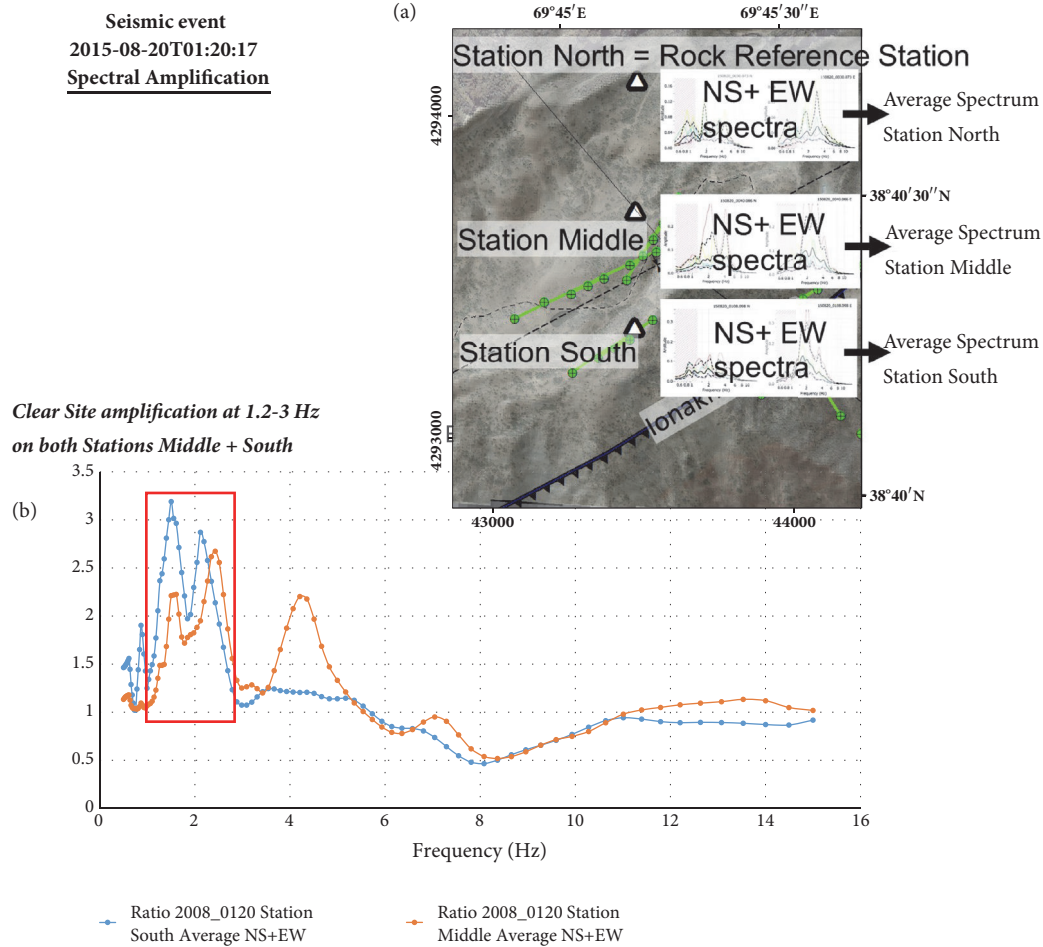


FIGURE 16: Spectral ratios for averaged NS and EW spectra (from spectra shown in Figures 15(b)– 15(d)) computed for event of August 20, 2015 (UTC 01:02:17) for Stations South and Middle with respect to Station North (used as reference station). Location of stations and type of processing indicated in (a); resulting spectral ratios for Station South (blue curve) and Middle (orange curve), with Station North as reference shown in (b).

Slope of Site 1 (denoted as “Landslide 1” in Figures 18 and 19).

A closer view showing the spatial relationship between the Ionakhsh Fault, the site geometry, geophysical profiles, and the existing geological sections is shown in Figure 18. Here, we can see that one ERT profile along the slope crosses the fault (see yellow bar in yellow outline). The large along-slope seismic tomography also crosses the fault (see lower parts of Figures 19(a) and 19(b)), but outside the location of geophones where the V_p variations are weakly controlled. Therefore, no particular V_p changes are shown by this long seismic tomography as all geophones are located on the East side of the fault. However, the ERT profile (shown in Figure 9(c)) displays a change of resistivity from low resistivity in the East (<60 ohm.m) to medium resistivity in the West (>130 ohm.m). This contact seems to be subvertical. Also, our observations in the field combined with analyses of satellite images (Pleiades) confirm a roughly vertical contact of outcropping reddish sandstones in the East (lower Cretaceous) to outcropping grey sandstones in the West (Upper Cretaceous, also found in the borehole). So, we do

not follow the interpretation of the Southern Tajik Geological Prospecting Expedition [20] indicating a fault dip (of less than 60°) to the Northwest (see red line on their profile in Figure 12). The consequence is that, with a vertical dip, the fault also crosses a major part of the upper dam slope (while it would barely “touch” the dam if a dip to the NW is assumed). However, as indicated above, a series of uncertainties affect those interpretations; to confirm the strike and dip of the fault more detailed investigations would have to be completed on the site (also to the East and West of the main slope).

5. Discussion and Conclusions

The main result of the geophysical survey (combined with geological data that were briefly introduced above) is the identification of a large weak zone (roughly 800 by 450 m, along the steep lower slope, starting above the intermediate slope break) on the main investigated Site 1 that is outlined in yellow in the 3D geomodel views in the Figures 18 and 19.

This conclusion is based on previous studies summarized in the report of the Southern Tajik Geological Prospecting

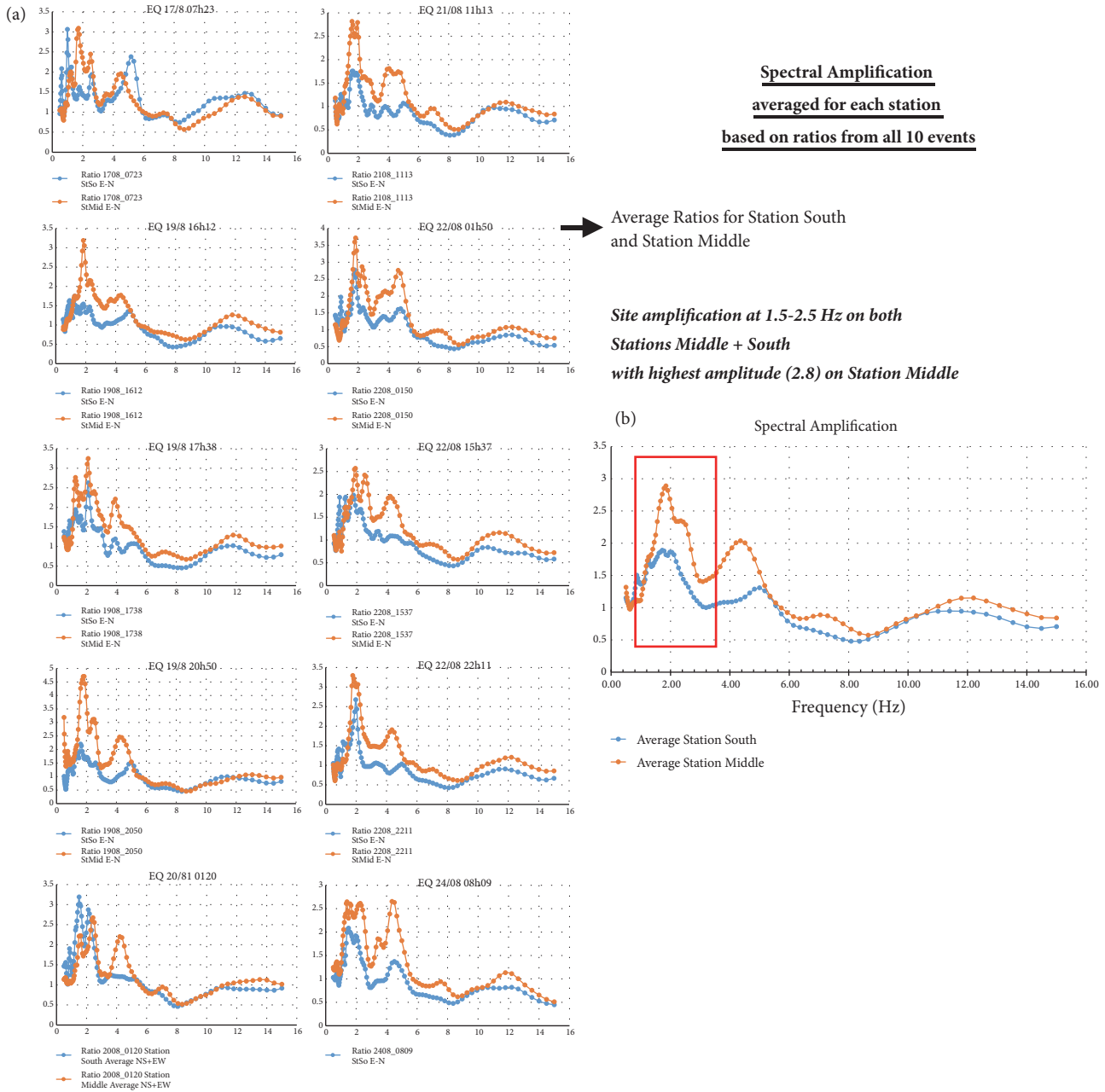


FIGURE 17: (a) Spectral ratios for averaged NS and EW spectra computed for 10 events recorded on all 3 stations, for Stations South and Middle with respect to Station North (used as reference station). (b) Final average spectral ratios for combined NS and EW spectra (from all 10 events), for Stations South (blue curve) and Middle (orange curve) with respect to Station North (used as reference station).

Expedition [20], combined with our geophysical results. The past studies highlighted the morphological and structural features of Site 1, on the right-bank slope of the Vakhsh River above the spillway exit of the Rogun HPP, which characterize a very large potentially unstable zone. Those studies concluded that the total area of the right-bank slope exposed to landslide processes would be about $1.4 \cdot 10^6 \text{ m}^2$ ($1700 \times 800 \text{ m}$: this includes the entire plateau and upper steep slope); the unstable mass would have a thickness of up to 500 m; consequently, the total volume of this mass could be up to $700 \cdot 10^6 \text{ m}^3$. Actually, these estimates are close to

ours when we consider the whole ancient mass movement covering almost the entire investigated slope.

Within this zone, our geophysical results confirmed the presence of a soft layer (weak material) near the surface. However, the extent of the area that is really marked by unfavorable geophysical properties (low resistivity values of less than 100 ohm.m observed in several parts of the intermediate plateau and along the lower steep slope, V_p and V_s of, respectively, less than 1000 and 500 m/s, up to a depth of 20 m as well as low resonance frequencies of less than 4 Hz in the same zones) is far less than what has been estimated

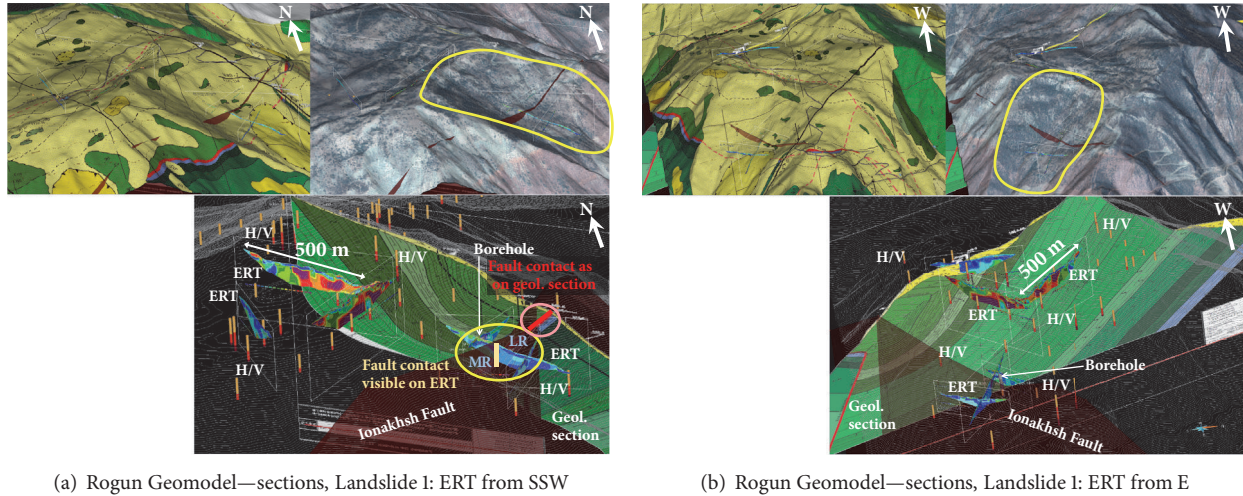


FIGURE 18: Views of 3D geomodel for Site 1 with location of ERT profiles, geological sections, Ionakhsh Fault, H/V logs, and borehole log ((a) view from SSW; (b) view from E). The yellow outline (~800 m long, ~450 m wide) marks the zone that we estimate to be most exposed to slope instability phenomena.

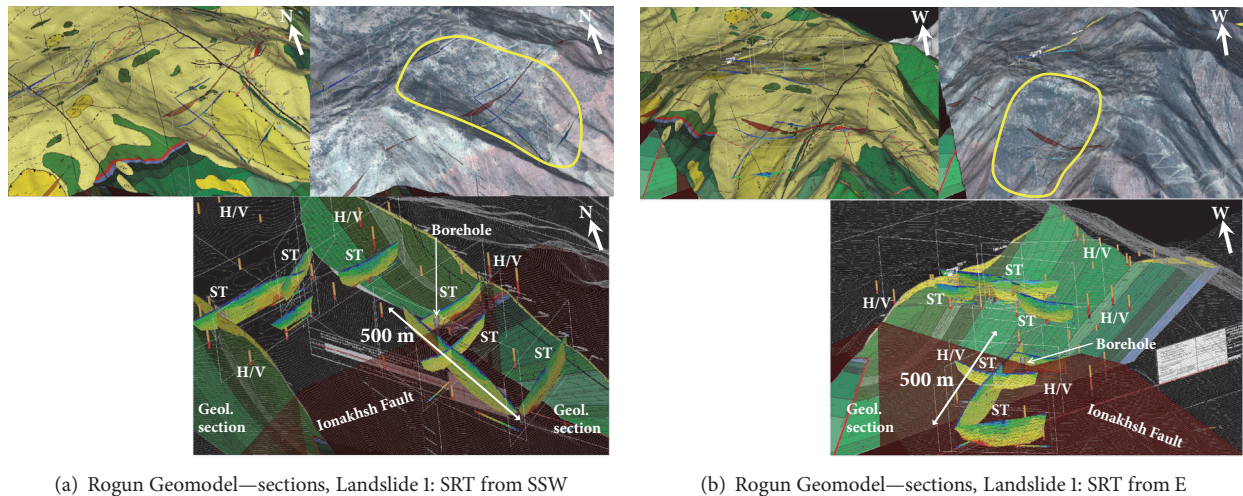


FIGURE 19: Views of 3D geomodel for Site 1 with location of SRT profiles, geological sections, Ionakhsh Fault, H/V logs, and borehole log ((a) view from SSW; (b) view from E). The yellow outline (~800 m long, ~450 m wide) marks the zone that we estimate to be most exposed to slope instability phenomena.

by previous studies and of the amount of $350 \cdot 10^3 \text{ m}^2$ (800 by 450 m yellow outline in the Figures 18 and 19). Figure 14(c) shows that this unstable mass can locally have a thickness of up to 100 m, but on average it is 20-40 m thick. According to those data, the volume of the unstable mass could be up to $10\text{-}15 \cdot 10^6 \text{ m}^3$.

Certainly, also our estimates are affected by numerous uncertainties. First of all, all geophysical measurements highlighted the great variability of electrical, seismic, and resonance properties over Site 1. We observed an absence of resonance peaks in the western part (roughly in the west of the lake of the plateau) which hints at the presence of outcropping hard rock, while along the slope break of the plateau and all over the eastern part of Site 1, resonance frequencies of 1 to 4 Hz indicate the presence of more deeply

fractured-weathered rocks with possible presence of soft deposits (colluvium as well as the terrace material on the plateau). This information combined with morphological aspects such as the deep graben-like depression along the southern border of the plateau might indicate the presence of a deep-seated instability responsible for a more intense fracturing of this part of the slope compared to the western zone. Most probably the Ionakhsh Fault crossing the site and identified on one of the ERT profiles (with subvertical dip) would also contribute to the general instability of the steepest part of the southern slope and of the border of the plateau above the same.

Here, we have not presented the outcomes of numerical studies that had been completed to estimate the likelihood that a major mass movement could be triggered from Site 1

(see a short summary in Havenith et al. [21]). Also, the main question at the origin of our study has not been answered in this paper that is focused on the geophysical results obtained for Site I: could a major mass movement that may be triggered by an earthquake also form a dam on Vakhsh River and could the dammed lake block the exit of the spillway tunnel? We intend to publish those results in a follow-up paper.

Data Availability

The geophysical data used to support the findings of this study are available from the corresponding author upon request.

Conflicts of Interest

The authors declare that they have no conflicts of interest.

Acknowledgments

These works had been completed in 2015 and 2016 in the frame of the 'Program of comprehensive geophysical exploration, analytical calculations and modeling potential stability of the landslide-prone slopes in the area of the main facilities of the Rogun HPP', under the Contract No. 2015-5/2-OP. We thank the Joint Stock Company "Rogunskaya GES" for having allowed us to complete the geophysical surveys on the sites 1 and 2 and for having provided access to past reports.

References

- [1] H. Havenith, I. Torgoev, A. Torgoev, A. Strom, Y. Xu, and T. Fernandez-Steeger, "The Kambarata 2 blast-fill dam, Kyrgyz Republic: blast event, geophysical monitoring and dam structure modelling," *Geoenvironmental Disasters*, vol. 2, no. 1, 2015.
- [2] S. Ulysse, D. Boisson, C. Prépetit, and H. Havenith, "Site Effect Assessment of the Gros-Morne Hill Area in Port-au-Prince, Haiti, Part A: Geophysical-Seismological Survey Results," *Geosciences*, vol. 8, no. 4, p. 142, 2018.
- [3] H.-B. Havenith and C. Bourdeau, "Earthquake-induced landslide hazards in mountain regions: A review of case histories from Central Asia," *Geologica Belgica*, vol. 13, no. 3, pp. 137–152, 2010.
- [4] N. N. Leonov, "The Khait, 1949 earthquake and geological conditions of its origin," in *Proceedings of the Academy of Sciences of the USSR, Geophysics*, vol. 3, pp. 409–424, 1960 (Russian).
- [5] S. G. Evans, N. J. Roberts, A. Ischuk, K. B. Delaney, G. S. Morozova, and O. Tutubalina, "Landslides triggered by the 1949 Khait earthquake, Tajikistan, and associated loss of life," *Engineering Geology*, vol. 109, no. 3–4, pp. 195–212, 2009.
- [6] R. L. Schuster and D. Alford, "Usoi landslide dam and Lake Sarez, Pamir Mountains, Tajikistan," *Environmental and Engineering Geoscience*, vol. 10, no. 2, pp. 151–168, 2004.
- [7] H. B. Havenith, K. Abdrakhmatov, I. Torgoev et al., "Earthquakes, Landslides, Dams and Reservoirs in the Tien," in *Landslide Science and Practice*, C. Margottini, P. Canuti, and K. Sassa, Eds., pp. 27–31, 2013.
- [8] I. Torgoev, H.-B. Havenith, A. Torgoev, P. Cerfontaine, and A. Ischuk, "Geophysical investigation of the landslide-prone slope downstream from the Rogun Dam construction site (Tajikistan)," in *Culture of Living with Landslides*, M. Mikos, N. Casagli, Y. Yueping, and K. Sassa, Eds., vol. 4, pp. 75–84, 2017.
- [9] H. B. Havenith, A. Torgoev, R. Schlögel, A. Braun, I. Torgoev, and A. Ischuk, "Tien Shan Geohazards Database: Landslide susceptibility analysis," *Geomorphology*, vol. 249, pp. 32–43, 2015.
- [10] H. B. Havenith, A. Strom, I. Torgoev et al., "Tien Shan Geohazards Database: Earthquakes and landslides," *Geomorphology*, vol. 249, pp. 16–31, 2015.
- [11] K. Abdrakhmatov, H.-B. Havenith, D. Delvaux, D. Jongmans, and P. Trefois, "Probabilistic PGA and Arias Intensity maps of Kyrgyzstan (Central Asia)," *Journal of Seismology*, vol. 7, no. 2, pp. 203–220, 2003.
- [12] D. Bindi, K. Abdrakhmatov, S. Parolai et al., "Seismic hazard assessment in Central Asia: Outcomes from a site approach," *Soil Dynamics and Earthquake Engineering*, vol. 37, pp. 84–91, 2012.
- [13] A. Ischuk, L. W. Bjerrum, M. Kamchybekov, K. Abdrakhmatov, and C. Lindholm, "Probabilistic seismic hazard assessment for the area of Kyrgyzstan, Tajikistan, and eastern Uzbekistan, central Asia," *Bulletin of the Seismological Society of America*, vol. 108, no. 1, pp. 130–144, 2018.
- [14] D. W. Simpson and S. K. Negmatullaev, "Induced seismicity at Nurek Reservoir, Tadjikistan, USSR," *Bulletin of the Seismological Society of America*, vol. 71, no. 5, pp. 1561–1586, 1981.
- [15] A. K. Chopra and P. Chakrabarti, "The Koyna earthquake and the damage to Koyna dam," *Bulletin of the Seismological Society of America*, vol. 63, no. 2, pp. 381–397, 1973.
- [16] Paradigm, "Paradigm R - E&P Subsurface Software Solutions," <http://www.pdgm.com/>.
- [17] M. H. Loke and R. D. Barker, "Practical techniques for 3D resistivity surveys and data inversion," *Geophysical Prospecting*, vol. 44, no. 3, pp. 499–523, 1996.
- [18] D. Demanet, *Tomographies 2D et 3D à partir de mesures géophysiques en surface et en forage [Ph.D. thesis]*, Liege University, Belgium, 2000.
- [19] M. Wathelet, "GEOPSY Geophysical Signal Database for Noise Array Processing. Software, LGIT, Grenoble, Fr," <http://www.geopsy.org>.
- [20] Southern-Tajik Geological Prospecting Expedition, *Detailed Study of Geological Structure of The Right Bank of Rogun Hydro-system*, vol. 81, 2012.
- [21] M. Mikoš, N. Casagli, Y. Yin, and K. Sassa, *Advancing Culture of Living with Landslides*, Springer International Publishing, Cham, 2017.